CHEMICAL REVIEWS

pubs.acs.org/CR

Review

In Situ TEM Characterization of Battery Materials

Published as part of Chemical Reviews special issue "Manufacturing Science and Metrology Development".

Diyi Cheng, Jinseok Hong, Daewon Lee, Seung-Yong Lee,* and Haimei Zheng*

Cite This: https://doi.org/10.1021/acs.chemrev.4c00507

Read Online

ACCESS | Metrics & More | Article Recommendations

ABSTRACT: Transmission electron microscopy (TEM) is an indispensable analytical technique in materials research as it probes material information down to the atomic level and can be utilized to examine dynamic phenomena during material transformations. *In situ* TEM resolves transient metastable states via direct observation of material dynamics under external stimuli. With innovative sample designs developed over the past decades, advanced *in situ* TEM has enabled emulation of battery operation conditions to unveil nanoscale changes within electrodes, at interfaces, and in electrolytes, rendering it a unique tool to offer unequivocal insights of battery materials that are beam-sensitive, air-sensitive, or that contain light elements, etc. In this review, we first briefly outline the history of advanced electron microscopy along with battery research, followed by an introduction to various *in situ* TEM sample cell configurations. We provide a comprehensive review on *in situ* TEM studies of battery materials for lithium batteries and beyond (e.g., sodium batteries and other battery chemistries) via open-cell and closed-cell *in situ* TEM approaches. At the end, we raise several unresolved points regarding sample preparation protocol, imaging conditions, etc., for *in situ* TEM experiments. We also provide an outlook on the next-stage development of *in situ* TEM for battery material study, aiming to foster closer collaboration between *in situ* TEM and battery research communities for mutual progress.

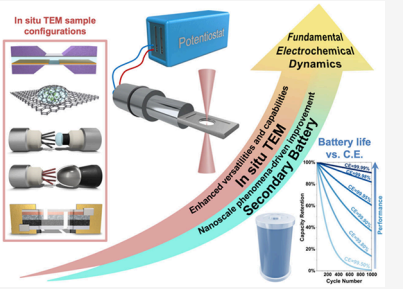

CONTENTS

Received: July 7, 2024
Revised: November 13, 2024
Accepted: November 25, 2024

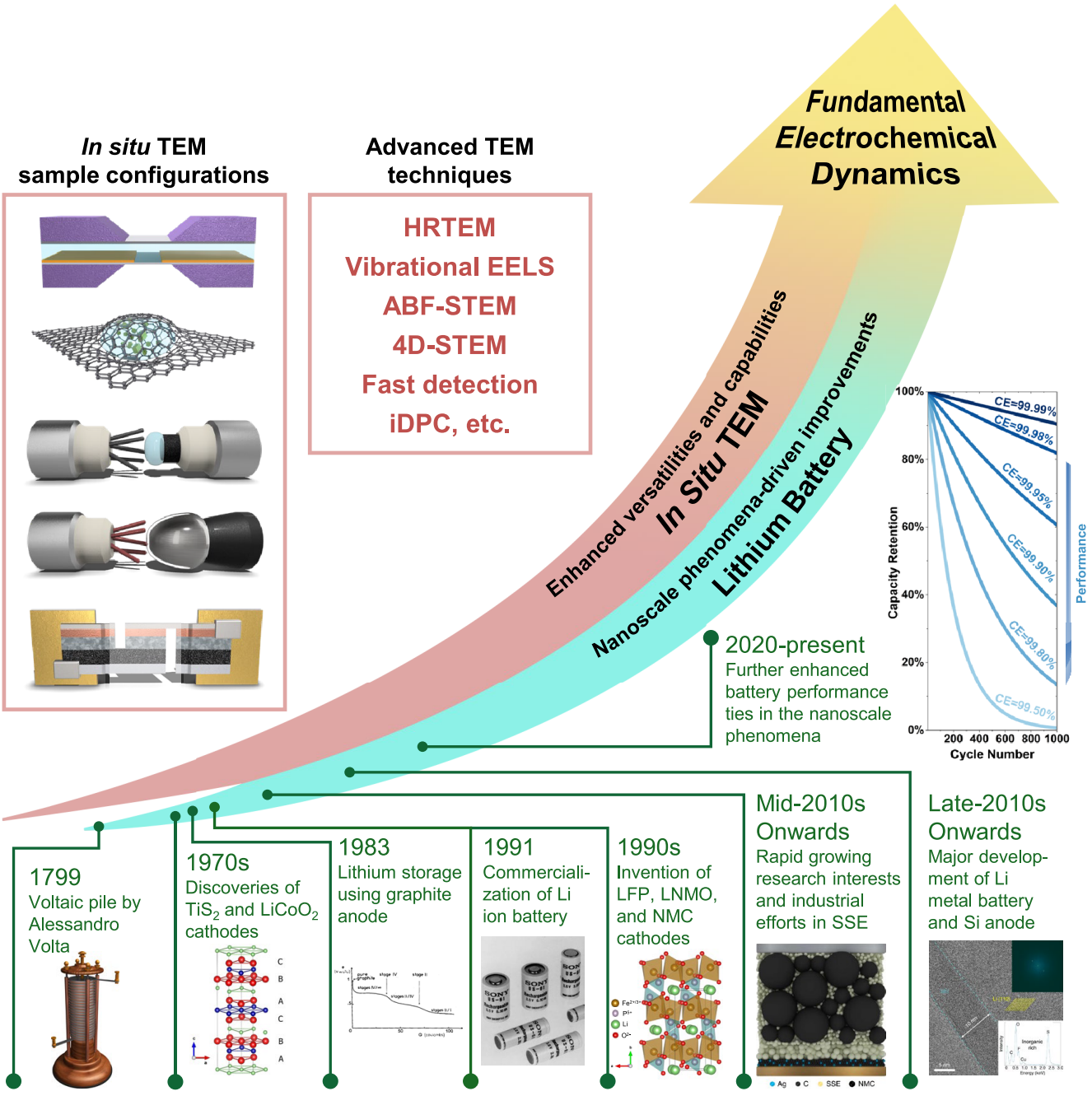

Figure 1. *In situ* TEM capabilities enabled by various sample cells and advanced TEM techniques for battery research. The bottom-half timeline shows the benchmarking events in the lithium battery field, emphasizing the progress of lithium battery research and the nanoscale-phenomena-driven improvement onward. For the images in the bottom row, the "1799" item is reproduced with permission. Copyright 2024, J J Osuna Caballero, Adobe Stock, under Education license. An image credit for the "1991" item is from ref 31. Other images in chronological order ("1970s", "1983", "Mid-2010s Onwards", and "Late-2010s Onwards") are reproduced with permissions from refs 5, 10, 20, 32. Copyright 2017 The Authors, Copyright 1983 Published by Elsevier B.V., Copyright 2020 The Authors, under exclusive license to Springer Nature Limited, Copyright 2019 The Authors, under exclusive license to Springer Nature Limited.

https://doi.org/10.1021/acs.chemrev.4c00507
Chem. Rev. XXXX, XXX, XXX−XXX

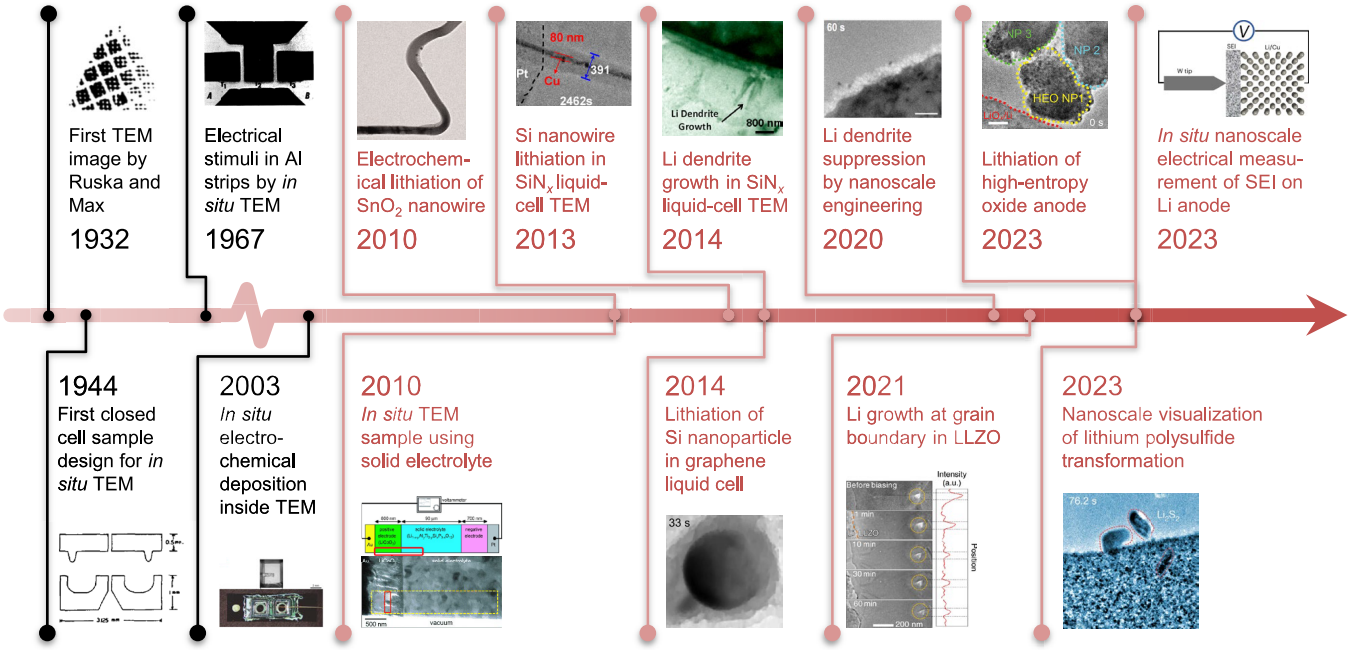

Figure 2. Progress of *insitu* TEM development for applications in lithium battery research. Some work with notable advances of *in situ* electrochemical TEM capabilities are highlighted. In chronological order from left to right and, within the same year, from top to bottom, reproduced with permissions from refs 23, 34−38, 40−47. Copyright 1932 WILEY-VCH Verlag GmbH & Co. KGaA, Weinheim, Copyright 1944 AIP Publishing, Copyright 1967 AIP Publishing, Copyright 2003 Springer Nature Limited, Copyright 2010 The American Association for the Advancement of Science, Copyright 2010 WILEY-VCH Verlag GmbH & Co. KGaA, Weinheim, Copyright 2013 American Chemical Society, Copyright 2014 American Chemical Society, Copyright 2014 American Chemical Society, Copyright 2020 Royal Society of Chemistry, Copyright 2021 The Authors, under exclusive license to Springer Nature Limited, Copyright 2023 Wiley-VCH GmbH, Copyright 2023 The Authors, under exclusive license to Springer Nature Limited, Copyright 2023 UChicago Argonne, LLC, Operator of Argonne National Laboratory.

1. INTRODUCTION

Battery technology has been renovated tremendously since the very beginning of battery conceptualization in 1799, when Volta created the first voltaic pile that was then considered as the first prototype of a battery (Figure 1).[1] The battery research, specifically on lithium battery chemistry, started to take off after the invention of TiS_2[2,3] and $LiCoO_2$ (LCO)[4] in the 1970s. Such layered-structure cathodes are suitable to store and release lithium ions in a rocking-chair manner, along which the generated electricity can be utilized to power devices. Later, in 1983, graphite began to be used in the lithium battery to host lithium ions as the anode, which ultimately promoted the invention of the first commercial lithium ion battery by Sony in 1991.[5] Due to the lack of suitable liquid electrolytes, the early development of battery materials centered on exploring new cathode materials that deliver higher capacity and higher cell voltage with good cyclability. It was the time when a variety of cathodes were invented in the 1990s, including $LiMn_2O_4$,[6] $LiFePO_4$ (LFP),[7] $Li(Ni_xMn_yCo_{1-x-y})O_2$ (NMC),[8] $LiNi_{0.5}Mn_{1.5}O_4$ (LNMO),[9] etc. (Figure 1). Approaching the 2010s, the solid-state battery field rapidly caught research attention worldwide, owing to its promises for better safety, higher energy density and anode compatibility, etc.[10−12] Around the same period, battery research focus started to shift back to anode materials such as lithium metal and silicon in the efforts of replacing graphite with anodes delivering higher capacity.[13−20]

With the mutual efforts from both the research community and industry, battery performance thereby experienced remarkable improvement in the past decades. Nowadays, the state-of-the-art lithium metal battery is able to achieve a Coulombic efficiency (CE) as high as 99.9%.[21,22] However, in order to achieve a capacity retention of 80% after 1000 cycles, an average CE of 99.98% will be needed (Figure 1). An increase of 0.08% in CE seems marginal while it may take the whole battery community decades to pursue, though with a silver lining ahead. As a deeper understanding was obtained along with the research efforts, it became increasingly pronounced that the ultimate enhancement of battery performance ties in the nanoscale phenomena within the electrode materials, electrolytes, and at the interfaces. Such needs place transmission electron microscopy (TEM), especially *in situ* TEM, in a critical position for pushing the boundary of battery research, owing to its capability of monitoring dynamic changes of battery materials under operational conditions with high spatial and temporal resolution.

https://doi.org/10.1021/acs.chemrev.4c00507
Chem. Rev. XXXX, XXX, XXX−XXX

TEM is a powerful and indispensable tool for materials characterizations. With the invention of TEM in the 1930s,[23] remarkable advances have been achieved in the development of TEM techniques and *in situ* TEM capabilities. Since the 1990s, aberration-corrected optics have significantly improved the imaging resolution of TEM. Nowadays, imaging at the atomic resolution has been a routine using modern TEM. Annular bright-field (ABF) imaging can directly visualize light atoms in the presence of heavy atoms, which has provided the opportunity to track distribution and migration of light elements, such as lithium, in battery materials.[24] Spectroscopic techniques, such as energy dispersive X-ray spectroscopy (EDS) and electron energy loss spectroscopy (EELS), enable elemental analysis and valence state examinations, providing critical information for battery research. Spatial resolution of EDS mapping allowing single atom identification has been demonstrated.[25] High resolution EELS was also able to resolve electronic structure of a specific atom.[26] Recent developments in monochromators have made vibrational EELS possible, which allows for probing organic chemistry and minimizing radiation damage.[27] Four-dimensional scanning transmission electron microscopy (4D-STEM) is another highlighted advanced technique that enables unprecedented opportunity to study the nanostructure, strain and charge density of beam sensitive materials in battery electrodes[28] and liquid electrolytes.[29] Additionally, the emergence of the integrated differential phase contrast STEM (iDPC-STEM) technique is capable of obtaining images with a high signal-to-noise ratio under lower electron doses, and breakthroughs have been made in characterizing beam sensitive materials using iDPC.[30]

In parallel, advanced *in situ* TEM with various sample cell configurations has been developed allowing one to mimic the operation conditions of battery materials under electrochemical stimuli, where the state-of-the-art TEM techniques including fast electron detection were integrated. Figure 2 highlights the works with notable advances in the history of *in situ* TEM development, especially the ones with applications in battery research.

An *in situ* TEM study was documented as early as 1942 on the gas−solid interaction under an electron beam.[33] In 1944, a liquid cell was developed with nitrocellulose film on a platinum frame that enabled encapsulation of liquid/vapor inside the cell.[34] Such a cell design facilitated the later development of microsized reactors for *in situ* TEM study of chemical/physical processes in liquid or oil environments. In 1967, Blech et al. customized the TEM sample holder tip using a silicon wafer and was able to observe void formation inside aluminum thin film upon electrical stimuli inside TEM.[35] In 2003, Ross' team developed an electrochemical liquid cell using Si with a SiN_x viewing window to study the electrodeposition of Cu.[36] This liquid cell design became the prototype of modern SiN_x liquid cells for *in situ* TEM study of dynamic reactions and battery materials.

The early 2010s witnessed the beginning of *in situ* TEM applications in the lithium battery field. Several groups individually published works on *in situ* TEM study of different battery materials using open-cell configurations (Figure 2).[37−39] Huang et al. built a nanosized battery configuration inside TEM using a SnO_2 nanowire anode in contact with an ionic liquid electrolyte and a piece of LCO cathode.[37] The electrochemical lithiation of the SnO_2 nanowire was examined using high-resolution TEM under electrochemical stimuli. The lithiation pathways and lithiated products observed in this work set up the principles for later conversion-type electrode material studies. In another work around the same time, Yamamoto et al. built a microsized battery mimicking the solid-state battery configuration that was thinned down by focused ion beam for electron transparency. The use of electron holography was able to identify an electric potential change across the solid−solid interfaces and inside the solid electrolyte.[38] Similarly in 2010, Mai et al. coupled nanowire anodes with a polymer-based solid electrolyte on a customized quartz substrate. They were able to measure the conductance change *in situ* with different states of charge in V_2O_5 nanowires.[39] These works opened the avenue of *in situ* TEM studies of battery materials, especially by using such open-cell configurations where no liquid encapsulation was applied.

Liquid-phase *in situ* TEM was employed in the lithium battery field starting in 2013. Many studies adopted the cell design using Si chips with a SiN_x viewing window.[40−42] The lithiation process of the Si nanowire was examined in a liquid electrolyte consisting of ethylene carbonate (EC) and dimethyl carbonate (DMC) solvents, where volume expansion of the nanowire and the presence of the Li_xSi phase were observed in real time.[40] Zeng et al. utilized a SiN_x liquid cell to monitor the lithium metal behavior in an EC/diethyl carbonate (DEC) liquid electrolyte. The *in situ* results were able to resolve the lithium dendrite growth and the formation of a solid-electrolyte interphase (SEI) at high resolution.[41] Graphene liquid cells have also been used to study lithiation processes of battery materials. For instance, Yuk et al. employed a graphene liquid cell to monitor the lithiation process of Si nanoparticles (NPs) and captured the preferred orientation of the lithiation direction in the NPs.[42] However, since no electrodes were included inside the cell, the lithiation processes inside the graphene liquid cell were induced by electron beam irradiation instead of electrochemical stimuli. The SiN_x liquid cell and graphene liquid cells are categorized as closed-cell sample configurations, which will be introduced in detail in the next chapter.

Entering the 2020s, a lithium dendrite suppression strategy via nanoscale engineering was implemented in a SiN_x liquid cell, uncovering the correlations between lithium metal morphologies and the SEI through high-resolution EDS.[43] An open-cell configuration was employed to study a $Li_7La_3Zr_2O_{12}$ (LLZO) solid electrolyte, and captured unexpected lithium dendrite growth at the grain boundaries in LLZO when an electrochemical stimuli was applied.[44] Coupling *in situ* TEM with valence EELS, this work provides direct evidence on the relatively higher electronic conductivities at the crystal grain boundaries in the solid electrolyte.[44] Such an attribute might lead to a local current hotspot and cause dendrite formation within the solid electrolyte during battery operation. Several other *in situ* TEM studies in 2023 unequivocally demonstrated the power of *in situ* TEM on nanoscale dynamics characterization. Su et al. utilized an open-cell configuration to investigate the lithiation mechanism of high-entropy transition metal oxide that can be potentially used as lithium battery anodes. The conversion reaction observed by *in situ* TEM directly suggested that the lithiated oxide can recover into its single-phase oxide just like a pristine material.[45] Another team managed to measure the electronic conductivity of SEI on a deposited lithium dendrite by employing an innovative *in situ* experimental design. The results unveiled a voltage-dependent differential conductance of the SEI layer, which has not been observed previously and is

https://doi.org/10.1021/acs.chemrev.4c00507
Chem. Rev. XXXX, XXX, XXX−XXX

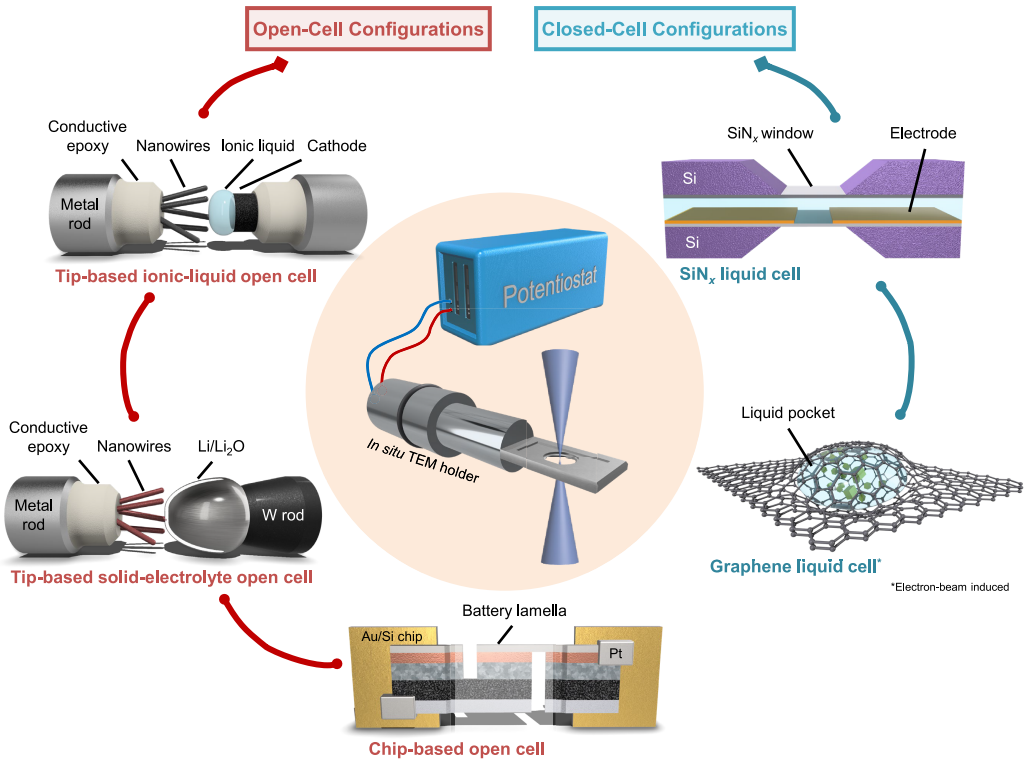

Figure 3. Schematics of common sample cell configurations for *in situ* TEM characterization of battery materials. Open-cell configurations include tip-based ionic-liquid open cell, tip-based solid-electrolyte open cell, and chip-based open cell. Closed-cell configurations highlight the SiN_x liquid cell and graphene liquid cell.

directly related to the cycling stability of a lithium metal anode.[46] A work published by Zhou et al. studied the transformation of lithium polysulfide species in a closed-cell configuration of lithium−sulfur (Li−S) battery chemistry. It yields unequivocal evidence of the evolving lithium polysulfide species during charging and discharging, and reveals the nucleation pathway of lithium sulfide.[47] To this day, *in situ* TEM continues to flourish in battery materials research, providing unprecedented insights for both the liquid- and solid-state battery fields.

In this review, we first introduce the *in situ* TEM approaches established for different battery material systems. We then summarize *in situ* TEM works using both open-cell and closed-cell configurations performed on battery materials in the past 14 years, including various types of anode, cathode, and electrolyte materials. Given the primary research attention from academia and industry on the lithium batteries, the majority of this article covers lithium-battery-related studies via advanced *in situ* TEM. We spend one chapter summarizing the progress in the battery chemistries beyond Li-containing materials, namely those containing sodium (Na), potassium (K), zinc (Zn), magnesium (Mg), calcium (Ca), etc. We then highlight several points regarding sample preparation and data acquisition processes, where bias and misinterpretations could arise, potentially obscuring the realistic scenarios occurring within battery systems. At the end, we provide an outlook on the future directions and potential impact of *in situ* TEM on the next-stage advancement of battery fields, where mutual progress shall be anticipated.

2. *IN SITU* TEM APPROACHES AND SAMPLE CELL CONFIGURATIONS

In situ TEM studies driven by electrochemical stimuli require a specialized experimental setup, which commonly includes a TEM sample holder with electric biasing capabilities, a potentiostat for electrical input, and the sample reaction cell. Based on how the sample is maintained during measurement—specifically, whether the electrolyte is encapsulated—sample cell configurations can be categorized into two main types—closed cell and open cell (Figure 3). Each cell configuration exhibits its unique merit during *in situ* TEM examination.

2.1. Open-Cell Configuration

The open-cell configuration includes tip-based ionic-liquid open cell, tip-based solid-electrolyte open cell, and chip-based open cell, where the common feature is the electrolyte being directly exposed to a vacuum environment inside the TEM column. Due to either the negligible vapor pressure of ionic liquids or the solid nature of solid electrolytes, open cells are able to bear a vacuum environment and beam irradiation without the aid of an encapsulation mechanism.

2.1.1. Tip-Based Ionic-Liquid Open Cell. An ionic liquid with a low vapor pressure may withstand a high vacuum environment inside the TEM column. In one of the earliest reported works employing an ionic liquid as the electrolyte, lithium salt was dissolved in 1-butyl-1-methylpyrrolidinium bis (trifluoromethylsulfonyl) imide (P_{14}TFSI), which served as the lithium-conducting medium during battery operation.[37] The lithium source comes from a piece of LCO cathode on one end, which is covered by an ionic liquid. On the other end, the sample of interest, usually low-dimensional materials such as nanorods, nanowires, or nanoparticles, is attached to a metal

https://doi.org/10.1021/acs.chemrev.4c00507
Chem. Rev. XXXX, XXX, XXX−XXX

rod and a piezo manipulator during sample preparation. The piezo manipulator can be used to control the distance and contact between the sample and the ionic liquid. This conductive piezo manipulator can be then used to apply electrical stimuli to trigger the electrochemical process.[37]

The spatial resolution of a tip-based ionic liquid open cell is comparable to that of a graphene liquid cell when the sample thickness is essentially low. Due to the absence of organic liquid electrolytes that are usually extremely beam-sensitive, a tip-based ionic liquid open cell can withstand higher electron dose rates and achieve a higher spatial resolution. However, this setup requires samples with specific shapes and dimensions in the nanoscale regime, casting limits on sample selections. An ionic liquid may also bring ambiguity to the testing results because most practical battery systems utilize organic liquid electrolytes or solid electrolytes instead of ionic liquids.

2.1.2. Tip-Based Solid-Electrolyte Open Cell. Another type of open-cell configuration utilizes the same idea as the ionic-liquid open cell but uses a solid electrolyte as the lithium-conducting medium. In the case of lithium battery systems, this solid electrolyte is normally a thin layer of Li_2O naturally formed on the surface of the Li metal mounted on the anode side. Although Li_2O is a modest lithium conductor, its low thickness and insulating nature guarantees the Li_2O layer a good medium in the open-cell setup. Li metal is normally mounted on a tungsten tip and the rest of the setup is similar to the ionic-liquid open cell.

Inheriting the upside of open cell, tip-based solid-electrolyte open cell provides high spatial resolution. In some cases, nanoparticle samples can be mounted on a half-cut carbon-film-supported TEM mesh grid, where the Li/Li_2O tip is brought into contact with the grid, indirectly transferring lithium ions through the carbon film.[48] Alternatively, this setup can be used directly to study the interfacial reactions of electrode materials or solid electrolytes in contact with lithium metal.[49,50] The unique setup makes it possible to study the interfacial phenomena between sample materials and Li metal, which is also a major direction for lithium battery research. Due to the use of piezo manipulators in both open-cell configurations, they can be categorized as tip-based open cells.

2.1.3. Chip-Based Open Cell. The last type of open cell does not require the use of piezo manipulators. Instead, the battery sample presents itself in the form of a thin lamella that is mounted across the gap on a pattern chip that is conventionally made of Si. The electrical contact is patterned on the Si chip with metal layers, such as Au and Pt, etc. This approach commonly utilizes a focused ion beam to extract the lamella from the bulk battery and then transfer it onto the Si chip, after which the lamella has its anode current collector and cathode current collector isolated on each side to build the electrical pathway[51,52] (Figure 3). The middle region of the lamella is thinned down to tens of nanometers in thickness for TEM observation.

Chip-based open cell preserves the pristine interface inside the solid-state battery system and has the most-like sample geometry as the real solid-state batteries. Nevertheless, the procedure to produce such nanosized batteries is nontrivial and time-consuming. Extra care needs to be taken to avoid short-circuiting inside the nanosized battery.[51,53] Besides, sample selection is largely limited to those that can form layered thin film structures.

2.2. Closed-Cell Configuration

Since most liquid electrolytes used in batteries consist of organic compounds with high vapor pressure that cannot withstand direct exposure to vacuum, the closed-cell approach is more viable for *in situ* TEM studies of battery materials in organic liquid electrolytes. For the closed-cell configuration, the wet sample is sandwiched between two thin membranes in the liquid cell during measurement. A liquid cell can be either self-contained or designed as a flow cell, allowing liquids to flow in and out of the cell via nanotubing. The self-contained liquid cell design adopts a variety of membrane materials, such as SiN_x,[36,54−57] polymers,[58] graphene,[59] amorphous carbon,[60] MoS_2,[61] BN,[62] or other two-dimensional (2D) materials. So far, nearly all the commercial flow cells use SiN_x as membrane because of the well-established microelectro-mechanical systems (MEMS) processing that can fabricate SiN_x windows with a low defect rate.[57,63]

The SiN_x liquid cell, either self-contained or a flow cell, makes it easier to incorporate electrodes into the cell, thus it has been predominately used for *in situ* TEM study of battery materials during electrochemical processes. Graphene liquid cells have also been used for characterization of battery materials. However, the material transformations observed in the graphene liquid cell are often driven by electron irradiation rather than electrochemical stimuli. Some other common 2D materials suffer from similar issues regarding the integration of conductive electrodes. Polymer electrochemical liquid cells have recently been reported for *in situ* TEM study of electrocatalytic reactions,[58] which may open new opportunities for *in situ* TEM study of battery materials in the future.

2.2.1. SiN_x Liquid Cell. The self-contained SiN_x electrochemical liquid cells have the sample materials and liquid electrolytes preloaded into the cell without further liquid flow during *in situ* TEM characterization (Figure 3). Electrodes made of various materials (e.g., Ti, Au, Pt, etc.) are patterned on a Si/SiN_x chip. Another chip has liquid reservoirs adjacent to the SiN_x membrane window. These chips are stuck or glued together with the SiN_x windows aligned, allowing the electron beam to pass through. Samples can be loaded into the liquid cell with the liquid reservoir, followed by sealing the samples inside the cell before *in situ* TEM imaging.

Similarly, in a flow cell, the sample of interest can be loaded in the viewing area on the chip. It is followed by clamping two chips together with an O-ring so that a closed cell is formed confining the liquid electrolyte between the membranes.[36] Nanotubing is connected with the liquid cells and passes through the TEM holder, which enables the liquids to transport in/out of the liquid cell. Additionally, a pumping system is normally connected to the system to allow liquid to flow through the cell during measurement. This design guarantees either a continuous flow of liquid or static conditions where the liquid remains stationary during experiments.

The SiN_x liquid cell is a versatile sample platform as it enables real-time observations of various battery materials dynamics in liquid electrolytes, mimicking the real environment of liquid-electrolyte batteries. The types of liquid electrolytes can be changed according to the experimental needs. Nevertheless, the downside of this approach is the compromised spatial resolution due to thick SiN_x membranes (e.g., each can be at least 30 nm-thick), and large spacing of the SiN_x window due to membrane bulging, thus thickening the liquid in the path of the electron beam. Moreover, simple

https://doi.org/10.1021/acs.chemrev.4c00507
Chem. Rev. XXXX, XXX, XXX−XXX

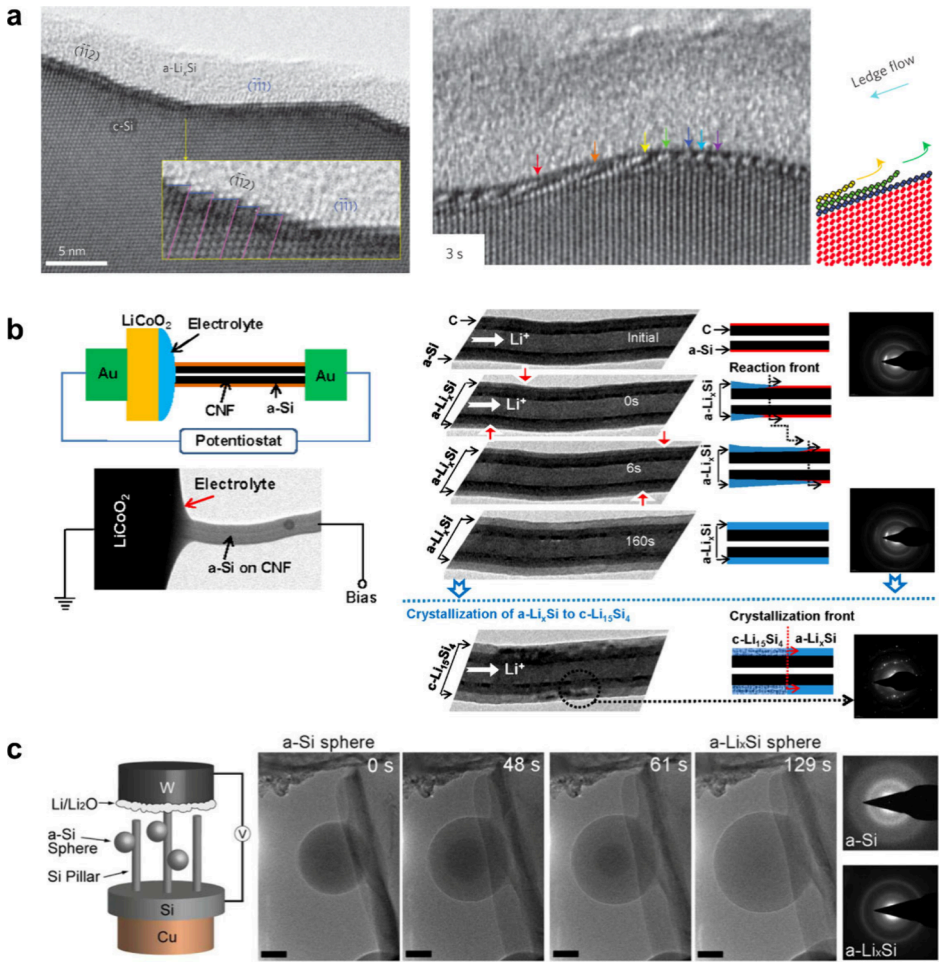

Figure 4. Lithiation process of Si nanomaterials via open-cell *in situ* TEM configurations. (a) High-resolution TEM (HRTEM) images at the early stage of lithiation showing the interface between amorphous and crystalline regions, along with the Si atom detachment process in a ledge flow. Reproduced with permission from ref 78. Copyright 2012 Springer Nature Limited. (b) Schematics of the open-cell setup and the microstructural evolution of the Si-coated CNF during lithiation. Reproduced with permission from ref 79. Copyright 2012 American Chemical Society. (c) A schematic of the open-cell setup and time series of the lithiation of a single amorphous Si sphere. Scale bars: 200 nm. Reproduced with permission from ref 80. Copyright 2013 American Chemical Society.

drop-casting methods often lead to high contact resistance, hindering effective electrochemical reactions. Lastly, a SiN_x liquid cell often has a single narrow rectangular window, which limits the field of view for observations. Regardless, the SiN_x liquid cell remains the dominating approach so far for *in situ* TEM study of battery materials due to its versatility and reliability.

2.2.2. Graphene Liquid Cell. A graphene liquid cell is made with two layers of graphene sheets suspended on TEM grids (e.g., commercial Cu mesh grids). The wet samples of battery materials in the liquid electrolyte are loaded onto one graphene sheet on a TEM grid, and then the other graphene sheet is placed on the top to form a sandwiched liquid cell sealed by van der Waals forces between the graphene sheets. It often forms many liquid pockets inside a graphene liquid cell. Owing to the thin nature of graphene sheets, graphene liquid cells yield superior spatial resolution compared with SiN_x liquid cells (Figure 3).

A major drawback of graphene liquid cell is that it is usually not equipped with electrical contacts due to the electrically conducting graphene membrane, rendering it unable to apply electrical control to the material systems. As such, material changes occurring in a graphene liquid cell are primarily induced by electron beam irradiation. Such characteristics fall short of demands on the battery systems, which normally require electrical stimuli and precise control. In this regard, graphene liquid cells have limited applications in the study of battery chemistry. Nevertheless, due to its simple setup and high spatial resolution, graphene liquid cell has been widely used in the study of chemical processes where the electron beam is used to trigger the reactions.[60,64−68]

3. *IN SITU* TEM STUDY OF ANODE MATERIALS FOR LITHIUM BATTERIES

3.1. Silicon

The Si anode is renowned for its high theoretical capacity, comparable to that of the Li metal anode, and its earth abundance, rendering it a cost-effective and efficient alternative to the widely used graphite and Li metal anodes.[69−72] The Si anode undergoes an alloying reaction as eq 1 shown below:

$$Si + x{\cdot}Li^+ + x{\cdot}e^- \leftrightarrow Li_xSi \quad (1)$$

However, due to the nature of the alloying reaction, the Si anode suffers from severe volumetric changes during the repeated cycling, up to 300% of volume expansion and

https://doi.org/10.1021/acs.chemrev.4c00507
Chem. Rev. XXXX, XXX, XXX−XXX

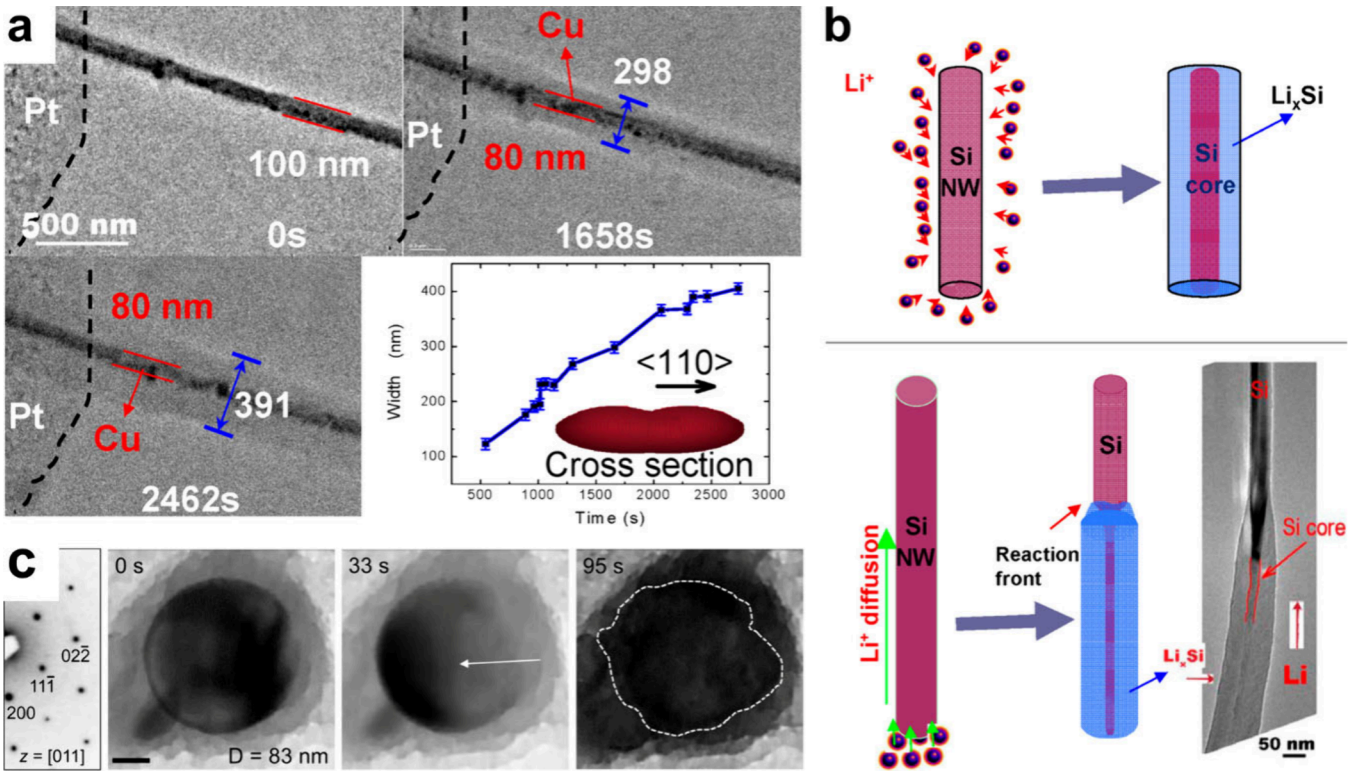

Figure 5. Lithiation process of Si nanomaterials via closed-cell *in situ* TEM configurations. (a) TEM images showing the lithiation of the Cu-coated Si NW and a plot of NW width changes vs. time. Reproduced with permission from ref 40. Copyright 2013 American Chemical Society. (b) Schematics of isotropic lithiation of Si NW in a liquid environment and directional lithiation of Si NW in open-cell configuration. Reproduced with permission from ref 40. Copyright 2013 American Chemical Society. (c) Morphological changes of Si NPs during lithiation. The white arrows indicate the <110> directions of Si crystal. Scale bar: 20 nm. Reproduced with permission from ref 42. Copyright 2014 American Chemical Society.

shrinkage.[73−76] Such a drastic structural change leads to the collapse of electrode integrity, resulting in cracking, pulverization, continuous SEI growth, and a trapped Li−Si alloy, which ultimately consume the active material and deplete the lithium reservoir.[76,77] In order to overcome the negative impact of the volume change in Si anode during cycling, it is essential to understand its lithiation mechanism at the nanoscale and investigate effective strategies to alleviate the volumetric change. Numerous *in situ* TEM studies have been performed on the Si anode in various configurations, i.e., nanowire (NW), nanosphere (NS), nanorod (NR), etc., where invaluable information has been collected that enlightens the research field for better engineering efforts at the bulk scale.

3.1.1. Amorphization and Lithiation Pathways. It has been documented from many works that the Si anode tends to form an amorphous phase before full lithiation.[78−80] After the Si anode is 100% lithiated, there exist both amorphous and crystalline Li_xSi phases in the electrode, while the transition from crystalline Si to the amorphous phase and the subsequent amorphous-to-crystalline transition processes remain a conundrum. *In situ* TEM has been utilized to probe the nanoscale changes during these two processes to provide insights with the help of other characterization tools.

An early *in situ* study in 2012 used the tip-based open-cell configuration to study the behavior of a single-crystalline Si nanowire upon lithiation from a Li metal anode, where the migration of the reaction front was captured (Figure 4a). Li reacts with Si from the outer surface of the nanowire and forms an amorphous Li_xSi phase. With the reaction proceeding, the interface between the amorphous and crystalline phases approached the deeper region of the nanowire. Intriguingly, Si atoms were lithiated in a ledge flow manner at the reaction front, where Si atoms react with Li atoms and detach from the crystalline body, atomic layer by atomic layer.[78] Different crystal orientations yielded different mobility of the amorphous/crystalline interface, stressing the importance of interfacial dynamics associated with the crystallinity of the Si anode for rate capability and deformation behavior. Another work in the same year probed the lithiation mechanism of amorphous Si nanowire using a battery setup, where $LiCoO_2$ was used as the cathode and ionic liquid was used as the electrolyte.[79] Amorphous Si coated on a carbon nanofiber (CNF) manifests an amorphous-to-crystalline transformation that appears facile and congruent. The *in situ* TEM configuration clearly captured the volume expansion during the first lithiation accompanying the amorphous phase, whereas crystallization of $Li_{15}Si_4$ species occurred after the volume expansion process subsided, as depicted in Figure 4b. Such direct evidence shows that the amorphous-to-crystalline transformation is determined by the lithium content in the amorphous phase.[79] By coupling density function theory (DFT) calculation and molecular dynamics (MD) simulation, a drastically higher thermodynamic driving force was uncovered for the amorphous-to-crystalline transformation with increasing lithium content in Li_xSi. Similar phenomena were also observed elsewhere.[81] During the crystallization step, although lithium content keeps increasing, the volume of Si nanowire remains relatively stable, indicating that the major volumetric change occurs during the amorphization stage in early lithiation. In contrast to Si nanowires, Si nanospheres

https://doi.org/10.1021/acs.chemrev.4c00507
Chem. Rev. XXXX, XXX, XXX−XXX

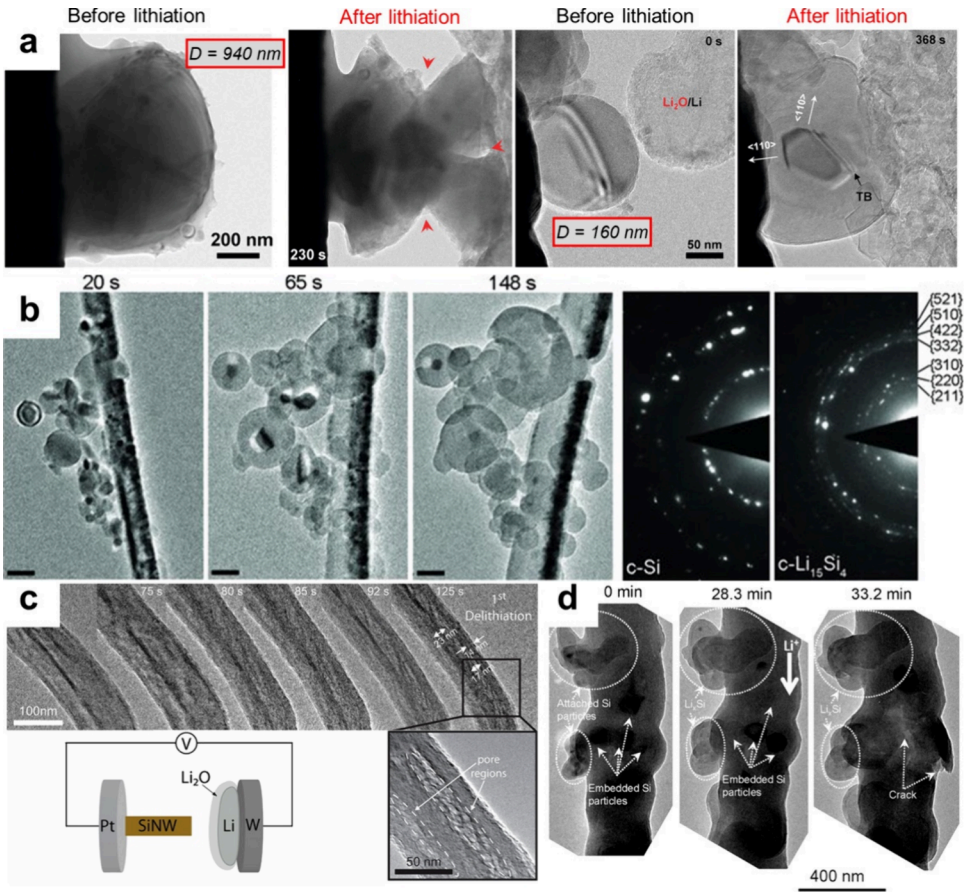

Figure 6. Nanomechanical phenomena during (de)lithiation of Si nanomaterials using open-cell configurations. (a) TEM images showing different deformation behaviors of Si particles with diameters of 940 and 160 nm, respectively. Reproduced with permission from ref 82. Copyright 2012 American Chemical Society. (b) Morphology changes and selected area electron diffraction (SAED) patterns of Si NPs during lithiation. Scale bars: 100 nm. Reproduced with permission from ref 83. Copyright 2012 WILEY-VCH Verlag GmbH & Co. KGaA, Weinheim. (c) Shape change of Si NWs during lithiation and delithiation, highlighting the pore formation after delithiation. Reproduced with permission from ref 84. Copyright 2018 American Chemical Society. (d) Comparison of the lithiation nanomechanics of the Si particles attached to and embedded in the CNF. Lithiation of the embedded particles caused carbon fiber cracking. Reproduced with permission from ref 85. Copyright 2012 American Chemical Society.

exhibit a two-phase transition during the first lithiation, whereas the nanospheres remain an amorphous state (Figure 4c). The gradual change of the image intensity combined with mathematical simulation indicates a varied lithium diffusivity in the nanospheres.[80] The absence of a crystalline phase in the nanosphere could be ascribed to the insufficient lithium in the structure, as compared with the nanowire scenario.

In situ TEM studies with the open-cell configuration provided atomic insights on the lithiation process of Si nanomaterials and suggested that volume expansion occurs primarily at the amorphous state. However, the presumed lithiation direction due to the sample geometries in the tip-based open cells may introduce anisotropic effects that deviate from the real behaviors of the Si anode. One way to avoid anisotropic effects is to study these nanomaterials in a liquid environment. Liquid-phase TEM has also been widely used for Si materials. Among the earliest studies applying *in situ* liquid-phase TEM for battery materials, Gu et al. used a SiN_x liquid cell to examine the lithiation process of Si nanowires in an EC/DMC liquid electrolyte, a common electrolyte combination used in practical lithium batteries (Figure 5a). As Si nanowires were submersed with liquid electrolyte, nanowires exhibited an isotropic volume expansion with lithiation from all orientations, rather than the directional lithiation as observed in the open cells.[40] Surprisingly, the core−shell structure was captured both in closed-cell and open-cell configurations after lithiation, indicating a fast lithium conduction on the surface of Si nanowires (Figure 5b). Although it was not able to achieve a spatial resolution as high as the open-cell configuration, the SiN_x liquid cell allowed the use of liquids that emulate the practical environment during charging and discharging and holds great potential for studying the impact of different electrolytes on the SEI formation.[40] Figure 5c shows the results where the graphene liquid cell was employed to study the lithiation mechanism of Si nanoparticles, and a preferred lithiation orientation was observed. When the electron beam induced the lithium insertion into Si nanoparticles, the lithiation preferably occurred along the <110> crystal orientation with volume expansion along the same direction.[42] Such anisotropic volumetric changes cast a discrepancy regarding the manner of lithium diffusion into the Si anode through a liquid electrolyte, when compared with the results in the SiN_x liquid cell. Possible reasons include the types of stimuli and the crystallite shapes, which might lead to different lithiation behaviors of such nanomaterials in liquid electrolytes.

3.1.2. Nanomechanics Associated with Si Anode. Due to the drastic volumetric changes of Si materials during

https://doi.org/10.1021/acs.chemrev.4c00507
Chem. Rev. XXXX, XXX, XXX−XXX

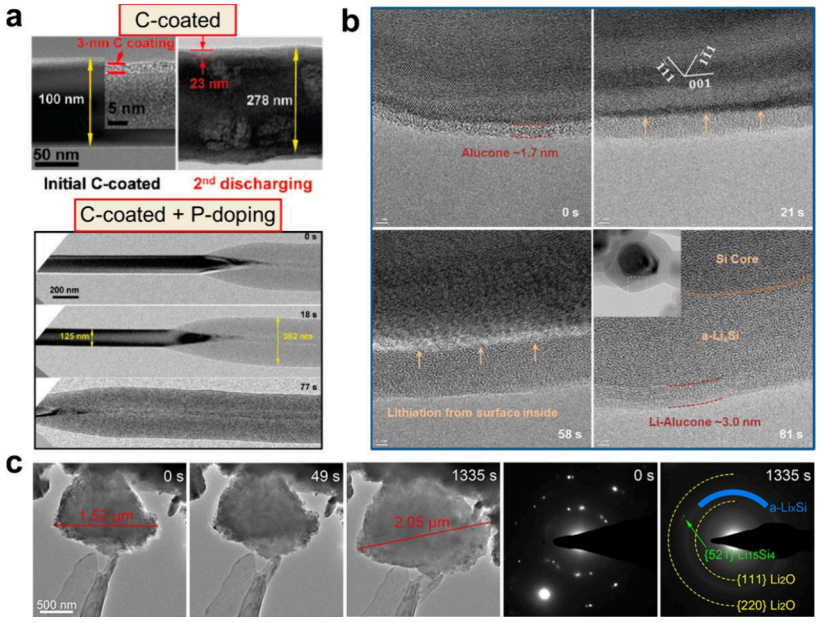

Figure 7. Anode modification for suppressing volumetric changes of Si nanomaterials. (a) Morphology changes of Si NW with C coating or an extra P doping during high-rate cycling. Reproduced with permission from ref 87. Copyright 2011 American Chemical Society. (b) HRTEM image revealing details of the alucone-coated Si nanoparticle lithiation process. Arrows indicate the reaction front. Reproduced with permission from ref 88. Copyright 2014 American Chemical Society. (c) Lithiation of porous Si particles and corresponding SAED patterns. Reproduced with permission from ref 89. Copyright 2016 The Authors.

electrochemical lithiation and delithiation, one of the major concerns of the Si anode is the electrode pulverization after repeated cycling that not only sacrifices the structural integrity of the anode but leads to electrolyte consumption and SEI formation. The consequence is severe performance degradation and potential safety issues. *In situ* TEM provides a way to use atomistic resolving power to examine the mechanical properties of the Si anode. Thereby numerous studies have been documented.

By using the tip-based open-cell configuration, Liu et al. unveiled that the fracture of Si nanoparticles is strictly associated with the particle size, where particles with diameters larger than 150 nm would experience fracture during the first lithiation (Figure 6a). The accumulated hoop tension on the surface is proposed to be the key for such mechanism.[82] Altering the particle sizes will surely help alleviate the electrode pulverization, while tuning the spherical particle morphology and crystalline nature might further mitigate the undesired impact, as amorphous nanoparticles did not show cracking at sizes larger than 400 nm in another study.[80] McDowell et al. applied tip-based open cell to study the reaction mechanism of Si nanoparticles loaded on a Si nanowire (Figure 6b). The particle fracture was also observed when the particle size exceeded 150 nm. In the meantime, it was uncovered that the reaction front migrates faster at the beginning of particle lithiation and slows down as the lithiation depth increases. The mechanical stress built up at the reaction front, namely the interface between Si and Li_xSi, is proposed to be the driving force for the rate change.[83]

The host materials also play a critical role in the mechanical aspect of the Si anode. Adkins et al. observed pore formation inside Si nanowires that were coated with a SiO_x shell in a tip-based open cell (Figure 6c). As lithium ions are removed from Si nanowires during delithiation, Si nanowires shrink while the SiO_x shell tends to hold the structure of the composite electrode, resulting in the pore formation inside Si nanowires.[84] The observed mechanism is important for practical use, as SiO_x is often used in combination with Si materials in the anode. The volume change mismatch between these species might lead to mechanical degradation of the composite electrode. In another study using Si particles embedded within carbon nanofibers (CNFs), the fracture of the carbon host was observed during the repeated volumetric changes of the active materials (Figure 6d).[85] Stress field simulation unveiled that the cracking of carbon shell initiates at the interface between Li_xSi and host. It was then predicted that a lithiation layer over 10 nm in thickness could lead to cracking in the core−shell structure using an amorphous carbon host. Such results emphasized the importance of exploring the proper spatial correlation of silicon nanoparticles with the carbon matrix when using a Si-graphite composite anode instead of a pure Si anode.[86]

3.1.3. Electrode Modification for Suppressing Volume Changes. As Si anodes experience large volume changes during charging/discharging, different strategies for mitigation have been proposed. *In situ* TEM has been an effective way to observe such an impact of the modification.

Liu et al. coated Si NWs with a 3 nm-thick carbon layer, and no obvious pore formation or fracture was seen after fast cycling (Figure 7a). Further doping of phosphorus into Si NWs, for the sake of improving electrical conductivity, achieved an ultrafast lithiation rate without fracture. Although the diameter of the Si nanowire changed from 125 to 362 nm, a volume change of nearly 300%, the Si nanowire was able to be fully lithiated and then delithiated without fracture or pore formation.[87] The structural compatibility between Si nanowires and thin carbon coating, in addition to the improved electrical conductivity, might be the key for the mechanical stability in this case. Figure 7b shows a surface modification by adding an alucone layer on Si particles. The mechanical

https://doi.org/10.1021/acs.chemrev.4c00507
Chem. Rev. XXXX, XXX, XXX−XXX

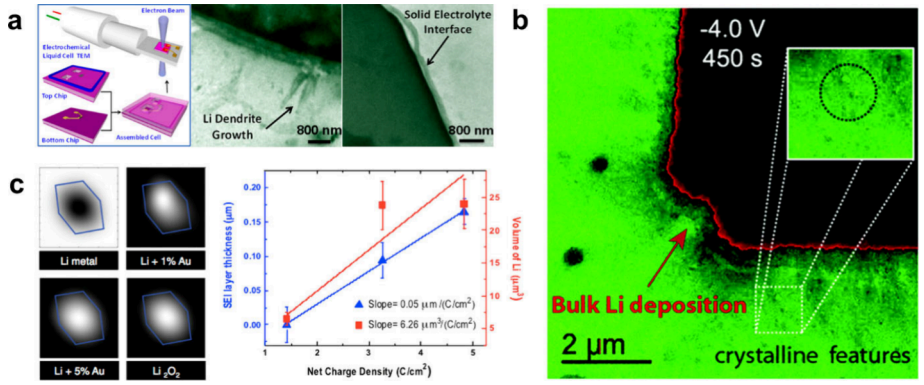

Figure 8. Early studies for visualizing lithium metal growth using *in situ* electrochemical liquid-phase TEM. (a) Experimental design of liquid cells for *in situ* electrochemical liquid-phase TEM and resultant images of lithium dendrite growth and SEI formation on an Au electrode in 1 M $LiPF_6$ in the EC/DEC electrolyte. Reproduced with permission from ref 41. Copyright 2014 American Chemical Society. (b) Li and SEI growth on an Au electrode observed during electrochemical reaction in 1.2 M $LiPF_6$ in EC/DMC electrolyte. Reproduced with permission from ref 96. Copyright 2014 Royal Society of Chemistry. (c) Simulated dark-field images of lithium compounds and net charge density calculated from CV measurements during the lithiation, used for quantifying *in situ* electrochemical liquid-phase TEM experiments. Reproduced with permission from ref 97. Copyright 2015 American Chemical Society.

flexibility and chemical stability of alucone resulted in deep lithiation of the Si nanoparticles without pulverization. However, the limited volumetric change might cause a reduced capacity of Si particles.[88] In Figure 7c, Shen et al. explored the potential of employing porous Si to suppress the drastic volume change. A porous Si particle with a size of 1.52 μm changed to 2.05 μm after lithiation, experiencing a much-reduced volume change.[89] The critical fracture size was increased up to 1.5 μm. Besides, the small crystalline domains inside porous Si have also promoted the full lithiation to form a crystalline $Li_{15}Si_4$ phase.

Due to the drastic volume change during lithiation and delithiation, Si electrode modification has been an effort to seek a balance between reduced pulverization and retained electrode capacity. On the one hand, the electrode suffers less from pulverization when the volume change is mitigated via surface coating or spatial refinement. However, this merit comes with a reduced capacity as the volume expansion is directly connected to the amount of lithium stored in the electrode. *In situ* TEM helps to find the stage at which the volume expansion of the Si electrode remains relatively steady while lithium ions come into the electrode.

Owing to its research attention and excellent contrast under electron beam, Si anodes have been extensively studied via *in situ* TEM in the past few decades. The insights obtained at the nanoscale include understanding the lithiation mechanism, mechanical degradation, solutions to undesired volumetric changes, etc. Many of these insights cannot be captured by other techniques due to insufficient spatial resolution, or the inability to apply electrochemical stimuli. *In situ* TEM has granted access to dynamic changes within Si materials, enabling the acquisition of nanoscale insights applicable to practical bulk-scale anode production. With increasing attention on Si-graphite anodes in recent years, *in situ* TEM would continue offering new knowledge necessary for further advancements.

3.2. Lithium Metal

The Li metal anode stands out among various anode candidates as a key enabler for high energy density, owing to its high theoretical capacity (3,860 mAh g^{-1}) and low electrode potential (−3.04 V vs. SHE). However, fundamental challenges persist in front of Li metal battery commercialization, such as inactive lithium formation, low Coulombic efficiency, and dendritic growth, which potentially lead to short circuits and safety concerns. Extensive studies have been conducted to comprehend the principles of lithium dendritic evolution during plating and stripping, where various factors influencing lithium dendritic growth were proposed, including the high current density that overwhelms the lithium-ion diffusion rate,[90] stress accumulations during lithium plating beneath the SEI,[91] and the ionic conductivity vs. mechanical properties of SEI components.[92,93] In response to the current understanding of lithium growth mechanisms, numerous strategies to inhibit lithium dendrites have been reported. These approaches involve SEI engineering through electrolyte optimization or the use of artificial layers, electrode modification employing lithiophilic host materials and 3D structures, and cell configurations designed using pressure, temperature, and external fields.[94,95]

In situ TEM has provided the chance to directly observe the plating and stripping processes of lithium at the nanoscale under diverse conditions. Obtained insights unveil properties of the SEI and inactive lithium that are hardly accessible with other probing tools. In this section, we reviewed the achievements of *in situ* TEM to better understand lithium evolution principles using both closed-cell and open-cell configurations, and discuss how such knowledge contributes to developing practical Li metal batteries.

3.2.1. Li Metal Nucleation and Growth Mechanisms.

The high sensitivities of Li metal and liquid electrolytes to air and moisture have posed outstanding challenges to TEM observations for many years. The nature of closed cells using *in situ* liquid cell TEM offered a way to monitor Li metal behaviors during growth and dissolution. With a SiN_x liquid cell, Zeng et al. first visualized the dendritic growth of Li metal in real-time using a practical electrolyte that consists of 1 M $LiPF_6$ in EC/DEC solvents[41] (as shown in Figure 8a). The cyclic voltammetry (CV) method was applied to a symmetric cell using Au working/counter electrodes within a voltage range of 0 to −3 V to induce lithium plating on the electrode. Following the initial Li−Au alloying reaction, the formation of a film-like SEI on the counter electrode during the negative sweeping of the cell was observed, besides the dendritic growth

https://doi.org/10.1021/acs.chemrev.4c00507
Chem. Rev. XXXX, XXX, XXX−XXX

of Li metal. This work demonstrated the promise of using a confined liquid environment to study the kinetics of Li metal growth, and showed the tendency of promoting dendritic Li when the applied current density was not well controlled.

Later, another *in situ* TEM work employed a liquid electrolyte consisting of 1.2 M $LiPF_6$ in EC/DMC (Figure 8b).[96] Au electrodes were used in the SiN_x liquid cell, and CV was applied as the electrical stimuli. Dendritic growth of Li metal and the SEI was found on the Au electrode surface, which turned out to be affected by the electric field and current distribution gradients. It was also demonstrated that Li deposition could initiate through the grown SEI, possibly due to the high ionic conductivity of the SEI or inactive lithium residuals in the SEI. Mehdi et al. further quantified the lithium and SEI growth obtained with *in situ* liquid-phase TEM, by correlating morphological changes with the electrochemical data.[97] A repetitive Li metal plating/stripping onto a Pt electrode using 1.0 M $LiPF_6$ in propylene carbonate (PC) electrolyte was first achieved, and the contrast reversal of lithium metal within the electrolyte in high-angle annular dark-field STEM (HAADF-STEM) images was interpreted via image simulations in Figure 8c. By correlating *in situ* STEM images of deposited Li/SEI and the net charge density measured from the corresponding CV curves, the authors quantitatively compared the growth rates of Li and the SEI, demonstrating the potential to link irreversible capacity with specific electrode events.

Li deposition on a glassy carbon electrode was investigated via STEM imaging by Sacci et al.[98] SEI formation on the electrode surface was captured before Li nucleation, and ADF-STEM images revealed that the SEI was approximately twice as compositionally dense as the liquid electrolyte. It was observed that Li nucleation occurred between the glassy carbon electrode and the SEI, leading to a transition to mass-transport-limited deposition. The growth of Li metal initiating between the SEI and the electrode is a prevalent belief in the field while *ex situ* experiments were not able to provide direct evidence of such a phenomenon. Dachraoui et al. observed the formation of a mosaic SEI layer on a glassy carbon electrode immersed within 1 M $LiPF_6$ in the EC/DEC liquid electrolyte.[99] They identified the initial nucleation of inorganic nanoparticles, followed by the transformation of island-like structures into a dispersed layer and subsequent densification, which eventually forms the mosaic SEI layer comprising both organic and inorganic compounds. Such direct observations have provided strong experimental evidence of modern SEI formation theories, and are of critical importance to electrolyte engineering.

Electrochemical growth/dissolution mechanisms of individual Li deposits under various conditions were proposed by *in situ* liquid-phase TEM studies. Kushima et al. elucidated Li growth behaviors in the early stage using a SiN_x liquid cell that consists of an Au working electrode with a $LiCoO_2$ counter electrode and a 1 M lithium bis(trifluoromethanesulfonyl)-imide (LiTFSI) in dimethyl sulfoxide (DMSO) electrolyte (Figure 9a).[100] In several earlier works, it was proposed that Li dendritic growth occurs during the transition of electrochemical reactions from charge-transfer-limited to diffusion-limited processes at the so-called Sand's time.[90,102,103] Kushima et al. proposed Li growth mechanisms that focus on the early stage,[100] which suggested that the competition between the rates of Li deposition and SEI formation determines whether Li grows on the surface or from the root of Li deposits. At

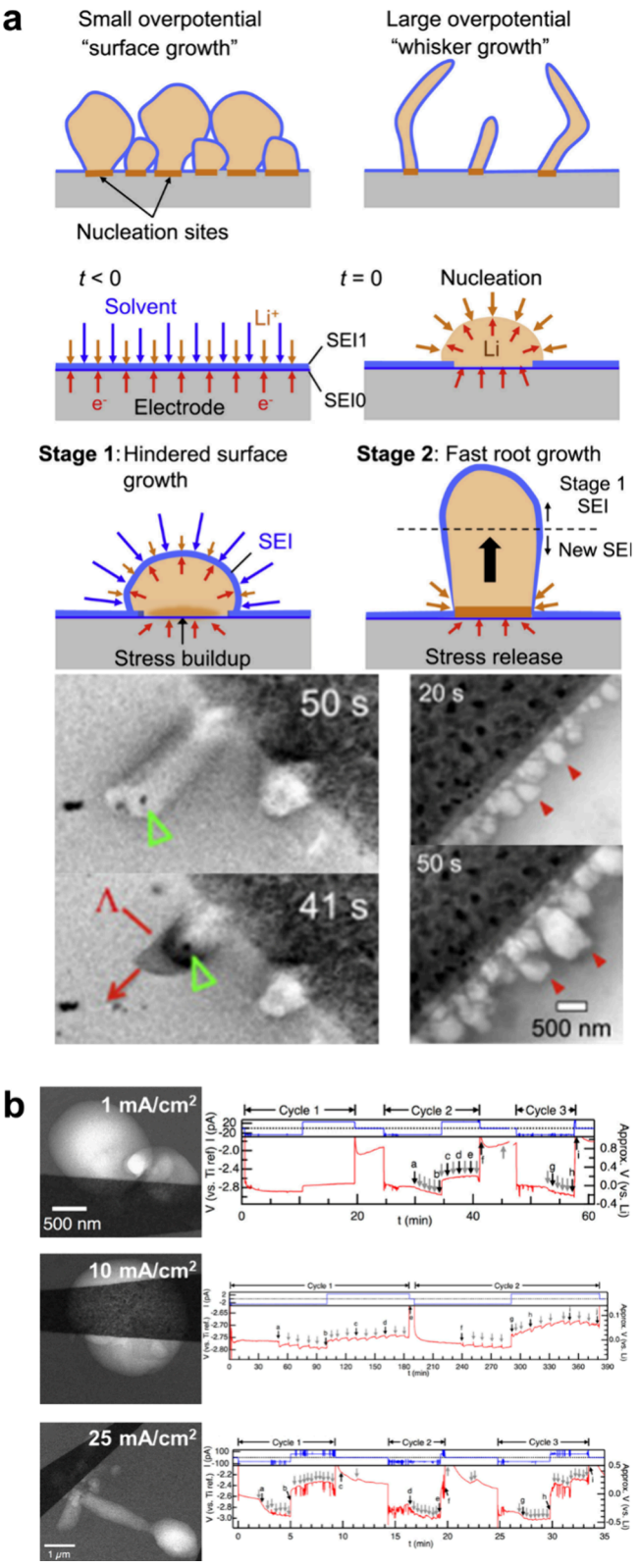

Figure 9. Mechanistic studies of electrochemical lithium growth and dissolution using *in situ* electrochemical liquid-phase TEM. (a) Dependence of lithium metal growth on the overpotential. Reproduced with permission from ref 100. Copyright 2016 Elsevier Ltd. (b) Dependence of lithium metal growth on current density. Reproduced with permission from ref 101. Copyright 2015 American Chemical Society.

https://doi.org/10.1021/acs.chemrev.4c00507
Chem. Rev. XXXX, XXX, XXX−XXX

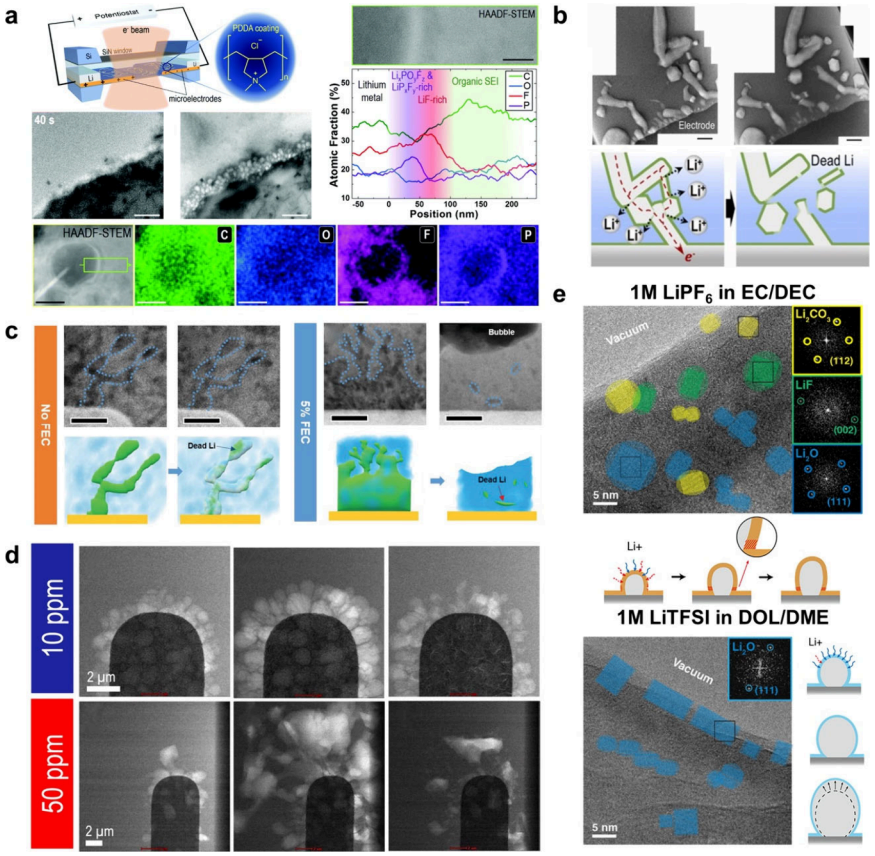

Figure 10. *In situ* electrochemical liquid-phase TEM studies on lithium dendrite suppression strategies. (a) Nanogranular lithium metal growth and SEI modification induced by an artificial electrode coating layer with a cationic polymer film. Scale bars for TEM images, HAADF-STEM image and corresponding EDS elemental maps, and HAADF-STEM image for EDS line-scan profiles: 1 μm, 200 nm, and 50 nm, respectively. Reproduced with permission from ref 43. Copyright 2020 Royal Society of Chemistry. (b) Stripping behaviors of nanogranular and dendritic lithium. Scale bars: 1 μm. Reproduced with permission from ref 107. Copyright 2022 Elsevier Ltd. (c) Dependence of lithium metal growth on FEC electrolyte additive. Reproduced with permission from ref 108. Copyright 2021 The Authors. (d) Lithium metal plating and stripping in the presence of trace H_2O in liquid electrolyte. Scale bars: 2 μm. Reproduced with permission from ref 109. Copyright 2016 The Authors. (e) Comparison of initial lithium growth behaviors in 1 M $LiPF_6$ in 1:1 EC/DEC and 1 M LiTFSI in 1:1 DOL/DME electrolytes. Reproduced with permission from ref 110. Copyright 2023 American Chemical Society.

intermediate overpotentials (e.g., ~0.1 V vs. Li/Li^+), the SEI is relatively thin, allowing Li to continuously grow uniformly and densely on its surface, forming a cauliflower-shaped morphology. However, under a large overpotential (e.g., <−0.5 V vs. Li/Li^+), a denser and thicker SEI, nonconductive to Li ions, can be rapidly formed on the electrode. In this case, Li is expected to nucleate at SEI cracks on the electrode and is compelled to grow in a whisker shape from the roots, where compressive stress has accumulated and the SEI is relatively thin. This study also provided insights into inactive Li formation. During Li stripping, it was observed that isolated inactive Li can be formed at a kink in a Li whisker, which has developed during the Li whisker growth while the compressive stress was relaxed and subsequently reaccumulated.

The effects of current densities on Li growth behavior were studied by Leenheer et al.,[101] where repetitive plating and stripping of Li metal were conducted at varying current densities of 1, 10, and 25 mA cm^{-2}. This work realized Li plating/stripping in liquid-phase TEM controlled via galvanostatic control, in contrast to the voltametric cycling protocol employed in other previous studies. The authors visualized the reinforcement of needle-like Li growth under increased current densities, in consistency with practical Li metal batteries (Figure 9b).[104,105] Smooth lithium deposits were formed at a current density of 1 mA cm^{-2}, exhibiting a high reversibility. At 10 mA cm^{-2}, Li grew into grains with facet edges in the first cycle, transitioning to a granular, needle-like morphology in the second and third cycles. At a significantly higher current density of 25 mA cm^{-2}, Li needles were observed even during the first cycle, which became more pronounced in the second and third cycles. Furthermore, the electron beam effect on Li growth morphology was investigated. It was found that Li metal tends to grow as balloon-like nodules when exposed to electron beam, in contrast to the faceted lithium grains observed without electron beam irradiation. It was then proposed that such a change might be because the electron beam creates numerous reduced radicals in the electrolyte, and the SEI attached to the Li subsequently promotes the isotropic growth. From the experiment, it was also observed that the electron beam effects are less significant at lower current densities. These phenomena were observed at a low electron dose rate of 0.1 e^- $Å^{-2}$ s^{-1} and a total dosage of 0.5 e^- $Å^{-2}$ $frame^{-1}$ during STEM imaging at a 300 kV acceleration voltage. The threshold for modifying lithium growth may vary in diverse experimental environments, including factors like SiN_x window/electrolyte thickness, electrolyte species, and the acceleration voltage of the electron beam. Nevertheless, this

https://doi.org/10.1021/acs.chemrev.4c00507
Chem. Rev. XXXX, XXX, XXX−XXX

result emphasizes the crucial need to meticulously quantify the impact of the electron beam on *in situ* TEM experiments.

It is also noteworthy that the differences in Li growth behavior between liquid-phase TEM cells and conventional coin cells were investigated by Harrison et al. using a 4 M LiFSI in a dimethoxyethane (DME) electrolyte.[106] They revealed that cell compression directly affects Li deposit morphology, CE, and self-discharge behaviors. Li metal grown in coin cells tends to appear denser and more uniform, whereas in liquid-phase TEM cells without pressure confinement, Li deposits become mossy and dendritic. It was suggested that cell pressure affects the SEI formation, which plays a major role in Li plating/stripping. A loose SEI can be formed at low cell pressure, directly affecting Li morphology and CE. Additionally, Li self-discharge occurred rapidly in liquid-phase TEM cells, possibly due to the insufficient shielding of a loose SEI on Li deposits from the electrolyte and potential electron beam effects. A further test showed that self-discharge was successfully prevented using a $LiAl_{0.3}S$ coating owing to its protective effect on Li metal as an artificial SEI. These findings underscore the importance of considering the unique environment provided by liquid-phase TEM cells when investigating Li plating/stripping behaviors and how the nanoscale knowledge could be translated to bulk cells.

3.2.2. Engineering Efforts for Regulating Li Metal Growth. Besides the efforts to elucidate the growth mechanisms of Li dendrites typically observed in practical liquid electrolytes, there have been studies to unravel the underlying mechanisms of several promising strategies that were researched for enhancing Li metal batteries (Figure 10).[43,107−110]

Lee et al. investigated mechanisms for suppressing Li dendrites using an artificial coating layer on the electrode, employing *in situ* electrochemical liquid-phase TEM as shown in Figure 10a.[43] In this work, a cationic polymer film, specifically poly(diallyldimethylammonium chloride) (PDDA), was applied onto the electrode within a liquid cell. To achieve a thin and uniform coating within a liquid TEM cell with a height of tens of nanometers, PDDA was electrostatically coated onto $Sn@SnO_2$ nanorods. The PDDA-coated nanorods were then dispersed onto the electrode, preventing agglomeration of the PDDA film during the drying process. Due to high contact resistance, the $Sn@SnO_2$ nanorods did not participate in electrochemical reactions, as confirmed by the constant volume observed throughout the reaction. This approach allowed them to reveal the impact of the artificial coating layer on Li growth. Direct observations of nanogranular Li growth and a uniform LiF-rich SEI on each Li deposit unveiled the SEI-driven modification mechanisms of Li growth. Notably, the detailed elemental distribution of the SEI on Li deposits was successfully visualized using STEM-EDS in a liquid-phase TEM experiment, which manifests a layer-by-layer SEI structure. Moreover, this research contributed to validating the efficacy of *in situ* TEM results by demonstrating their alignment with experimental outcomes conducted on actual coin cell batteries. The following study reported the Li-stripping processes, revealing three possible stripping modes of Li nanogranules grown under PDDA film: symmetric stripping mode, surface-preferred asymmetric stripping mode, and interface-preferred asymmetric stripping mode.[107] Specifically, the interface-preferred asymmetric stripping, signifying preferential Li stripping at the interfaces of lithium/electrode or lithium/lithium, can be a critical mechanism for the formation of inactive lithium, for both nanogranular and typical dendritic Li (Figure 10b). In addition, it was found that Li stripping is accompanied by SEI loss, emphasizing the importance of strategies to preserve previously formed SEI layers during repeated cycling.

Gong et al. utilized *in situ* liquid-phase TEM to investigate the influence of fluoroethylene carbonate (FEC) electrolyte additive on Li plating/stripping, which has been frequently reported to enhance the cyclability of Li metal batteries (Figure 10c).[108,111−113] *In situ* TEM captured that the addition of 5% FEC into a 1 M $LiPF_6$ in 1:1 EC/DMC electrolyte improved Li dendrite interconnectivity, leading to the suppression of inactive Li formation during stripping. Combined with nuclear magnetic resonance (NMR), online mass spectrometry (MS), secondary ion mass spectrometry (SIMS), and electrochemical impedance spectroscopy (EIS) studies, this effect was attributed to the formation of an F-rich SEI, e.g., LiF, from FEC additive, resulting in the denser plating and more uniform stripping of lithium.

Furthermore, Mehdi et al. studied the effect of trace H_2O in the electrolyte on Li growth behaviors, as shown in Figure 10d.[109] The authors observed that the electrolyte with H_2O of 50 ppm induces larger Li grains compared to that with H_2O of 10 ppm, along with a better reversible stripping behavior, supporting their previous findings from other experiments of Li metal batteries.[114] It was speculated that this difference might arise from the increased HF concentration in the presence of H_2O, leading to the formation of a LiF-rich SEI layer that facilitates rapid Li-ion diffusion.

The influence of the electrolyte species on the initial stages of Li plating was also explored through liquid-phase TEM by Park et al.[110] This study compared the initial Li growth using 1 M $LiPF_6$ in 1:1 EC/DEC and 1 M LiTFSI in 1:1 1,3-dioxolane (DOL)/DME electrolytes. The DOL/DME system exhibited a higher Li nucleation overpotential of −3.2 V (vs. Pt pseudoreference) compared to the EC/DEC system at −4.1 V (vs. Pt pseudoreference). Although fewer nuclei were observed in the DOL/DME system, it showed much faster and more drastic growth, forming larger grains, as shown in Figure 10e. The accompanying cryo-TEM analysis revealed that the EC/DEC electrolyte produced an uneven SEI containing Li_2CO_3, LiF, and Li_2O, while the DOL/DME electrolyte formed a uniform multilayered Li_2O and a flexible SEI, which could result in fewer lithium nuclei and larger grains.

3.2.3. Li Growth and Transport in Carbon Host. Offering superior spatial resolution compared to liquid-phase TEM, open-cell *in situ* TEM studies yielded invaluable insights into Li plating/stripping, mechanical properties, and SEI formation utilizing unconventional electrolytes. Zheng et al. employed SEM imaging and the *in situ* TEM capability to investigate the interaction between Li metal and a surface coating composed of a monolayer of amorphous hollow carbon nanospheres.[115] To form hollow carbon nanospheres on the Cu substrate, polystyrene nanoparticles were first used as a template and coated with a thin layer of amorphous carbon. The coated nanoparticles were then heated at 400 °C under an inert atmosphere, resulting in the formation of hollow carbon nanospheres. It was found that Li nucleation occurred beneath the carbon layer, resulting in a more uniform and stable growth behavior. Through combined *in situ* TEM and electrochemical characterizations, this study suggested the potential of amorphous hollow carbon nanospheres for nanoscale interfacial engineering.

https://doi.org/10.1021/acs.chemrev.4c00507
Chem. Rev. XXXX, XXX, XXX−XXX

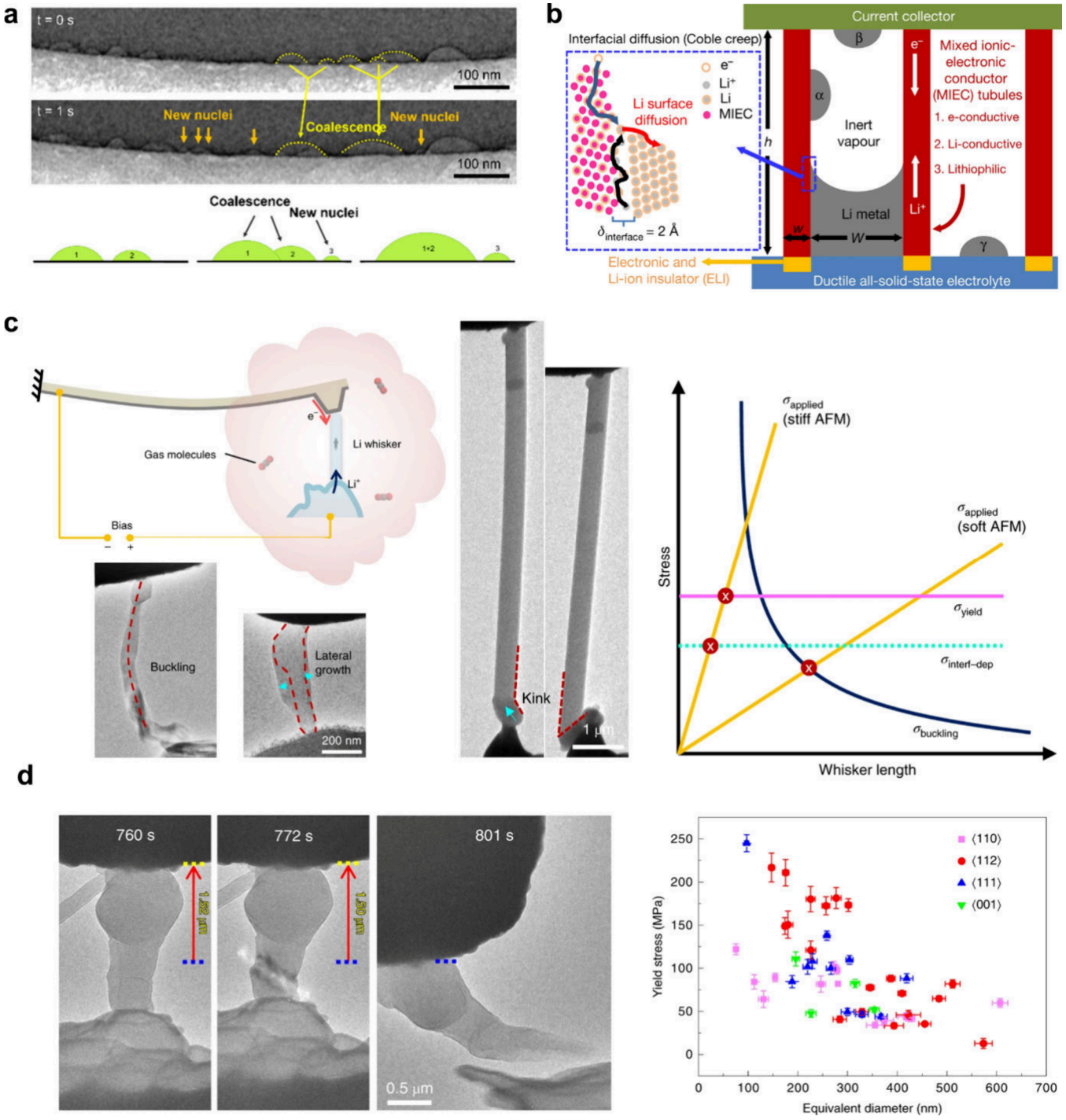

Figure 11. *In situ* electrochemical TEM studies on lithium metal growth mechanisms using the open-cell configuration. (a) Lithium metal nucleation and growth on carbon fibers. Reproduced with permission from ref 116. Copyright 2023 American Chemical Society. (b) Lithium metal growth inside ZnO_x-incorporated hollow carbon tubules. Reproduced with permission from ref 117. Copyright 2020 The Authors under exclusive license to Springer Nature Limited. (c, d) Lithium metal whisker growth and its mechanical characteristics investigated by *in situ* AFM-TEM in a CO_2 gas environment. Reproduced with permissions from refs 119, 120. Copyright 2019 This is a U.S. government work and not under copyright protection in the U.S., and Copyright 2020 The Authors, under exclusive license to Springer Nature Limited.

In the experimental setup of the open-cell *in situ* TEM configuration, thin carbon fibers are frequently used as mediators to facilitate the contact between two electrodes at the nanoscale. Several studies leveraged this characteristic to explore the fundamentals of Li growth dynamics. For example, Wang et al. investigated the nucleation and growth of Li metal on the carbon fiber (Figure 11a), reporting the transition of Li metal from droplet-shaped NPs to faceted crystals.[116] It was observed that the fusion of Li deposits on the carbon surface leads to the coalescence of droplet-shaped Li particles, which later transform into faceted crystals for surface energy reduction as they grow. Along with the TEM observations, molecular dynamics (MD) and Monte Carlo calculations further clarified the four key stages of Li deposition: nucleation

https://doi.org/10.1021/acs.chemrev.4c00507
Chem. Rev. XXXX, XXX, XXX−XXX

of amorphous clusters, crystallization, migration−fusion of clusters, and particle growth. During the fusion process, smaller clusters align with the crystallographic orientation of larger ones, and grain boundary migration causes these boundaries to disappear, eventually forming a single crystal. Moreover, their statistical interpretations of *in situ* TEM data indicated instantaneous Li nucleation in the early stage followed by saturation, which exhibits a combined form of the conventional instantaneous nucleation model and the progressive nucleation model.

Chen et al. exploited tip-based open-cell *in situ* TEM using mixed ionic-electronic conductor (MIEC) tubules as 3D Li hosts for Li metal batteries (Figure 11b).[117] It was directly observed that single-crystal Li inside the ZnO_x-incorporated hollow carbon tubules was able to plate and strip via diffusional Coble creep mechanism. Such a setup later demonstrated excellent cycle performance in an all-solid-state battery tested with a $LiFePO_4$ cathode and a poly(ethylene oxide) (PEO)-based/LiTFSI thin film solid electrolyte. The Li_2O layer that was formed by the conversion reaction between ZnO_x and Li during the lithiation could act as a lithiophilic layer, leading to the complete and rapid wetting of Li metal on the MIEC surface during growth. Another Li host strategy used TiO_2 as the seeding layer.[118] Sun et al. utilized TiO_2 as intercalation-type lithiophilic seeds in nitrogen-doped hollow porous carbon spheres (N-HPCSs). Open-cell *in situ* TEM demonstrated the Li plating/stripping behaviors on Ag and TiO_2 nanoparticles in N-HPCSs, where the TiO_2 nanoparticles exhibited good reversibility during the whole process, indicating that intercalation reaction materials could be reversibly used as lithiophilic seeds.

3.2.4. Mechanical Considerations during Li Metal Growth. Open-cell *in situ* TEM experiments can be combined with controlled gas environments, namely environmental TEM, to understand SEI-dependent Li growth behaviors. In particular, the influences of stress during the lithium growth were studied by leveraging an atomic force microscope (AFM) cantilever capable of *in situ* stress measurement.[119,120] As illustrated in Figure 11c and 11d, the axial stress ranges that could deform lithium whiskers during growth were estimated through direct observations of Li whisker growth under a soft or stiff AFM cantilever in CO_2 environment. He et al. proposed four different Li whisker behavior scenarios under elastic constraint: (i) buckling, (ii) kinking, (iii) yielding, and (iv) termination of deposition at the interface. The authors interpreted each phenomenon as a result of the competition between critical stresses based on the length of Li whiskers and applied stress, as summarized in Figure 11c. Instead, Zhang et al. focused more on establishing the dependence of Li whisker diameters and growth directions on the critical stresses for deformation, as shown in Figure 11d.[120] Maximum stress before Li necking during the growth and the yield strength measured with as-grown Li demonstrate a decreasing trend with larger diameter of Li whiskers regardless of their growth direction. It was found that the lithium whisker growth stress reaches up to 130 MPa and their measured yield strength reaches as high as 244 MPa, which are surprisingly higher than the reported values for bulk polycrystalline lithium.

Wang et al. correlated Li stripping behaviors with the yield strength of the SEI using a tip-based solid-electrolyte open cell.[121] It was observed that the stripping behaviors of Li whiskers depend on the t/r ratio (Figure 12a), where t and r denote the thickness of the SEI and the radius of the Li

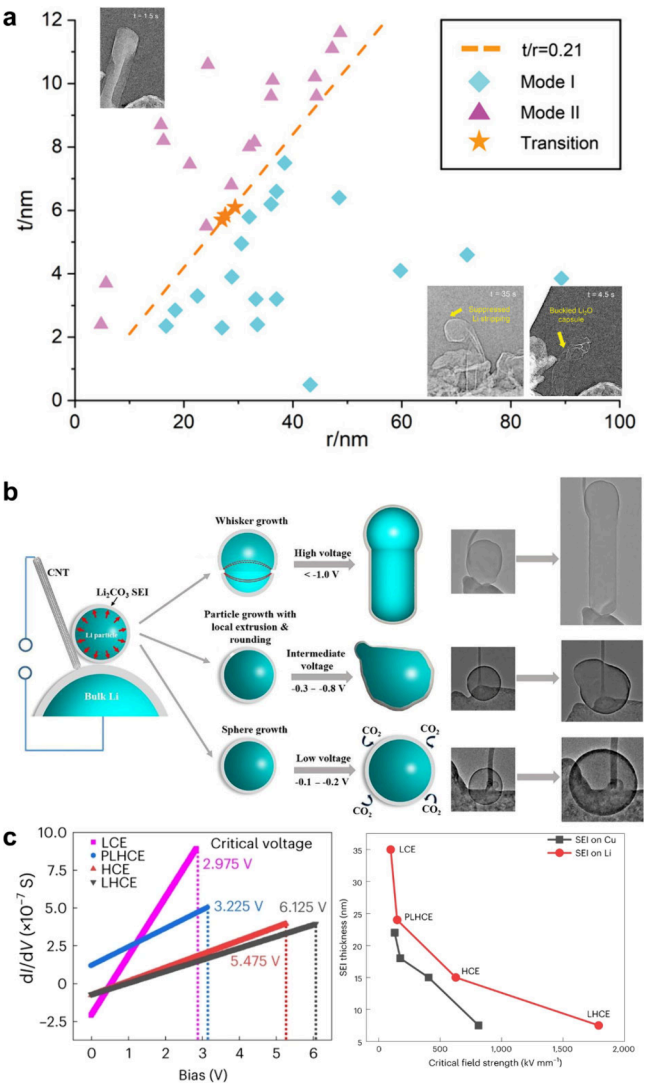

Figure 12. *In situ* TEM studies of SEI effect on lithium plating and stripping using the open-cell configuration. (a) Dependence of lithium stripping mode on the ratio of SEI thickness to Li whisker radius. Reproduced with permission from ref 121. Copyright 2022 The Authors. (b) Impact of SEI and applied voltage on lithium metal morphology in CO_2 or O_2 gas environments. Reproduced with permission from ref 122. Copyright 2021 Science China Press. (c) Comparison of SEI electrical properties formed in four different electrolyte systems. Reproduced with permission from ref 46. Copyright 2023 The Authors, under exclusive license to Springer Nature Limited.

whisker, respectively. Based on the statistical analysis, Li whiskers with high t/r ratios strip in a planar manner from the root, while those with low t/r ratios strip through multisite cavitation at the Li/Li_2O interface, resulting in severe buckling and necking. This phenomenon was proposed as the consequence of stress applied to the surface SEI during Li whisker stripping. As the stress incurred during the stripping process is dependent on the t/r ratio according to the elasticity solution for a cylindrical pressure vessel, the buckling and necking can occur under the low t/r ratio condition, in which the stress exceeds the yield strength of the SEI. This study has provided a mechanical criterion for the SEI or artificial solid structures designed to enhance lithium metal batteries.

https://doi.org/10.1021/acs.chemrev.4c00507
Chem. Rev. XXXX, XXX, XXX−XXX

The impact of the SEI on lithium morphology was also investigated by Yang et al. via *in situ* environmental TEM studies.[122] Under a CO_2 environment where Li_2CO_3 can be formed as the SEI on the lithium metal, cracking of the SEI and subsequent directional growth of the lithium whisker at this region was observed at high-voltage conditions as illustrated in Figure 12b. In contrast, the self-healing of the SEI (SEI reformation at the cracking region) outpaced lithium directional growth at the SEI crack under low-voltage conditions, resulting in spherical lithium growth. Considering the consistent spherical lithium growth regardless of the applied voltage observed under an O_2 gas environment where a Li_2O SEI could be formed, the influence of intrinsic SEI properties on the lithium growth behavior was emphasized in this study.

To further understand the impact of the SEI on Li metal behavior, Xu et al. conducted a comparative analysis to study the electrical properties of the SEI with a tip-based open cell TEM configuration (Figure 12c).[46] Copper wires, on which SEI/Li particles or solely the SEI were electrochemically formed inside a coin cell, were loaded into the open-cell holder for the *in situ* experiments. By comparing the measured $I-V$ and $dI/dV-V$ curves of SEIs with those of insulating SiO_2 and semiconducting TiO_2 as references, the differential conductance and critical field strength for the breakdown of SEIs were calculated. This work compared SEIs formed in four different electrolyte systems, including (i) low-concentration electrolyte (LCE; 1:9 lithium bis(fluorosulfonyl)imide (LiFSI)/DME), (ii) high-concentration electrolyte (HCE; 1:1.2 LiFSI/DME), (iii) localized high-concentration electrolyte (LHCE; 1:1.2:3 LiFSI/DME/bis(2,2,2-trifluoroethyl) ether (BTFE)), and (iv) pseudolocalized high-concentration electrolyte (PLHCE; 1:1.2:3 LiFSI/DME/bis(2,2,2-trifluoroethyl) carbonate (BTFEC)). Li-electrolyte interface models for each electrolyte were constructed using hybrid *ab initio* molecular dynamics (AIMD) simulations, and electron transport in the SEI was calculated in terms of the $I-V$ curve. By combining experimental and computational results, it was demonstrated that the electrical properties of SEIs resemble those of semiconductors. In addition, the SEI formed in the LHCE electrolyte exhibits the lowest rates of differential conductance and the highest critical field strength among the four electrolyte systems. This suggests that it is the most electrically insulating and stable SEI against electrical potential. The authors considered this phenomenon as the origin of the excellent cycling performance of LHCE in Li||Cu and Li|| NMC811 cells, which was further supported by *ex situ* TEM showing topographically smooth Li particles and thin SEI layers. This study provided fundamental insights into the attributes of a good SEI that could be directly correlated with practical Li metal battery performance.

To summarize, as Li metal is formed locally within the microscope, *in situ* TEM presents the advantage of observing Li metal dynamics without concerning the air sensitivity, which is why *in situ* TEM has been widely investigated in Li metal research before the vast application of cryo-EM very recently. The high resolving power and dynamic capturing capability of *in situ* TEM have generated unprecedented fundamental insights regarding Li metal nucleation mechanisms in various sample configurations, Li metal mechanics, SEI properties, etc. The obtained knowledge was directly linked with practical battery performance and has guided the engineering efforts for designing the next-generation Li metal batteries.

3.3. Carbon-Based Materials

Graphite anode is widely used in commercial lithium-ion batteries due to its excellent cycling performance and low cost. However, its limited theoretical capacity poses a challenge to achieving higher energy density while maintaining the longevity advantages of graphite. Extensive research efforts have been devoted to various carbon-based materials to address this challenge,[123−125] among which *in situ* TEM was able to elucidate the fundamental knowledge of Li-ion interactions in graphite anodes and uncover the lithiation behaviors in new carbon-based anode materials, thereby contributing to the exploration of next-generation anodes as alternatives to graphite.

Unocic et al. successfully visualized the SEI formation on the graphite anode with *in situ* liquid-phase TEM using 1 M $LiPF_6$ in EC/DEC, a practical electrolyte used in graphite cells.[126] SEI growth dynamics was captured during chronoamperometry measurement from 3.0 to 1.5 V with a 0.25 V step per 5 min. Figure 13a shows the local SEI formation at the electrode−electrolyte interface with a porous structure. An interesting phenomenon was observed when the cell potential decreased from 1.75 to 1.5 V, where a portion of the SEI abruptly fractured and rapidly reformed. The authors suggested that the SEI damage and self-healing characteristics were caused by the variations in the local electrostatic forces and the magnitude of the equipotential field lines when the applied potential changed. Dong et al. developed a highly branched N-doped graphitic tubular foam as a high-capacity Li-ion battery anode material and investigated its electrochemical reaction via *in situ* TEM.[127] In an open-cell configuration with an ionic liquid electrolyte, the *in situ* TEM observations unraveled a large expansion of interplanar spacing at the curved-wall positions, implying the relatively high capability for Li-ion storage at this region. Furthermore, it was observed that N-doping increased defects and expanded (0002) interplanar spacing, contributing to the improved capacity, rate capability, and cycling stability of the material. These findings highlight the promising potential of defect and morphology engineering in enhancing the electrochemical performance of carbon materials for Li-ion batteries.

Liu et al. investigated the mechanical properties of a multiwalled carbon nanotube (MWCNT) anode using open-cell *in situ* TEM.[128] It was observed that the lithiation process of MWCNTs accompanies the formation of a poly crystalline Li_2O layer on the surface and a 5.9%-expansion of the (0002) interplanar spacing. Despite the absence of external pressure, MWCNTs exhibited a tensile hoop stress of ∼50 GPa after lithiation due to their closed-shell geometry. Subsequent stress application to the lithiated MWCNTs resulted in brittle fracture (Figure 13b), indicating mechanical weakening induced by lithium insertion. This was attributed to the mechanical and chemical weakening of C−C bonding by lithiation, supported by molecular orbital theory calculations. This work further demonstrated the improved mechanical properties of lithiated graphene nanoribbons (GNRs) that are synthesized by longitudinal splitting of MWCNTs.[129] It showed a reversible expansion and contraction of (0002) interplanar spacing in GNRs during lithiation and delithiation, while a thin crystalline Li_2O layer remained a stable SEI (Figure 13c). *In situ* mechanical testing illustrated that lithiated GNRs had gradual bending and buckling without fracture, indicating superior mechanical stability compared to the lithiated MWCNTs. The enhanced mechanical strength of

https://doi.org/10.1021/acs.chemrev.4c00507
Chem. Rev. XXXX, XXX, XXX−XXX

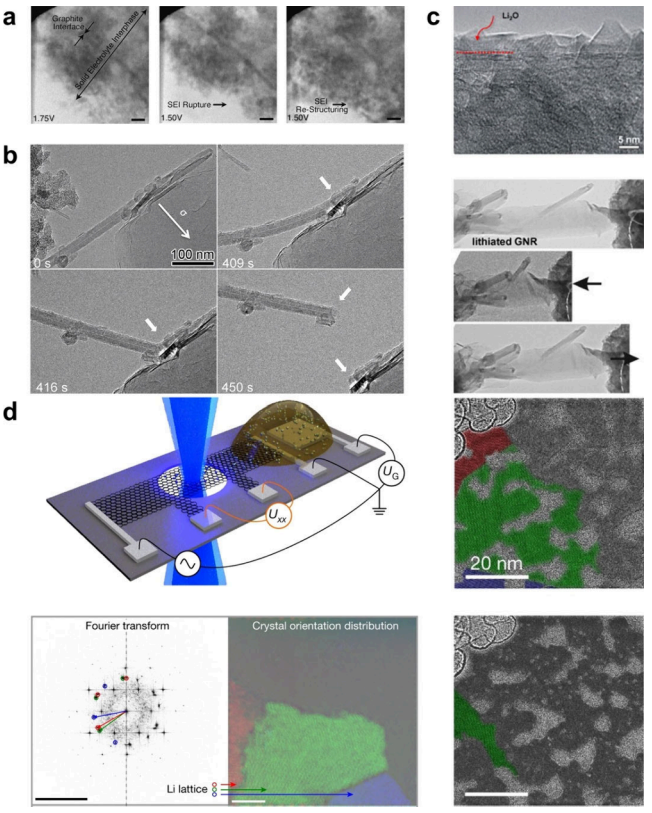

Figure 13. Investigations of lithiation and SEI formation mechanisms of carbon-based anode materials. (a) SEI formation on a graphite anode in 1 M $LiPF_6$ EC/DEC electrolyte during lithiation. Scale bars: 1 μm. Reproduced with permission from ref 126. Copyright 2014 Microscopy Society of America. (b) Enhanced brittleness of multiwalled carbon nanotubes (MWCNTs) after lithiation. Reproduced with permission from ref 128. Copyright 2011 American Chemical Society. (c) Uniform Li_2O layer formation on graphene nanoribbons (GNRs) after lithiation, including *in situ* mechanical testing of the lithiated GNRs. Reproduced with permission from ref 129. Copyright 2012 Elsevier Ltd. (d) Schematic illustration of an *in situ* TEM setup for investigating lithiation/delithiation in a graphene bilayer, accompanied by TEM images showing crystal orientations during lithiation and delithiation. Scale bars for fast Fourier transformed (FFT) pattern and corresponding HRTEM image: 10 nm^{-1} and 5 nm, respectively. Reproduced with permission from ref 67. Copyright 2018 Springer Nature Limited.

the lithiated GNRs was attributed to the stress-free vertical breathing of stacked planar graphene layers.

Later, Kühne et al. investigated Li-ion intercalation into a graphene bilayer material with an *in situ* electrochemical cell as illustrated in Figure 13d.[67] A graphene bilayer was laid on a Si_3N_4-covered Si substrate with an open hole, where electrodes were predeposited via the MEMS process. One end of the graphene bilayer was directly connected to a working electrode and the other end was indirectly connected to a counter electrode via a solid polymer electrolyte to build an electrochemical cell. The lithiation process into the graphene bilayer at the angstrom level was observed through the open-hole area, leveraging an 80 kV spherical and chromatic aberration-corrected TEM instrument. During lithiation, lattice planes with the in-plane lattice constants of 3.1 Å were observed by HRTEM image and FFT patterns (Figure 13d). This lattice constant matched well with a calculated in-plane lattice constant of the hexagonal close-packed phase, which is the energetically favorable phase determined by first-principles calculations. Moreover, the observed additional crystal was found to be a superdense Li metal based on the comprehensive interpretation of calculations and EELS experimental results. This closely packed Li grew laterally during lithiation and reversibly disappeared during delithiation, except for some residues caused by defects in the graphene lattices. This work revealed that a superdense ordering, which typically exists under extreme conditions, could be present between the two atomic layers upon lithiation of carbon material.

3.4. Metal Alloys

In addition to Si anodes, various metal materials, such as Ge, Au, Al, Sb, etc., exhibit a very high theoretical capacity for Li storage through alloying reactions, making them attractive candidates for next-generation Li-ion battery anodes. *In situ* TEM has also aided the investigations of fundamental lithiation/delithiation mechanisms of these metal alloy anodes.

Ge anodes demonstrate a comparable volumetric capacity to Si anodes, e.g., 7,366 Ah L^{-1} for Ge vs. 8,334 Ah L^{-1} for Si, but with a higher lithium diffusivity. Similar to Si anodes, a two-step lithiation process was identified for Ge nanowires via an *in situ* TEM study with an open-cell configuration.[130] This work unveiled a core−shell structural transformation and surface amorphization of Ge nanowires after lithiation, attributed to the rapid transport of lithium ions on the electrode surface. Unlike Si, Ge nanowires consistently exhibited obvious elongation in <112> directions during lithiation, while Si nanowires showed little axial elongation.[87,131] The authors observed the formation and propagation of nanopores in Ge nanowires. The nanopores were considered beneficial to battery performance in several aspects, including improved mechanical stability, fast ion transport, and stress relaxation. Liu et al. further induced axial lithiation along the <111> direction in Ge nanowires by introducing a conformal, epitaxial, and ultrathin Si shell, which was proved by *in situ* TEM experiments with an open-cell configuration.[132] The surface diffusion of lithium ions was controlled by the Si shell which has lower lithium diffusivity and a higher chemical potential compared to Ge, resulting in axial lithiation. These findings underscore the potential of interface and bandgap engineering to manipulate nanoscale ionic transport properties in Li-ion batteries. Liang et al. demonstrated the suppression of cracks in Ge nanoparticles during lithiation, as captured via open-cell *in situ* TEM.[133] The isotropic lithiation process observed in Ge nanoparticles led to crack-free lithiation, attributed to the more uniform distribution of hoop stress throughout the material. In contrast, they found that Si nanoparticles underwent severe cracking during lithiation due to the anisotropic lithiation process, resulting in nonuniform hoop stress distribution.

Figure 14a demonstrates size-dependent pore formation inside Ge nanowires coated with an amorphous Si shell.[134] It was observed that nanopores could be formed during the delithiation once the diameter of the Ge nanowire is larger than 27 nm. Gu et al. investigated the stress effect on the lithiation behaviors of Ge nanowires.[138] The stress induced by the bending of Ge nanowires led to a nonsymmetric lithiation behavior where lithiation speeded up at the tensile side and slowed down at the compressive side. By employing a coupled chemomechanical model that integrates Li diffusion and elastoplasticity, they demonstrated that stress impacts both reaction and diffusion rates. This computational approach

https://doi.org/10.1021/acs.chemrev.4c00507
Chem. Rev. XXXX, XXX, XXX−XXX

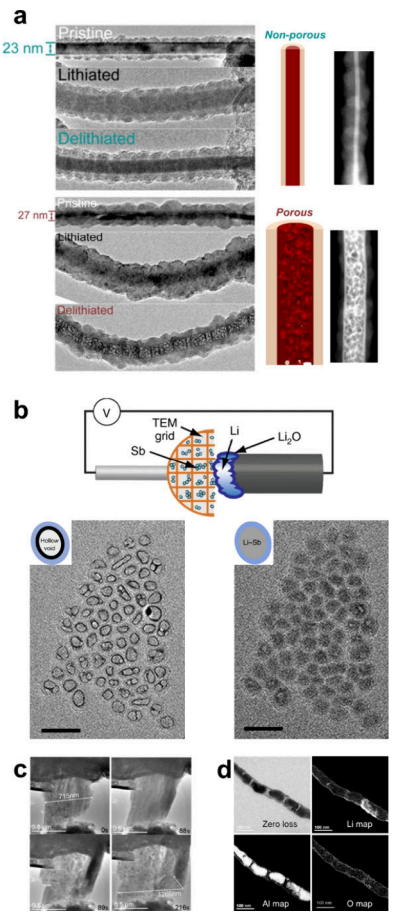

Figure 14. *In situ* TEM studies on lithiation/delithiation mechanisms of alloying anode materials. (a) Size-dependent nanopore formation in germanium (Ge) nanowires during delithiation. Reproduced with permission from ref 134. Copyright 2016 American Chemical Society. (b) Lithiation/delithiation of antimony (Sb) nanoparticles involving reversible filling and formation of nanovoids. Scale bars: 50 nm. Reproduced with permission from ref 135. Copyright 2020 The Authors, under exclusive license to Springer Nature Limited. (c) Failure of a black phosphorus (P) anode during delithiation. Reproduced with permission from ref 136. Copyright 2016 American Chemical Society. (d) Pulverization and the formation of a thin Al_2O_3 surface layer during lithiation of aluminum (Al) nanowires. Reproduced with permission from ref 137. Copyright 2011 American Chemical Society.

offered a deeper understanding of the *in situ* TEM findings, explaining the formation of an asymmetric core−shell structure driven by faster lithiation on the tensile side of the nanowire. Gan et al. utilized *in situ* TEM and off-axis electron holography to explore the dynamics of charge distribution during the lithiation of Ge nanowires, unraveling the complex interplay between positive and negative charges within the core−shell structure.[139] The mean inner potential of the lithiated Li_xGe shell decreased as lithiation progressed, while the Ge core displayed a lower mean inner potential than its theoretical value attributed to the accumulation of trapped charges at the interface. It was proposed that electrons are trapped at the interface of the Ge core, whereas lithium ions were accumulated at the interface of the Li_xGe shell, serving to balance the charge distribution.

The failure mechanisms of metal alloy materials were investigated through *in situ* TEM studies with high spatial and temporal resolutions. As the volumetric change of the alloying materials during lithiation is the key to the limited cyclability, hollow and yolk−shell structures have been proposed to stabilize the structure.[140−142] Specifically, Boebinger et al. investigated antimony (Sb) nanoparticles as a lithium-ion battery anode, revealing the formation of a uniform void after the first delithiation, which was reversibly filled and vacated during repeated lithiation and delithiation cycles (Figure 14b).[135] In contrast, the buckling of particles rather than the void formation was more prevalent for larger Sb particles. Based on these findings, the authors proposed a chemo-mechanical model suggesting that mechanical constraints induced by the surface oxide film led to the void formation, emphasizing the proper particle size for improved stability.

Besides, the failure mechanism of a black phosphorus anode was investigated via *in situ* open-cell TEM,[136] which proposed the high correlation of its failure with the delithiation process rather than lithiation. As shown in Figure 14c, anisotropic expansion was observed during lithiation as a new phase evolved by the reaction with lithium ions. This phase transformation resulted in the change of orthorhombic black phosphorus to amorphous Li_xP_y. Alike the case in Li_xSi material where a congruent amorphous-to-crystalline phase transformation was observed, the transformation of amorphous Li_xP_y to crystalline Li_3P was also present in this case. Such phase transformation was predicted by MD simulation to be a kinetically favorable low-barrier transition.[143] Intriguingly, the size of the black phosphorus anode even increased during the delithiation. Such cracking and pulverization of the electrode resulted in the loss of electrical contact and contributed to capacity fading.

The pulverization of Al nanowires and the formation of a thin Al_2O_3 surface were examined via open-cell *in situ* TEM.[137] It was found that the lithiation always initiates from the surface Al_2O_3 layer, followed by the lithiation of the inner Al core, which is similar to the lithiation process observed in other alloying materials.[40,82,130] In addition, during the lithiation, it was observed that the single-crystal Al nanowire transformed into a polycrystalline LiAl alloy with volume expansion in both radial and longitudinal directions. Delithiation led to the formation of nanovoids originating from volume contraction. EELS mapping results revealed that the nanoparticle inside the nanowire is Al, while the surface layer consists of Li, Al, and O, corresponding to Li−Al−O glass (Figure 14d). This study suggested that this glass layer, known for high ionic conductivity and low electrical conductivity, acts as a solid electrolyte, maintaining a thin surface to prevent cracking or contact loss. Different from nanowires, a nanoporous Cu−Ge−Al alloy was investigated by Ma et al. using *in situ* TEM to monitor morphological and structural evolution.[144] The study showed that the porous structure can effectively accommodate volume expansion, resulting in structural stability. It was demonstrated that the structural design improvement enhances battery performance by ensuring stability during charge/discharge cycles.

Zeng et al. investigated Li−Au alloying reactions via *in situ* electrochemical liquid-phase TEM using 1 M $LiPF_6$ in EC/DEC electrolyte.[145] CV control was applied to a symmetric cell with Au working/counter electrodes. The experiments uncovered three mechanisms inducing morphological changes: gradual dissolution, explosive reactions, and local expansion/shrinkage. In Figure 15a, the gradual dissolution of the Au electrode, starting from the corner, occurred in two steps with

https://doi.org/10.1021/acs.chemrev.4c00507
Chem. Rev. XXXX, XXX, XXX−XXX

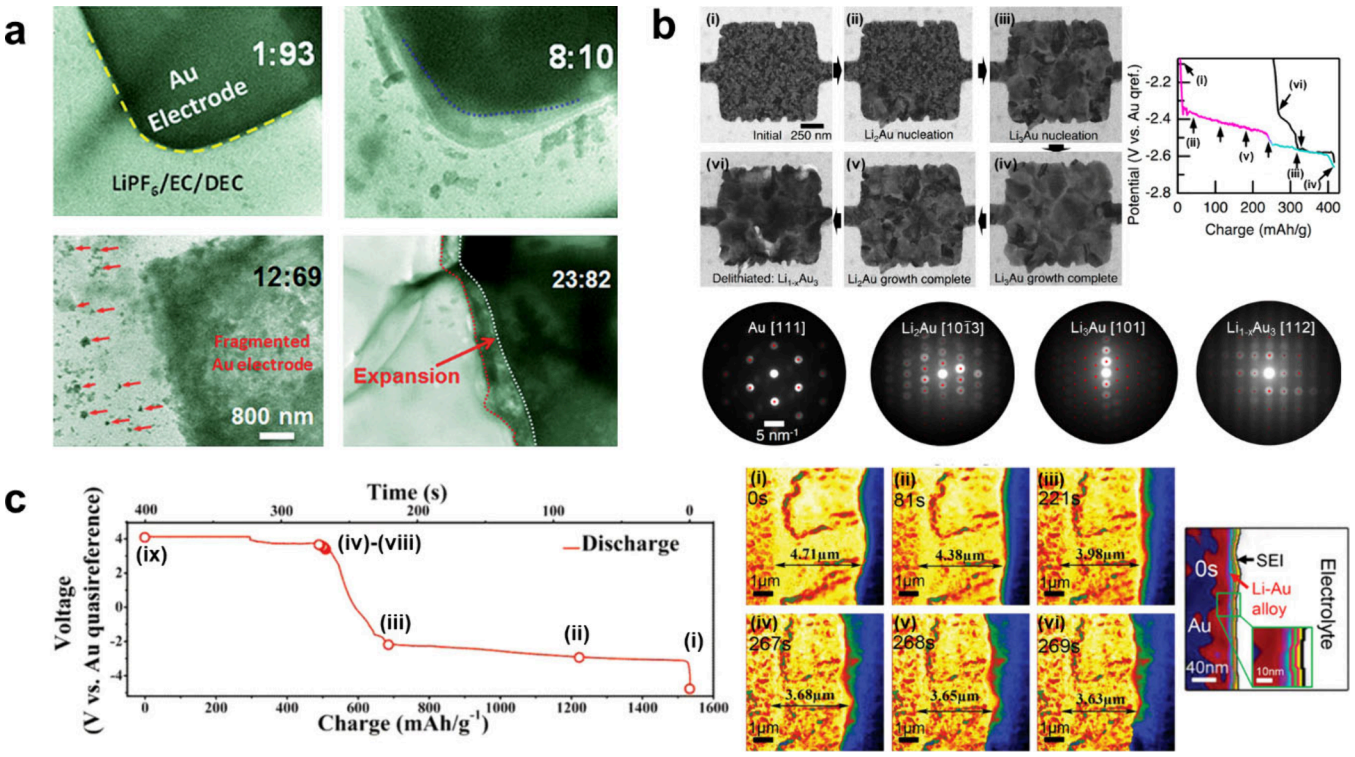

Figure 15. Lithium alloying reaction process of gold (Au) anodes revealed by *in situ* electrochemical liquid-phase TEM. (a) Gradual dissolution, explosive reactions, and local expansion/shrinkage of an Au electrode during lithiation. Reproduced with permission from ref 145. Copyright 2015 Royal Society of Chemistry. (b) Intermediate phase evolution during Li−Au alloying reactions. Reproduced with permission from ref 146. Copyright 2016 American Chemical Society. (c) SEI bilayer formation during lithiation of an Au anode. Reproduced with permission from ref 147. Copyright 2019 WILEY-VCH Verlag GmbH & Co. KGaA, Weinheim.

the second dissolution at the newly exposed surface. A drastic Li−Au alloying during lithiation resulted in an inhomogeneous reaction and peeling-off of lithiated Au particles, followed by vigorous bubble formation by the electrolyte decomposition observed in the subsequent steps. Additionally, lithiation and delithiation of the Au electrode resulted in observable expansion and shrinkage, accompanied by crack formation due to volume changes during these processes.

Another study demonstrated lithiation and phase propagation of Au and Al thin films using 1 M $LiPF_6$ in EC/DMC electrolyte, identifying intermediate phases through convergent beam electron diffraction (CBED) patterns (Figure 15b).[146] A nucleation/growth behavior was observed during lithiation of Au and Al films, with phase evolution progressing sequentially from nearby grains. In the early stages, the Au film underwent phase transformation into δ_1-Li_2Au, followed by Li_3Au. During the delithiation process, intermediate phases were absent, and the metastable α_1-$LiAu_3$ phase was identified as the final phase. On the other hand, lithiation of Al film led to the formation of polycrystalline β-LiAl through lateral spreading, with nonuniform spreading rates from nucleation points. This study suggests that, for the Al and Au films, lithiation initializes preferably at the outer corners, due to the lowest strain energy during lithiation. Furthermore, the unique phase evolution pathways were attributed to the low nucleation energy barrier at the grain boundaries.

In addition to exploring lithiation mechanisms, SEI formation on Au electrodes was also investigated by liquid-phase TEM.[96,147] The dendritic SEI formation before the Li deposition on the Au electrode was observed by Sacci et al., which was attributed to the decomposition of the EC solvent.[96] Hou et al. observed SEI formation, growth, and fracture on an Au electrode at an extremely high current density using commercial 1 M $LiPF_6$ in EC/DMC electrolyte (Figure 15c).[147] This work showed that an uneven and thick SEI is formed from reactions between the electrode and the electrolyte during the initial stages of lithiation. An inorganic inner SEI and an organic outer SEI were observed, exhibiting an inhomogeneous distribution and interface. During the charging process, SEI growth occurred as the electrolyte permeated through the porous SEI layers. It was proposed that the volume expansion of the Au electrode promoted the movement of small radicals, accelerating electrolyte decomposition, and consequently, SEI growth. The fracture of SEI film was caused by the substantial volume change during lithiation and delithiation. After cracks formed on the SEI surface, the rapid dissolution of the inorganic inner SEI layer occurred, contributing to the failure of the SEI films.

3.5. Metal Oxides

Metal oxides have been another research focus since 2000 due to their high theoretical capacities as conversion-type anode materials.[148] Numerous research efforts were put into this area to illustrate the lithiation mechanisms, along with morphological changes and their electrochemical reversibilities. Most metal oxide anodes undergo the following conversion reaction (eq 2) during lithiation

$$M_xO_y + 2yLi^+ + 2ye^- \rightarrow xM + yLi_2O \quad (2)$$

where M denotes metal element. Owing to their high atomic mass and electron beam tolerance, metal oxides are one of the most favorable materials for *in situ* TEM researchers. *In situ*

https://doi.org/10.1021/acs.chemrev.4c00507
Chem. Rev. XXXX, XXX, XXX−XXX

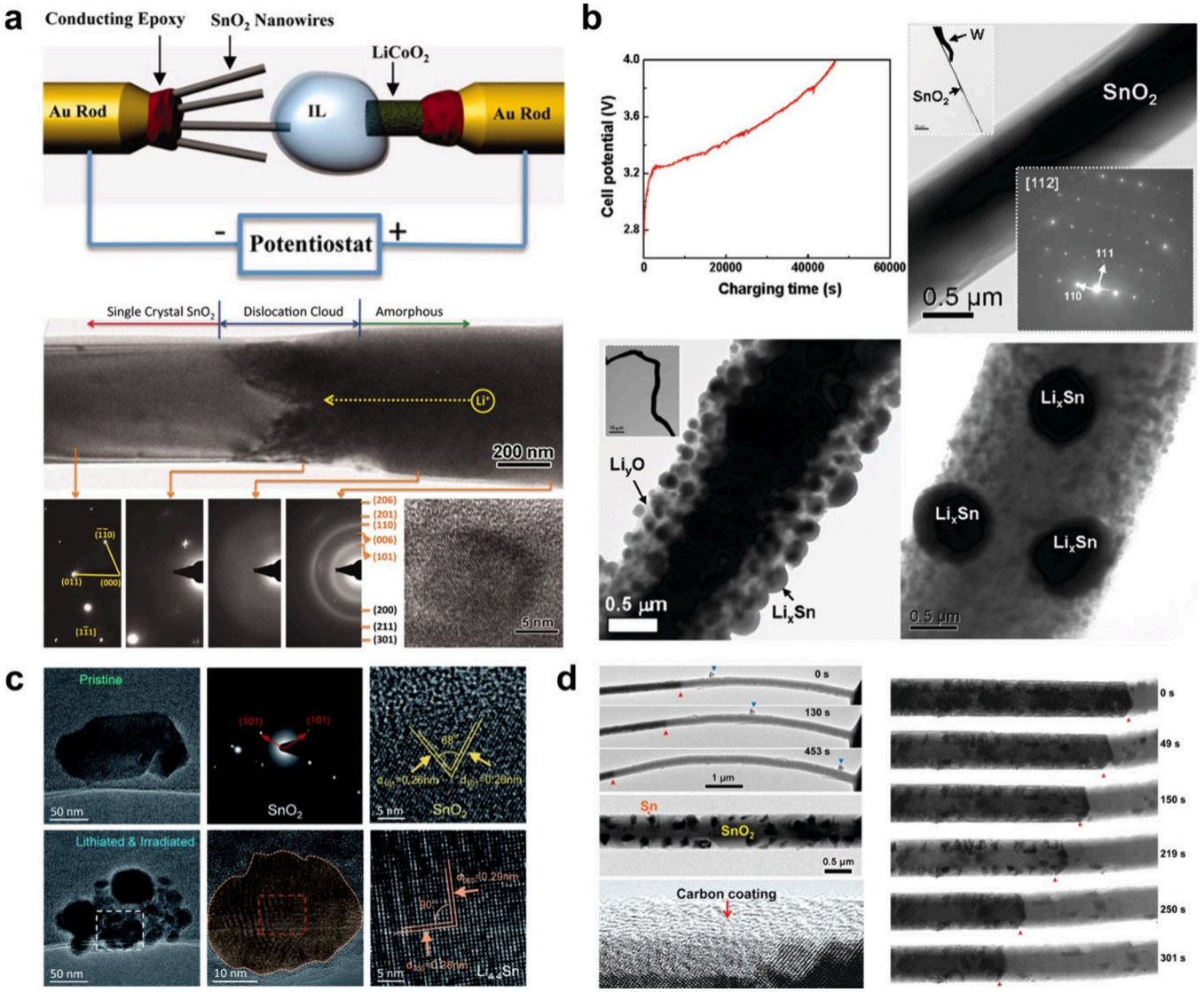

Figure 16. Lithiation processes of SnO_2 nanomaterials probed by open-cell *in situ* TEM. (a) A schematic of tip-based ionic-liquid open-cell configuration and structural changes observed in SnO_2 NW during lithiation. Reproduced with permission from ref 37. Copyright 2010 The American Association for the Advancement of Science. (b) Voltage curve and associated morphology changes during SnO_2 NW lithiation. Reproduced with permission from ref 151. Copyright 2011 American Chemical Society. (c) HRTEM and SAED analysis of SnO_2 NP before and after the 1st lithiation. Reproduced with permission from ref 152. Copyright 2020 Royal Society of Chemistry. (d) Microstructure evolution of SnO_2 NW with carbon coating. Reproduced with permission from ref 149. Copyright 2011 American Chemical Society.

TEM utilizing both open-cell and closed-cell configurations has greatly expanded the understanding of metal oxide anode materials down to the atomic level. Ever since the *in situ* TEM work on tin oxide (SnO_2) in 2010,[37] also known as the first *in situ* TEM work on lithium battery material, a major portion of *in situ* TEM efforts focused on SnO_2 material, with the rest focused on a vast range of metal oxides consisting of transition metal elements, i.e., Co, Ti, Fe, Ni, Mn, V, W, etc. As such, in this section we first summarize the research progress on SnO_2 using *in situ* TEM, then move onto studies of other transitional metal oxides.

3.5.1. Tin Oxides. Back in the 2010s, it was known that the microstructure of the electrode material directly impacts the electrochemical performance, where nanosized materials normally exhibit higher capacity and cyclability compared with microsized materials. However, direct evidence to demonstrate the transformation of nanomaterials during the electrochemical process was lacking in the research field. SnO_2 became the first example with its atomic structural change unveiled by tip-based ionic liquid *in situ* TEM by Huang et al., when SnO_2 was thoroughly studied using *in situ* TEM along with other advanced characterizations.[149,150]

3.5.1.1. Lithiation Mechanisms. Figure 16a shows the first nanodevice consisting of a SnO_2 nanowire, ionic liquid, and LCO cathode that can be controlled by a piezo-manipulator system. SnO_2 nanowire was moved to be in contact with ionic liquid, and the electrochemical stimuli was applied.[37] SnO_2 exhibited drastic volumetric changes both in axial direction and radial direction. Selected-area electron diffraction (SAED) at different locations around the reaction front demonstrated the presence of metallic Sn and Li_xSn alloys in the lithiated area, where the majority appeared amorphous.[37] More intriguingly, the lithiation in SnO_2 proceeds in a crystalline-to-amorphous manner that is mediated by the formation of a large amount of the dislocations at the crystalline/amorphous interface. Although the lithiated products are metallic Sn and Li_xSn,

https://doi.org/10.1021/acs.chemrev.4c00507
Chem. Rev. XXXX, XXX, XXX−XXX

the majority of the nanowire became amorphous. *In situ* TEM has provided unprecedented insights into SnO_2 material about its lithiation mechanism. Employing a similar setup, Wang et al. examined the lithiation process of SnO_2 nanowires while they were immersed in an ionic liquid (Figure 16b). The detailed analysis unraveled the nucleation of Li_xSn nanoparticles on the SnO_2 nanowire after lithiation, accompanying the formation of an amorphous matrix that was rich in Li_2O nanocrystallites.[151] This set of results further confirmed the lithiation process inside the SnO_2 nanowire, where solid-state amorphization appears as the triggering event.

In another tip-based solid-electrolyte *in situ* TEM work with Li metal as the lithium source, it was found that large $Li_{4.4}Sn$ crystals were formed upon a deep lithiation of the SnO_2 nanoparticles (Figure 16c). Nevertheless, such large crystal formation can be mitigated when the particle size was essentially reduced below 15 nm.[152] Drastic shape changes in SnO_2 nanowires or nanoparticles could pose potential concerns for practical electrode applications. Strategies such as surface coating were attempted as shown in Figure 16d. A 5 nm-thick carbon coating effectively suppressed the radial expansion of the SnO_2 nanowire during lithiation and no dislocation region was observed in the carbon-coated SnO_2 nanowire.[149] The mechanical strength of the carbon coating confined the lithiation direction and mitigated the undesired shape change of the SnO_2 nanowires.

The lithiation mechanism of SnO_2 within liquid electrolyte has the advantage of ensuring uniform lithiation into the nanostructure. Graphene liquid cells serve as ideal microreactors to observe atomistic insight of SnO_2 lithiation in liquid environments. Chang et al. sandwiched SnO_2 nanoparticles in a liquid electrolyte between the graphene TEM grids and utilized the electron beam to trigger the lithiation process, where Sn and Li_2O were identified as the lithiation product.[66] Subsequent high-resolution imaging captured the coalescence of two Sn particles at the lithiation stage, indicating the root of the shape change of the SnO_2 electrode after repeated charging and discharging. In another *in situ* TEM work performed in graphene liquid cells, the Sn−SnO_2 core−shell structure was used to investigate the lithiation process when interfacial stress is present. Sn core underwent lithiation and volume expansion, followed by lithium deficiency due to lithiation of the SnO_2 shell. Significant void formation was observed during the lithiation process.[153]

3.5.1.2. SEI Formation. Open cells were used to obtain atomistic insights into the lithiation mechanism, while closed cells provided the merits of observing SEI formation on SnO_2 anodes owing to the surrounding liquid electrolyte environment.[154] Cheong et al. observed the SEI growth on SnO_2 nanotubes utilizing graphene liquid cells (Figure 17a). HRTEM demonstrates that a relatively uniform SEI was formed at the beginning and then grew into a thicker SEI with an amorphous phase.[155] The observed SEI growth was attributed to the decomposition and redeposition of the electrolyte onto the nanotube surface, which eventually leads to a stable SEI layer after full lithiation. Figure 17b shows SEI growth on a SnO_2 nanotube with a TiO_2 coating on the surface. It was shown that a thick SEI was formed at the beginning and then became thinner as lithiation proceeded. The overall SEI thickness was merely ~12 nm. The opposite trend of SEI growth observed in these two studies demonstrated the importance of coating layers and how they help stabilize the SEI on SnO_2 nanotubes.[156] Another study

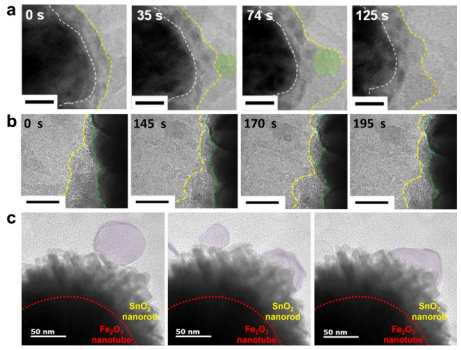

Figure 17. Lithiation processes of SnO_2 nanomaterials probed in graphene liquid cells. (a) HRTEM images showing the formation process of a thicker amorphous SEI layer on SnO_2 NP. Scale bars: 10 nm. Reproduced with permission from ref 155. Copyright 2016 Elsevier Ltd. (b) SEI growth on SnO_2 NT vs. time. Scale bars: 20 nm. Reproduced with permission from ref 156. Copyright 2017 Elsevier Ltd. (c) SEI layer observation on SnO_2 NRs. Reproduced with permission from ref 157. Copyright 2017 The Authors.

with graphene liquid cells used SnO_2 nanorod on Fe_2O_3 nanotubes and observed the nonuniform SEI growth on the SnO_2 nanorod (Figure 17c). The observed SEI was attributed to the high surface area of the nanorods in contact with the liquid electrolyte.[157]

Although the graphene liquid cell provided exceptional spatial resolution over SiN_x liquid cell studies, the intrinsic limitation of lacking electrochemical stimuli has weakened the conclusions, especially regarding the SEI formation. Normally a SEI forms with the electrolyte decomposition when the local electrochemical potential is out of the electrochemical stability window of the electrolyte. However, the electrolyte decomposition observed in the graphene liquid cells is likely caused by electron beam irradiation, which acts more as a source of damage than as a stimulus. Nevertheless, the way graphene liquid cell works for liquid-phase TEM by forming liquid pockets has provided invaluable insight for the next-generation atomistic-resolution liquid cell development for electrochemical processes.

3.5.2. Transition Metal Oxides. Due to their high theoretical capacities, transition metal oxides (TMO) have been extensively studied as potential anode materials using *in situ* TEM. Common TMO anodes contain a variety of species such as Co, Ti, Fe, Ni, Mn, V, W, etc., most of which follow conversion reactions during lithiation processes. Nevertheless, due to the different crystal structures, atomic radii, lithium diffusivities, and chemical properties of these oxide anodes, they all exhibit distinct lithiation behaviors and electrochemical performance. Different particle morphologies and sizes are another important parameter to determine the variations among these TMOs. These electrochemical properties require in-depth investigations so that a relationship between electrochemical performance and their intrinsic properties can be established for the optimization of TMO anodes.

In situ TEM using open-cell configuration provides the advantage of high spatial resolution, where the majority of them utilized solid-electrolyte open-cell sample setup owing to the ease of using lithium metal as the anode and its surface oxide as the solid electrolyte. We will summarize the exemplary results from mostly single-transition-metal oxides in the order of ascending atomic numbers and propose the optimal

https://doi.org/10.1021/acs.chemrev.4c00507
Chem. Rev. XXXX, XXX, XXX−XXX

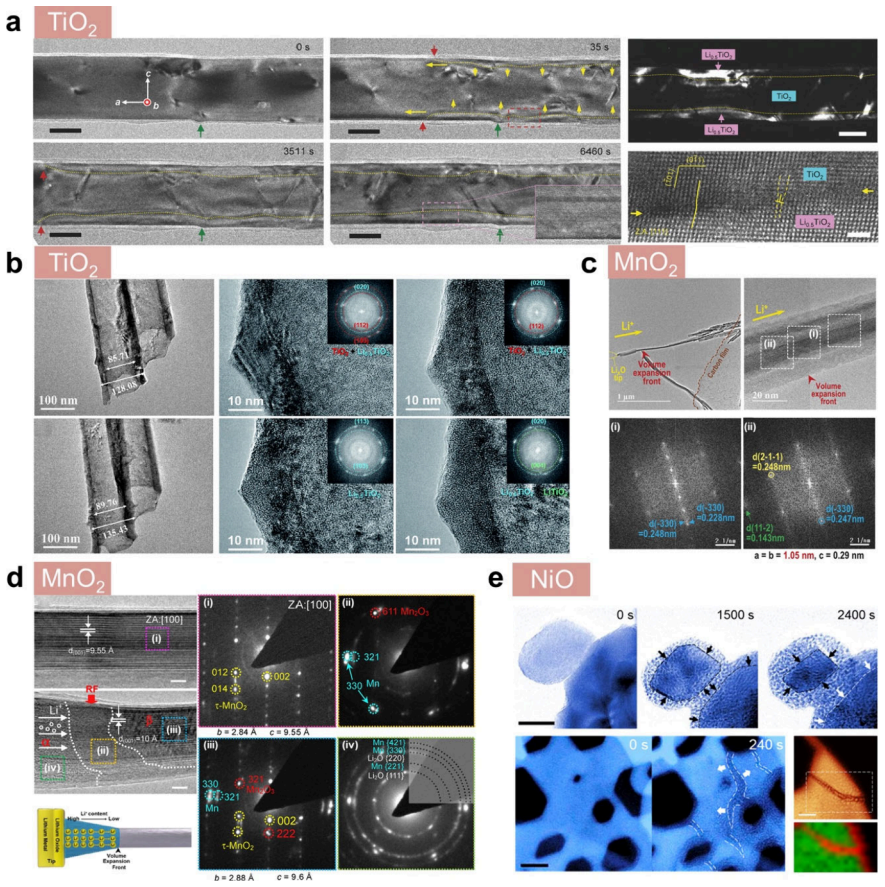

Figure 18. Lithiation processes of TMO nanomaterials via open-cell *in situ* TEM configurations. (a) Nanostructure evolution of TiO_2 NW during lithiation. Scale bars for TEM images and HRTEM image: 50 and 2 nm, respectively. Reproduced with permission from ref 159. Copyright 2017 WILEY-VCH Verlag GmbH & Co. KGaA, Weinheim. (b) Low-magnification morphological change along with HRTEM analysis of N-doped TiO_2 NTs. Reproduced with permission from ref 160. Copyright 2017 Royal Society of Chemistry. (c) Low-magnification TEM images of a K-doped α-MnO_2 NW during lithiation. FFTs show the presence of lattice expansion. Reproduced with permission from ref 162. Copyright 2017 WILEY-VCH Verlag GmbH & Co. KGaA, Weinheim. (d) HRTEM and SAED analysis of τ-MnO_2 NR during lithiation. Lattice expansion and metallic Mn formation were observed. Scale bars: 10 nm. Reproduced with permission from ref 163. Copyright 2019, Elsevier Ltd. (e) Morphological changes of NiO NPs showing shrinking-core mode and finger mode during lithiation. Scale bars: 20 nm. Reproduced with permission from ref 164. Copyright 2015 American Chemical Society.

conditions required for the high capacity and long cyclability of such anodes.

Titanium oxides are potential lithium anode materials due to their ability to store lithium ions and form a stable lithiated structure, which has been reported to undergo a two-phase lithiation process.[158] Figure 18a and 18b demonstrate the lithiation mechanism of anatase TiO_2, where the impact of particle sizes and electronic conductivity are emphasized. Figure 18a shows the lithation process of a single-crystal TiO_2 nanowire, where an interface between anatase TiO_2 and orthorhombic $Li_{0.5}TiO_2$ was clearly observed upon gradual lithiation.[159] The interface was shown in the HRTEM images where 5−10 atomic layers were found between two phases. Due to the low lithium kinetics inside the $Li_{0.5}TiO_2$ phase, lithiation proceeds fairly slowly. Intriguingly, when using polycrystalline TiO_2 nanoparticles with sizes below 25 nm, no interface was observed between TiO_2 and $Li_{0.5}TiO_2$, which underwent a solid-solution mediated lithiation process instead. The possible reason is that the nanosized polycrystalline TiO_2 can provide short lithium diffusion pathways and facilitate the fast phase change to the lithiated phase. In another study by Zhang et al., an N-doped TiO_2 nanotube was used for *in situ* TEM for the sake of improving its electronic conductivity (Figure 18b). Detailed HRTEM analysis unveiled a facile phase transformation from anatase TiO_2 to orthorhombic $Li_{0.5}TiO_2$ and then $Li_{0.5}TiO_2$ to tetragonal $LiTiO_2$. The facile lithiation and improved electrochemical performance were attributed to the enhanced electronic conductivity of the anatase TiO_2 nanotubes.[160]

Magnesium oxide (MnO_2) is one of the promising electrode materials for lithium batteries as it can serve either as a cathode through the lithium insertion mechanism or an anode through the conversion mechanism.[161] However, the conversion mechanism in the case as an anode material was not crystal clear in the field. *In situ* TEM employing solid-electrolyte open-cell configuration was used to study the lithiation mechanism of α-MnO_2 (Figure 18c). Lee et al. captured the fast lithium diffusion into K-doped α-MnO_2 due to its unique one-dimension lithium pathway. HRTEM and diffraction analysis identified the formation of $MnO+Li_2O$ as the intermediate phase, and metallic $Mn+Li_2O$ as the final lithiated products, with a crystal orientation relationship between the MnO_2 reactant and the MnO/Li_2O products.[162] Another work focused on the lithiation mechanism of todorokite-type manganese oxide (τ-MnO_2) using open-cell configuration *in situ* TEM (Figure 18d). τ-MnO_2 has intrinsically larger tunnels

https://doi.org/10.1021/acs.chemrev.4c00507
Chem. Rev. XXXX, XXX, XXX−XXX

for enhanced lithium transportation but the lithiation mechanism was not well understood. By using τ-MnO_2 nanorods, Cai et al. captured the intermediate phase as Mn_2O_3+Li_2O during lithiation. A rapid lithium migration was also observed on the surface of the τ-MnO_2 nanorods. Metallic Mn and Li_2O were observed toward the end of lithiation.[163] Intriguingly, upon delithiation, Mn was only able to transform back to the Mn_2O_3 phase instead of τ-MnO_2, indicating a lower formation energy of Mn_2O_3 compared to τ-MnO_2.

On another note, the NiO anode material suffers from limited rate capability. The underlying mechanism was uncovered using open-cell *in situ* TEM (Figure 18e). He et al. captured that lithiation of NiO follows a shrinking-core mode in the early stage and then follows a finger-like nucleation mode when lithiation gets deeper into the nanoparticles. The fairly fast lithiation was observed in the shrinking-core stage, while deeper lithiation took a long time for incubation to form finger-like nucleation areas inside the nanoparticles, after the particle interiors became gradually fully lithiated.[164] The finding is directly related to the slow kinetics observed in the battery rate capability testing. Accelerating the incubation inside the particle turns out be the key to enhancing the rate performance of NiO material.

Magnetite Fe_3O_4 is an anode candidate for lithium battery due to its inexpensive and nontoxic nature, which in the meantime can deliver a theoretical capacity of 926 mAh g^{-1}. He et al. utilized open-cell configuration to study the lithiation mechanism of Fe_3O_4 inside TEM (Figure 19a). Metallic Fe and Li_2O were identified as the final lithiation products as common metal oxide anodes. Nevertheless, a coexistence of three phases, namely Fe_3O_4, $Li_xFe_3O_4$, and Fe+Li_2O, was captured during lithiation in bright-field STEM images. Based on the phase contrast, a clear phase transformation process was demonstrated. The $Li_xFe_3O_4$ phase nucleated from the edge of the nanoparticle, while the Fe+Li_2O phase appeared before the full lithiation of the Fe_3O_4 phase, rendering the presence of three phases on the same particle.[165] By comparing the propagation speed of such phases, it was found that the intercalation step into the $Li_xFe_3O_4$ phase is much faster than the conversion step into Fe+Li_2O, stressing how the reaction kinetics can affect the lithiation pathway at the single-particle level.

Cobalt oxides are another popular metal oxide anode materials besides SnO_2, as CoO was one of the earliest metal oxides investigated as a conversion-type lithium-ion battery anode.[148] *In situ* TEM was extensively applied to study the lithiation mechanism of cobalt oxides with various stoichiometries and their analogues.[168−171] Figure 19b shows the lithiation process of Co_3O_4 nanoparticles that were dispersed on a graphene sheet and then loaded into the open-cell setup. Many *in situ* studies on metal oxides have employed carbon-film-based sample configuration,[172−175] which is similar to those loading sample particles on TEM half grids as the working electrode.[166] In this work, Co_3O_4 particles were lithiated to form metallic Co particles embedded within a Li_2O matrix. And the formation of CoO instead of Co_3O_4 was unveiled during the subsequent delithiation and lithiation, indicating that the capacity loss of the first cycle comes from the irreversible formation of the Co_3O_4 phase. Zinc oxide (ZnO) has also been considered as a promising anode material due to its high theoretical capacity of 978 mAh g^{-1} and environmental compatibility. Nevertheless, bulk ZnO anodes suffer from sluggish kinetics in stark contrast to their nanosized

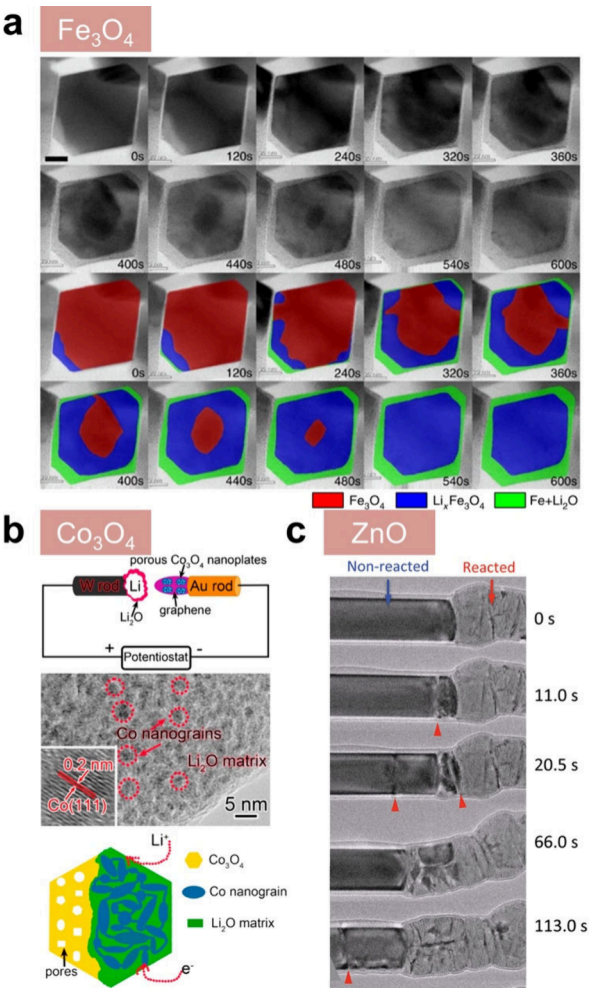

Figure 19. Lithiation process of TMO nanomaterials via open-cell *in situ* TEM configuration. (a) *In situ* observation of two-phase lithiation in Fe_3O_4 nanocrystal. Scale bar: 20 nm. Reproduced with permission from ref 165. Copyright 2016 The Authors. (b) Nanostructural changes in Co_3O_4 nanoplates during lithiation and the corresponding schematic. Reproduced with permission from ref 166. Copyright 2014 Elsevier Ltd. (c) Crack-driven lithiation process in ZnO NWs by HRTEM images. Reproduced with permission from ref 167. Copyright 2011 American Chemical Society.

analogue. A good understanding of their lithiation mechanism was needed to address such size-dependent performance. Figure 19c shows the lithiation process of single-crystal ZnO nanowires using open-cell *in situ* TEM. Similar to the observation of SnO_2, solid-state amorphization was observed during the lithiation of ZnO nanowires.[167] However, nanocracks with a length of about 70 nm were observed ahead of the lithiation front and were proposed to be precursors of electrochemically driven solid-state amorphization, calling for engineering efforts to reduce the particle sizes for improved kinetics.

More research efforts on TMO anodes include MoO_3 and WO_3, and RuO_2 materials.[176−181] Figure 20a demonstrates the lithiation and delithiation mechanisms of MoO_3 nanobelt. Upon lithiation, metallic Mo and Li_2O were formed as the lithiated products. During delithiation, crystalline $Li_{1.66}Mo_{0.66}O_2$ was first formed, after which amorphous Li_2MoO_3 was formed as the final delithiated product.[176] Despite the irreversible phase conversion during the first cycle,

https://doi.org/10.1021/acs.chemrev.4c00507
Chem. Rev. XXXX, XXX, XXX−XXX

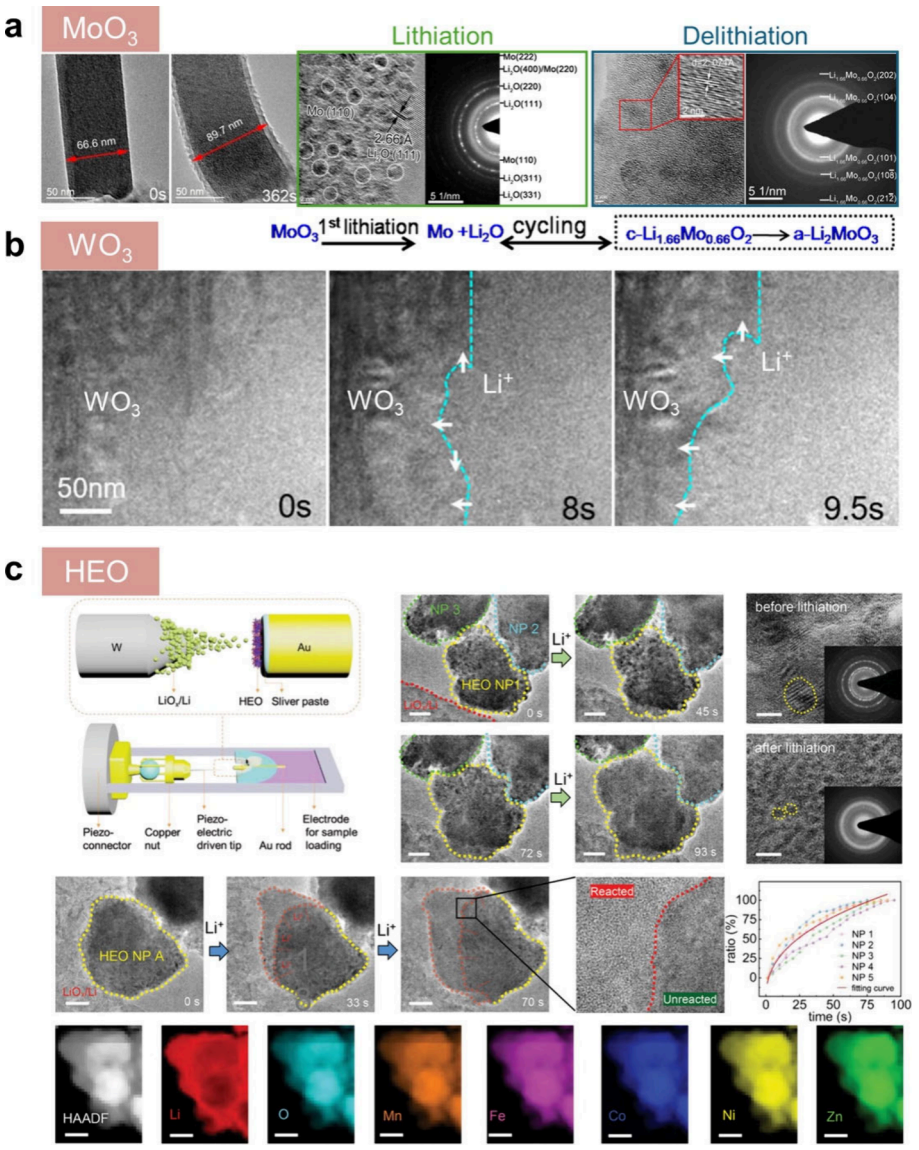

Figure 20. Lithiation process of TMO nanomaterials via open-cell *in situ* TEM configuration. (a) Morphological and structural changes of MoO_3 during lithiation and delithiation. Reproduced with permission from ref 176. Copyright 2016 American Chemical Society. (b) Reaction front migration during WO_3 lithiation. Reproduced with permission from ref 177. Copyright 2023 American Chemical Society. (c) Nanostructural evolution of HEO NPs upon lithiation. EDS mapping shows the presence of various metal elements. Scale bars: 50 nm (except for those for magnified HRTEM images: 5 nm). Reproduced with permission from ref 45. Copyright 2023 Wiley-VCH GmbH.

the subsequent phase transformations between Mo and Li_2MoO_3 appear reversible. Figure 20b shows the lithiation process of WO_3 film using open-cell *in situ* TEM. Planar defects were observed at the reaction front during lithiation.[177] DFT calculation indicates that such defects tremendously increased the migration barrier for lithium ions and thereby led to nonuniform lithiation speed and uneven reaction front, emphasizing the importance of eliminating nanodefects for improved lithium-ion transportation.

As an emerging trending topic, high-entropy alloy synthesis obtained fast advancement recently. High-entropy metal oxides (HEOs) have also caught research attention due to the possibility of combining the merits of different metal oxides as anode materials. Figure 20c demonstrates the lithiation mechanism observed in an HEO that consists of Co, Ni, Mn, Zn, and Fe elements using open-cell *in situ* TEM. As expected, single-phase HEO particles transformed into metallic particles embedded in a Li_2O-rich amorphous matrix at the end of the first lithiation.[45] Surprisingly, the polyphase metallic species could be recovered to the original single-phase HEO after delithiation. Repeated cycling was achieved due to the reversible reaction between single-phase HEO and polyphase metallic products. Note that other metal species mainly underwent conversion reactions, while Zn species went through both conversion and alloying reactions, providing extra capacity. Such efforts call for more attention to HEOs that could potentially be used as practical anode materials.

In a word, metal oxides are one of the most popular anode materials investigated besides graphite, Si, and Li anodes. Their high theoretical capacities undoubtedly attract significant research attention. Nanosized metal oxides were widely used to avoid the shortcomings of low electronic conductivities. However, severe volume changes still pose challenges to their cyclability. Additionally, the use of transition metal brings extra concerns regarding the gravimetric energy density and cost.

https://doi.org/10.1021/acs.chemrev.4c00507
Chem. Rev. XXXX, XXX, XXX−XXX

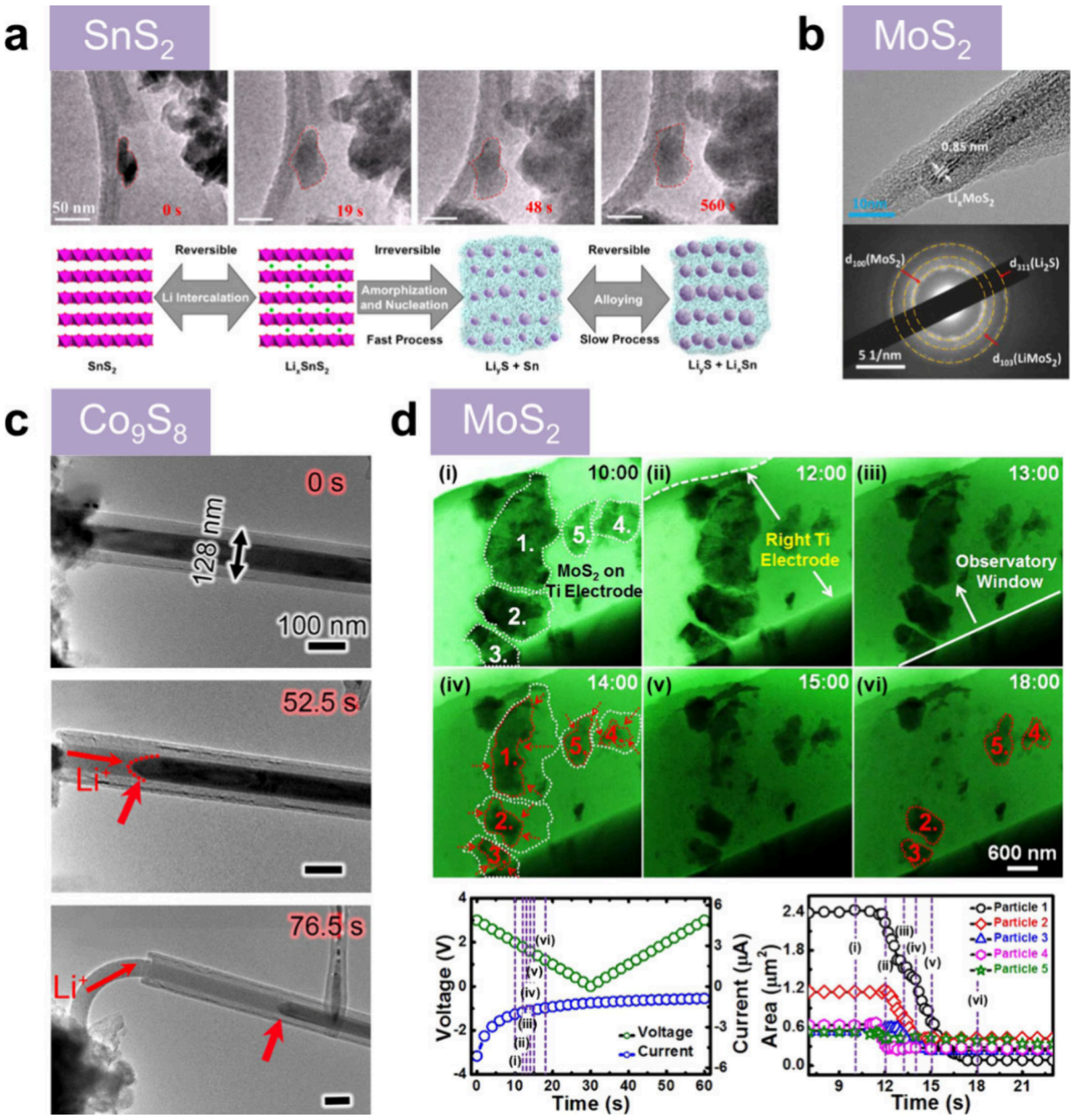

Figure 21. Lithiation process of metal chalcogenides via *in situ* TEM using (a–c) open-cell and (d) closed-cell configurations. (a) Nanostructural evolution of SnS_2 during lithiation. Reproduced with permission from ref 186. Copyright 2017 American Chemical Society. (b) HRTEM and SAED showing the structural change of MoS_2 upon lithiation. Reproduced with permission from ref 187. Copyright 2020 Elsevier Ltd. (c) Morphological changes of Co_9S_8 inside CNT during lithiation. Reproduced with permission from ref 189. Copyright 2013 American Chemical Society. (d) Low-magnification TEM images of microstructures of MoS_2 nanosheets inside SiN_x liquid cell. Reproduced with permission from ref 190. Copyright 2015 American Chemical Society.

Future research ought to focus on improving the cyclability of metal oxides while harvesting their high theoretical capacity.

3.6. Metal Chalcogenides

Owing to their unique electronic and catalytic properties, metal chalcogenides (MCs) have drawn tremendous attention and exhibited promises for next-generation electronics, electrochemical energy storage, chemical sensing devices, etc.[182,183] Regarding the battery applications, MCs show high theoretical capacity due to the combination of intercalation, conversion, and alloying reactions which in total yield extra capacity compared with the state-of-the-art anode materials.[183,184] Common MCs such as MoS_2, $MoSe_2$, VS_2, and SnS_2 have been widely studied as battery anodes or host materials.[185] However, due to the intrinsically low electronic conductivity and low cyclability, a better understanding of their lithiation process was needed for the structure optimization of MCs, where *in situ* TEM comes in play. Some of the *in situ* TEM works on MCs are summarized below.

Yin et al. utilized a tip-based open-cell configuration to study the lithiation mechanism of SnS_2 as shown in Figure 21a. Detailed analysis captured the lithiation process as follows: 1) lithium intercalation into the SnS_2 layers to form the Li_xSnS_2 phase; 2) with further lithiation, Li_xSnS_2 transitions to an amorphous state with metallic Sn nucleation inside a Li_2S-rich amorphous matrix; 3) subsequently, lithium alloys with Sn to form Li_xSn in the presence of Li_2S.[186] It was proposed that the

https://doi.org/10.1021/acs.chemrev.4c00507
Chem. Rev. XXXX, XXX, XXX−XXX

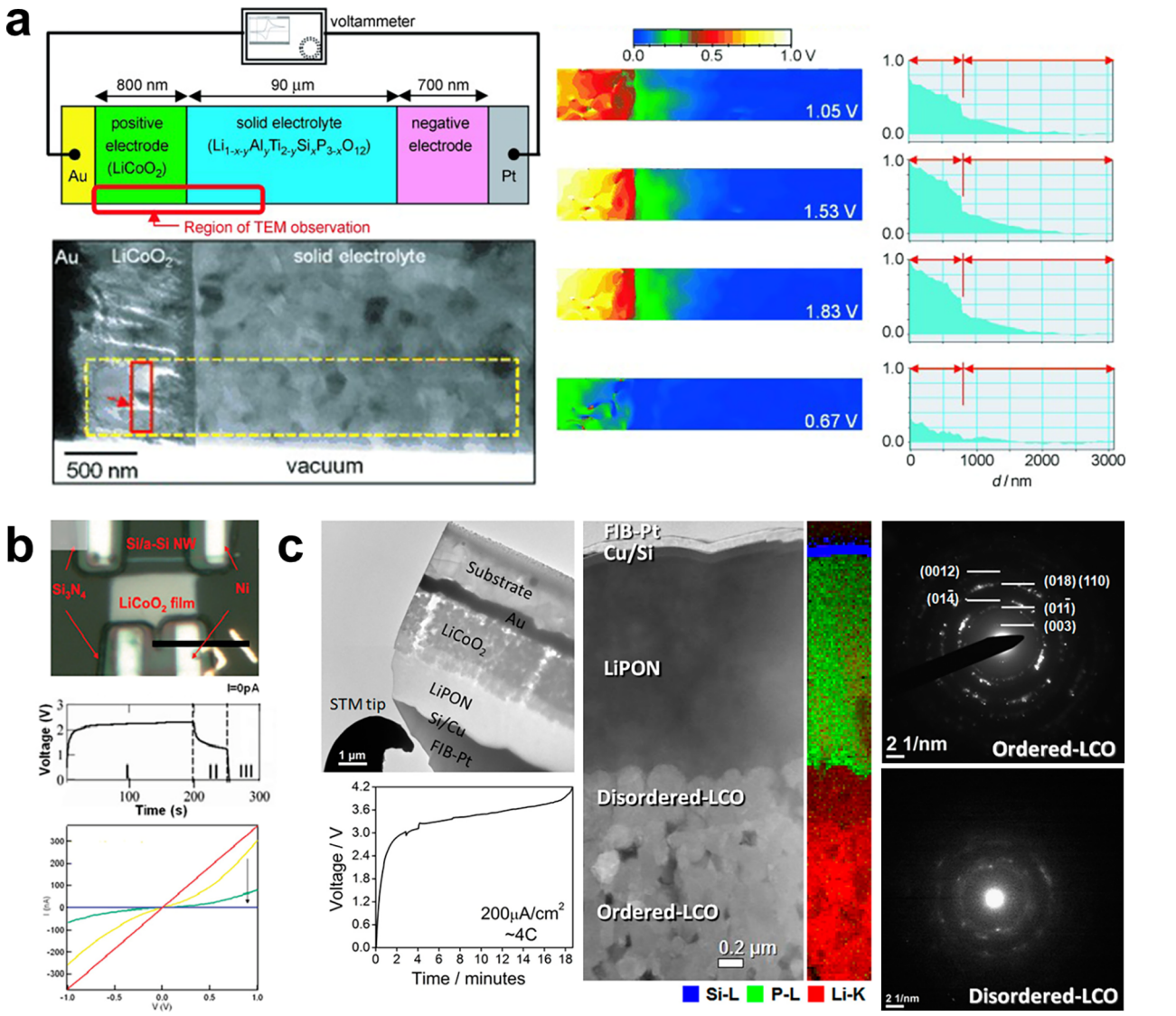

Figure 22. Open-cell *in situ* TEM studies on LCO cathodes and associated interfaces. (a) A schematic of open-cell configuration and electrical potential mapping of an LCO-based microbattery by electron holography. Reproduced with permission from ref 38. Copyright 2010 WILEY-VCH Verlag GmbH & Co. KGaA, Weinheim. (b) Electrical tests on Si-LCO microbattery in an open-cell design. Scale bar: 10 μm. Reproduced with permission from ref 39. Copyright 2010 American Chemical Society. (c) Cross-sectional examination on an LCO-based nanobattery by HRTEM, EELS mapping, and SAED. Reproduced with permission from ref 191. Copyright 2016 American Chemical Society.

alloying step was the limiting step due to the low electronic conductivity of the Li_2S matrix. Most of the capacity loss occurred during the conversion reaction to form Li_2S, because Li_2S is a rather stable component in an electrochemical system. Another work focused on the lithiation process of MoS_2, which exhibits faster lithium kinetics due to its larger interlayer spacing (Figure 21b). *In situ* TEM was able to capture a multiple-step intercalation-conversion reaction as lithiation proceeds. The final lithiated products turned out to be Mo and Li_2S, mixed with the Li_xMoS_2 phase.[187] Large volume expansion was observed during lithiation. Su et al. investigated the lithiation process of Co_9S_8 material in the presence of a carbon nanotube encapsulation. Figure 21c illustrates the confined lithiation inside a carbon nanotube, where axial elongation is effectively suppressed and radial expansion is measured to be ~32.4%. The excellent electronic properties of carbon nanotubes facilitated facile lithiation in Co_9S_8. In particular, the lithiated Co_9S_8 nanowire showed severe axial elongation and even extruded through the wall of the open carbon nanotube, stressing the essence of host materials in mitigating large volume expansion while providing sufficient electronic conductivity.[188,189]

The SiN_x-based liquid cell has also been employed to study the lithiation process of MoS_2 nanosheets inside a liquid electrolyte (Figure 21d). MoS_2 decomposition into nanoparticles was captured in the early stage of lithiation, followed by volume shrinkage of individual particles. Such phenomena stand in direct contrast to the findings of the open-cell study, where volume expansion was observed.[187] It was proposed that due to the presence of the liquid electrolyte, severe formation of lithium polysulfides and their dissolution into the electrolyte led to the loss of MoS_2 material.[190] Such a process is likely to occur within the liquid electrolyte especially when electron beam serves as extra stimuli besides electrical current.

In summary, MCs demonstrate their great potential as battery anode materials while their intrinsically low electronic

https://doi.org/10.1021/acs.chemrev.4c00507
Chem. Rev. XXXX, XXX, XXX−XXX

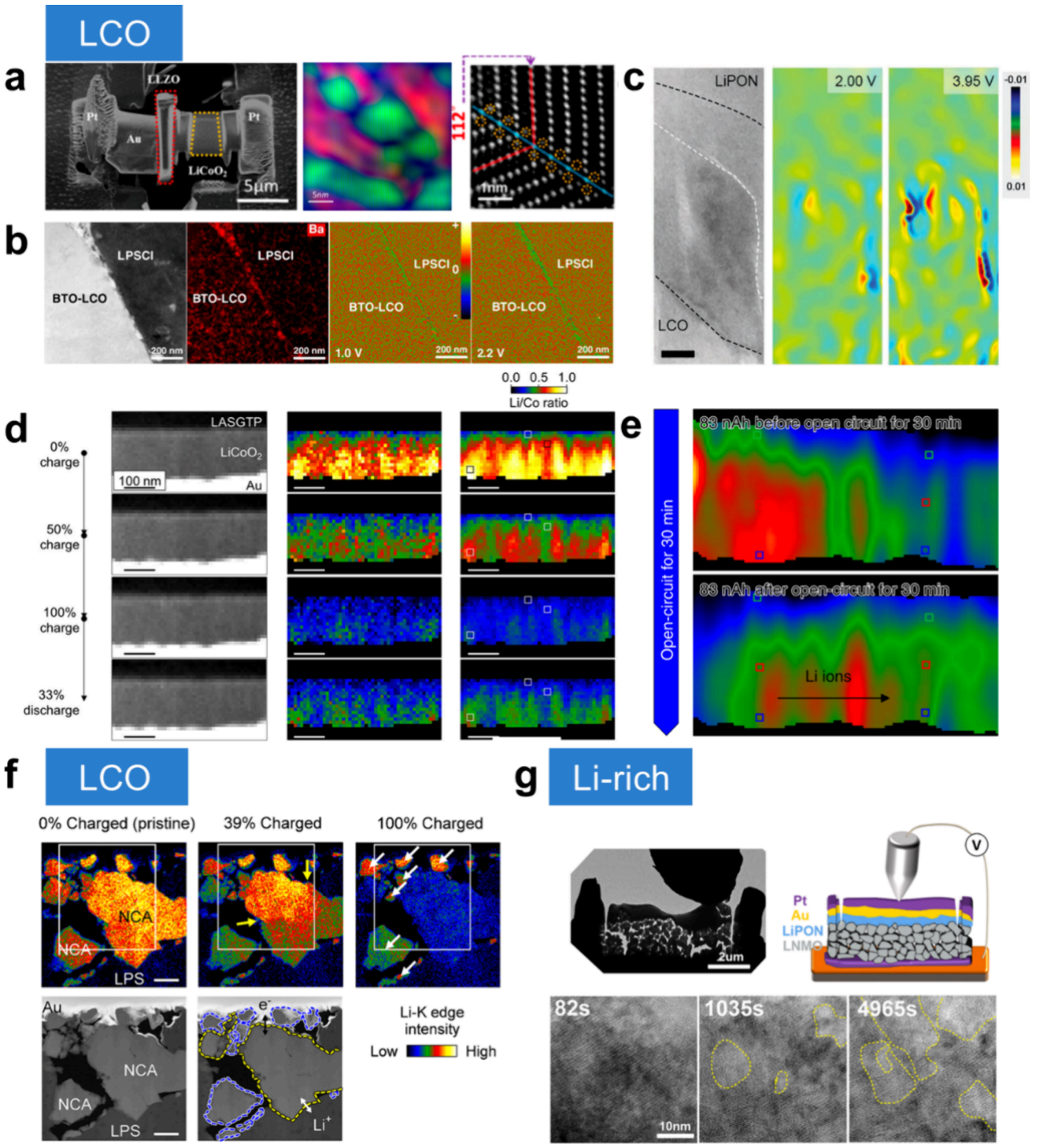

Figure 23. Lithium transport, interface formation, and structural change within LTMOs during cycling. (a) Twin boundary formation inside LCO nanocrystallites at discharged state. Reproduced with permission from ref 192. Copyright 2017 American Chemical Society. (b) Facile lithium transport across the interface between BTO-coated LCO and LPSCl during charging. Reproduced with permission from ref 193. Copyright 2020 The Authors. (c) Lithium accumulation along the LCO/LiPON interface observed by electron holography. Scale bar: 100 nm. Reproduced with permission from ref 194. Copyright 2021 Wiley-VCH GmbH. (d) Lithium transport properties between LCO grains and at the LCO/LASGTP interface investigated by enhanced EELS mapping via NMF analysis. Scale bars: 100 nm. Reproduced with permission from ref 195. Copyright 2018 American Chemical Society. (e) Lithium redistribution at open-circuit condition probed by high-resolution EELS. Reproduced with permission from ref 196. Copyright 2020 The Authors. (f) Lithium diffusion pathways in NCA cathode monitored by *in situ* STEM-EELS mapping. Scale bars: 500 nm. Reproduced with permission from ref 197. Copyright 2020 American Chemical Society. (g) Pore formation inside Li-rich cathode during charging. Reproduced with permission from ref 198. Copyright 2022 American Chemical Society.

conductivity and the formation of Li_2S solid/polysulfides remain as obstacles for future development. Conductive host materials and the use of solid electrolytes call for more research efforts to address the existing issues for MCs.

https://doi.org/10.1021/acs.chemrev.4c00507
Chem. Rev. XXXX, XXX, XXX−XXX

4. *IN SITU* TEM STUDY OF CATHODE MATERIALS FOR LITHIUM BATTERIES

Early development in the lithium battery field focused on expanding cathode chemistry to obtain materials with higher capacity, better cyclability, and good thermal and structural stability. Lithium transition metal oxides (LTMOs) are one of the major families in the lithium cathode category, including well-known materials such as lithium cobalt oxide (LCO), lithium manganese oxide (LMO), lithium nickel cobalt manganese oxide (NCM), lithium nickel manganese oxide (LNMO), and lithium nickel cobalt aluminum oxide (NCA). Additionally, lithium iron phosphate (LFP), though belonging to the phosphate family, is widely used due to its exceptional cyclability and thermal stability.

Characterizations such as X-ray diffraction (XRD) have been employed to determine the crystal structures of these LTMO cathodes, revealing the lithium diffusion pathways within different structures. For instance, layered structures provide two-dimensional diffusion pathways, while spinel structures offer three-dimensional pathways, and olivine structures allow for one-dimensional lithium conduction. Lithium ions intercalate through these cathodes during battery operation without significantly altering their crystal structures. The distinct crystal structures and compositions result in sharply varying electrochemical properties among these intercalation cathodes.

Despite these differences, most LTMO cathodes experience similar degradation mechanisms during repeated cycling, such as crystal structural changes, interphase formation, and mechanical failure. A thorough understanding of these degradation events during operation is crucial for engineering the next-generation cathode materials.

Beyond intercalation cathodes, there are also promising cathode candidates from other chemistries, such as fluoride cathodes, sulfide cathodes, lithium−sulfur (Li−S), lithium−oxygen (Li−O_2), and lithium−carbon dioxide (Li−CO_2). Many of these cathodes fall under the category of conversion-type materials, which involve different electrochemical reaction mechanisms compared to traditional intercalation cathodes. Instead of retaining their crystal structures during lithiation/delithiation, conversion cathodes undergo drastic structural changes, often along with irreversible processes that lead to capacity loss. However, due to the high theoretical capacities of conversion cathodes, countless research efforts have been devoted to this field. *In situ* TEM is one of the most useful tools to study the lithiation mechanism and structural changes at the nanoscale, providing insights that can be directly applied to cathode structural modifications or cell optimization. Below we summarize some major progress on *in situ* TEM that probed on both intercalation and conversion cathodes in the past decades.

4.1. Lithium Transition Metal Oxides

Since structural transformations in LTMO cathodes are relatively subtle during cycling, a high-resolution imaging capability is commonly needed to capture the corresponding changes, where the conventional liquid-phase TEM setup falls short of spatial resolution. Therefore, the majority of *in situ* TEM studies on LTMO cathodes employed open-cell configurations, including both tip-based and chip-based setups. Due to the micrometer size of common LTMO cathode particles, cathode lamella or thin films are more suitable for *in situ* TEM works where the focused ion beam is frequently used for sample preparation. For better compatibility with cathode lamella and thin films, solid electrolytes instead of ionic liquids are preferred for this type of study.

Figure 22a shows one of the first open-cell *in situ* TEM studies on an LCO cathode and its interface with a $Li_{1-x-y}Al_yTi_{2-y}Si_xP_{3-x}O_{12}$ solid electrolyte using a sample setup similar to the chip-based configuration. This planar all-solid-state battery allows for TEM observation at the sampling region indicated by the red box, which was thinned down to ∼60 nm in thickness by the focused ion beam. Current collectors on two ends of the battery are used for electrical control. Electron holography was employed to demonstrate the electrical potential change across the battery lamella during charging and discharging.[38] A gradual decrease of electrical potential was observed in the LCO cathode toward the electrolyte direction. However, a drastic potential drop was captured between LCO and solid electrolyte, indicating high interfacial impedance at the cathode/electrolyte interface.[38] This is the first visualization of the interfacial resistance inside a solid-state battery via electron microscopy. Figure 22b demonstrates a chip-based open-cell design where LCO serves as the cathode, lithium phosphorus oxynitride (LiPON) as the solid electrolyte, and a Si nanowire as the anode. Such sample configuration was able to charge and discharge inside the microscope and unveil a diminished electrode reversibility due to the decreased electronic conductivity of the electrode.[39] However, due to the planar layout of the deposited samples, this setup was not able to perform high-resolution imaging.

Another noteworthy work utilized a solid-state battery sample lamella and a piezo-controlled tip for electrical control (Figure 22c). The sample also consists of an LCO cathode, an LiPON electrolyte, and an Si anode, while this lamella was thinned down to below 100 nm in thickness for electron transparency. Precise potential control was achieved in this setup. Electron diffraction uncovered a disordering of LCO cathode at the interface between LiPON and bulk LCO for the first time, which was composed of CoO and lithium oxide species.[191] EELS mapping afterward suggests a lithium accumulation at the LCO/LiPON interface, which might be the cause of forming lithium oxide species and low-valence Co species, and be the source of a high interfacial impedance. This open-cell setup is similar to the sample configuration in chip-based open cells, except for the electrical stimuli via a piezo-controlled probe. Such setup appears easier to fabricate while it lacks sufficient structural stability due to the use of the tip, compared to the chip-based open cells. Regardless, these three works have directly visualized the interfacial phenomena between cathode and electrolyte and inspired the chip-based sample design in the later stage for *in situ* TEM studies.[51,52]

Figure 23a shows a chip-based open cell that consists of an LCO cathode and a lithium lanthanum zirconium oxide (LLZO) solid electrolyte. Geographical phase analysis clearly labeled the orientation and size of individual grains of the LCO cathode.[192] By using aberration-corrected STEM imaging, the presence of twin boundaries and antiphase domain boundaries inside the LCO layer was found after delithiation, which might be a source of impedance inside the cathode. Another work using LCO and an argyrodite Li_6PS_5Cl (LPSCl) solid electrolyte demonstrated a lithium accumulation at the cathode/electrolyte interface. However, after coating the LCO cathode with a thin layer of $BaTiO_3$ (BTO), the interface exhibits much-reduced charge accumulation (Figure 23b). It was proposed that this dielectric BTO layer can

https://doi.org/10.1021/acs.chemrev.4c00507
Chem. Rev. XXXX, XXX, XXX−XXX

effectively mediate the lithium diffusion at the interface, thereby reducing the charge nonuniformity and interfacial impedance.[193] The direct evidence of charge redistribution suggests the essence of the dielectric oxide coating layer, which has been widely applied in solid-state batteries afterward. Figure 23c illustrates the electron holography mapping of a nanobattery made of LCO cathode and LiPON solid electrolyte. Similar to the previous study, an LCO transition layer was present at the LCO/LiPON interface. A nanocrystalline region was observed between the transition layer and the LiPON layer.[194] Electron holography was able to capture the positive charge distribution along the interface, indicating lithium accumulation at the nanocrystalline region and transition layer. The nanocrystalline region lacks sufficient lithium conductivity and turns out to be the source of interfacial impendence.

Later, Nomura et al. combined an *in situ* open-cell sample configuration and advanced hyperspectral image analysis to analyze lithium kinetics inside solid-state batteries. Figure 23d shows a cross-section of a battery consisting of LCO cathode and an $Li_{1+x+y}Al_x(Ti, Ge)_{2-x}Si_yP_{3-y}O_{12}$ (LASGTP) solid electrolyte. By applying non-negative matrix factorization (NMF) analysis, STEM-EELS mapping directly captured the lithium concentration change at the LCO/LASGTP interface during charging and discharging.[195] An inactive interface layer consisting of Co_3O_4 was also found at the cathode/electrolyte interface, regarded as the origin of interface resistance due to its low ionic conductivity. A lithium-rich region was observed at the grain boundaries inside the LCO cathode. Surprisingly, lithium activity appears higher in the lithium-rich region at the pristine state, namely grain boundaries in LCO. This phenomenon was further confirmed in their later study by applying a similar sample configuration and an advanced image denoising method via sparse coding.[196] High-resolution EELS mapping was able to capture the lithium redistribution at open-circuit conditions (Figure 23e). Lithium migrated along the concentration gradient to the lithium-poor region at the resting state, successfully capturing the lithium activities to achieve an equilibrium state.[196] The direct evidence of lithium redistribution highlights the importance of the resting step during battery operation to achieve a more uniform lithium distribution and lower battery polarization.

Besides LCO, NCA and NCM cathodes have also been studied for *in situ* TEM.[199] Nomura et al. applied the chip-based open cell to investigate lithium kinetics inside an NCA cathode that is paired with a sulfide solid electrolyte (Figure 23f). STEM-EELS mapping illustrates the lithium diffusion inside NCA grains and in between. It was clearly shown that particles far away from the solid electrolyte exhibit a delayed lithium extraction during charging.[197] The inactive particles highlighted in the NCM region stress the importance of reducing electrode porosity and using grains with larger sizes to reduce inactive portions and lithium diffusion barriers.

Figure 23g demonstrates a nanobattery that consists of an $Li_{1.2}Ni_{0.2}Mn_{0.6}O_2$ cathode and an LiPON electrolyte. The HADDF-STEM image at the interface indicated the formation of rock-salt and spinel structures that are commonly considered as a degradation phase of layered LTMO cathodes. Intriguingly, nanopores were observed inside such a Li-rich cathode during the charging process, as indicated by the bright-contrast regions in HAADF-STEM images.[198] This observation was proposed to be the result of the formation and movement of defects inside cathodes during the lithium extraction process.

Apart from common LTMO cathode materials, including those not highlighted here,[200−203] V_2O_5 was also investigated using *in situ* TEM to unveil their unique lithium storage mechanisms.[204,205] Numerous research efforts including *ex situ* and *in situ* characterizations were put into LTMO materials; however, *in situ* TEM shows its unique capability to visualize lithium transport and interfacial kinetics at the nanoscale and during battery operation. Such an approach has provided unprecedented and refreshing insights regarding the metastable states of LTMO cathodes.

4.2. Transition Metal Phosphates

LFP is a well-known lithium phosphate cathode that consists of an olivine crystal structure and one-dimensional lithium pathways. Its unique composition and structure render LFP a stable cathode that delivers long cycle life and has been widely used in practical commercial batteries. At the early age of exploration, *in situ* TEM was also applied to study its lithiation mechanism.

Figure 24a shows an open-cell *in situ* TEM setup using $FePO_4$ (FP) particles as the cathode in order to study the

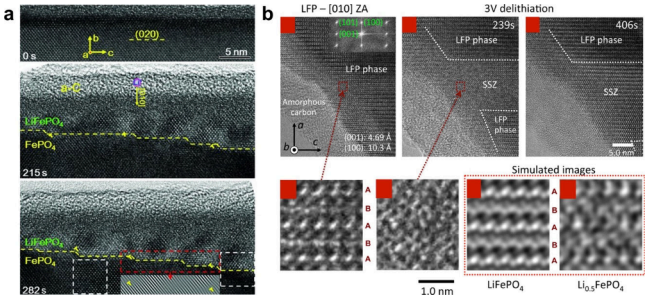

Figure 24. Lithiation and delithiation process in LFP cathodes using open-cell *in situ* TEM. (a) Reaction front probed by HRTEM images when lithiating FP particles. Reproduced with permission from ref 206. Copyright 2013 WILEY-VCH Verlag GmbH & Co. KGaA, Weinheim. (b) HRTEM images showing a solid-solution zone in LFP during high-rate delithiation. Reproduced with permission from ref 207. Copyright 2014 American Chemical Society.

lithiation process. Atomic resolution imaging uncovered that the phase boundary between FP and LFP migrates along the [001] crystal orientation, same as the lithium diffusion direction.[206] It was proposed that relaxation of the elastic strain at the interface is the major driving force for such lithiation direction. In another study employing open-cell *in situ* TEM, a solid-solution zone was found between FP and LFP regions during the high-rate delithiation process, exhibiting no dislocations and appearing stable at room temperature (Figure 24b). Such a solid-solution transition layer is proposed to enhance lithium kinetics and the rate capability of LFP cathodes.[207] This observation aligns with the approaches to reduce LFP particle size to alleviate issues related to low electronic and lithium conductivity.

Liquid cell TEM has also been applied to study LFP particle behaviors during charging and discharging. Holtz et al. combined an SiN_x-based closed cell and advanced valence EELS to uncover the delithiation process of LFP particles. By using a monochromated electron source, the energy resolution of EELS was able to achieve 0.2 eV and could be used to probe the plasmon region. EELS displayed in Figure 25a captured an

https://doi.org/10.1021/acs.chemrev.4c00507
Chem. Rev. XXXX, XXX, XXX−XXX

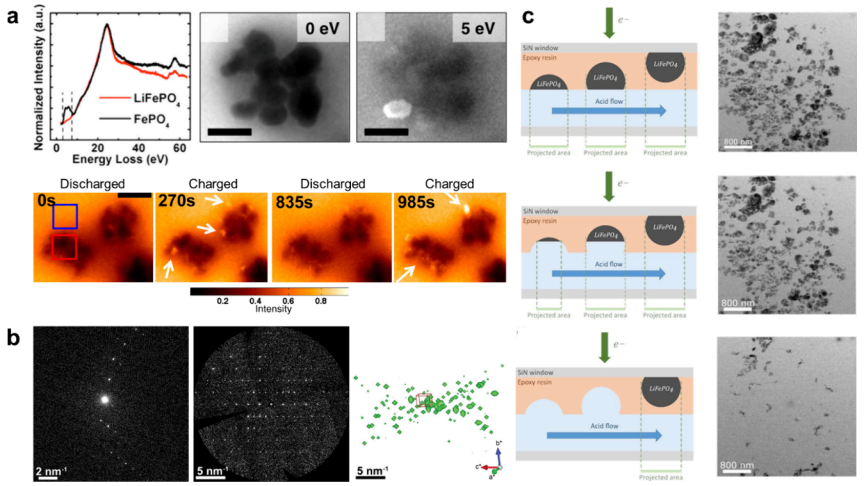

Figure 25. Microstructure changes of LFP nanomaterials during charging and discharging in liquid cell TEM. (a) Competing delithiation of LFP NPs observed by EFTEM imaging. Scale bars: 200 nm. Reproduced with permission from ref 208. Copyright 2014 American Chemical Society. (b) Electron diffraction tomography probing structural evolution in single LFP crystal. Reproduced with permission from ref 209. Copyright 2018 American Chemical Society. (c) Microstructure evolution during LFP particle dissolution in sulfuric acid. Reproduced with permission from ref 210. Copyright 2022 The Authors.

extra peak at around 5 eV in the FP sample while not in the LFP sample. When imaging with a 5 eV energy filter, one can distinguish delithiated LFP particles from pristine ones in TEM images.[208] By leveraging energy-filtered TEM (EFTEM), it was shown that a competing delithiation mechanism is present among LFP particles, along with anisotropic particle growth.

Besides valence EELS, electron diffraction tomography (EDT) was utilized in the liquid cell study of LFP particles (Figure 25b). Based on the well-documented crystal structure of charged LFP particle, Karakulina et al. applied EDT on single crystals of LFP inside a SiN_x-based liquid cell during delithiation. Crystal structure analysis at the unit cell level was achieved, with spatial identification of specific particles.[209] These techniques demonstrated their unique capability to determine crystal structure information in three dimensions, even when the spatial resolution is limited by the liquid environment. Another work in 2023 focused on the cathode recycling process using liquid cell TEM. Figure 25c illustrates the dissolution of LFP particles in sulfuric acid to mimic the recycling procedure for battery cathodes. It was shown that the initial dissolution of LFP particles appeared slow but accelerated after one-third of the entire dissolution process. This work demonstrated the advantage of combining liquid cell TEM and ultramicrotomy to prepare cathode samples with designated sizes and thickness, and investigate their dissolution kinetics in real-time.[210] Such a dissolution process ties in with the battery recycling aspect, which is one of the popular topics in the battery field for ensuring a sustainable material supply in the long run.

4.3. Transition Metal Fluorides

Conversion reactions of most transition metal compounds occur at low potentials (vs. Li/Li^+), suitable for use as anodes.[211,212] Nevertheless, several transition metal compounds, MX_z (where M = Fe, Co, Ni, Cu, etc., and X = S, F, etc.), exhibit high electrode potentials that are appropriate as cathodes.[213] Although conversion cathodes suffer from poor reversibility due to sluggish reaction kinetics, aggregation of transition metal nanoparticles, and significant voltage hysteresis, the high theoretical capacity makes them attractive candidates for extensive investigations.

Wang et al. monitored the lithiation process of FeF_2 nanoparticles during the conversion reaction and reported the gradual phase transformation from the surface to bulk.[48] By modifying the conventional tip-based open-cell configuration, the nanoparticles were dispersed on a carbon-film-supported TEM mesh grid, making contact between the carbon film and the Li/Li_2O tip, as shown in Figure 26a. This design allowed lithium ions to reach the active materials through the carbon film when an appropriate voltage bias was applied. Two different time scales for inter- and intraparticle lithium-ion transport were observed. Lithium ions moved quickly to initiate a surface reaction, leading to the formation of subnanometer Fe particles, and then extended to the bulk region at a much slower rate (Figure 26a). It showed a large volume expansion of about 41−57% after the conversion reaction. Although LiF did not exhibit a visible diffraction pattern, its formation was confirmed through EELS, suggesting the possible formation of amorphous LiF as the lithiated product. It was suggested that fast dynamics is possible for FeF_2 conversion when particle sizes are reduced to nanometers. Karki et al. observed that Fe domains grew within the FeF_2 lattice through a conversion-driven topotactic transformation, resulting in a checkerboard-like structure (Figure 26b).[214] The conversion process was initiated from the surface and propagated layer-by-layer into the bulk. During lithiation, FeF_2 transformed into well-arranged Fe nanodomains with a preferential orientation along the [110] direction of the parent FeF_2. Lithiation occurred predominantly through the [001] lithium-ion channel, pushing Fe atoms out along the [010] or [100] direction to create space for Li ions. Intriguingly, molecular dynamics simulations showed that Fe^0 atoms have higher mobility compared to Fe^{2+}. Therefore, the authors suggested that the movement of Fe allowed for the formation of Fe−Fe bonds and contraction of the Fe layer, resulting in a topotactic transformation where Fe adopted a new crystallographic orientation within the FeF_2 lattice.

A partial substitution of fluorine with oxygen in iron fluoride (FeO_xF_{2-x}, where $0.4 < x < 0.7$) has been found to enhance

https://doi.org/10.1021/acs.chemrev.4c00507
Chem. Rev. XXXX, XXX, XXX−XXX

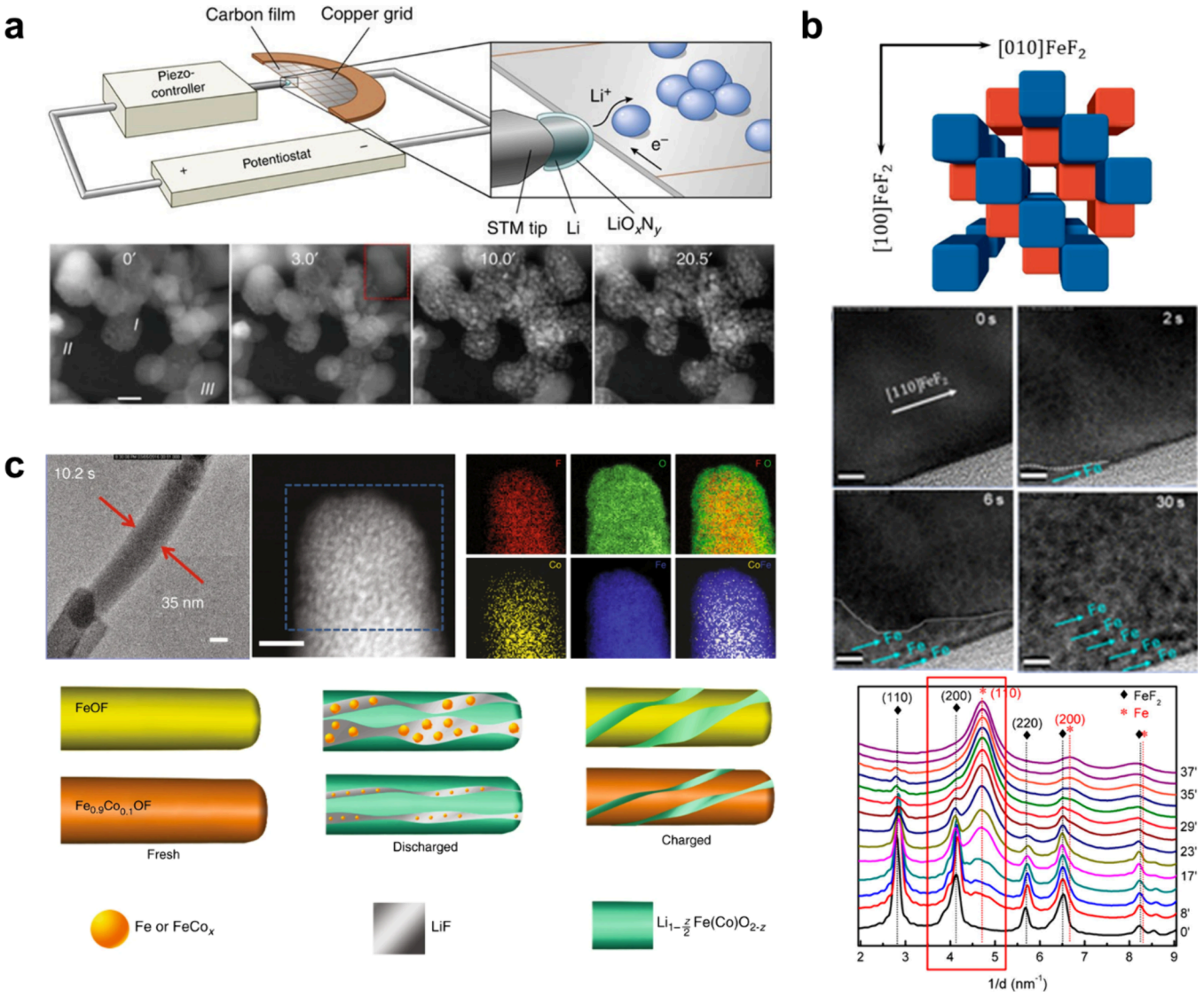

Figure 26. Lithiation/delithiation and failure mechanisms of conversion-type cathode materials. (a) Schematic illustration of the open-cell *in situ* TEM experimental design for investigating lithiation/delithiation of FeF_2 nanoparticles and corresponding time-lapse images. Scale bar: 10 nm. Reproduced with permission from ref 48. Copyright 2012 Springer Nature Limited. (b) Conversion-driven topotactic transformation of FeF_2 cathodes into Fe resulting in a checkerboard-like structure. Scale bars: 5 nm. Reproduced with permission from ref 214. Copyright 2018 American Chemical Society. (c) Comparison of conversion reaction mechanisms of $Fe_{0.9}Co_{0.1}OF$ and FeOF nanorod cathodes. Scale bars for HRTEM and ADF-STEM images: 20 and 10 nm, respectively. Reproduced with permission from ref 215. Copyright 2018 The Authors.

the electrochemical performance of iron fluoride cathodes, by transforming the less-reversible conversion reaction into a highly reversible extrusion reaction.[215−217] Fan et al. developed a high-performance Co/O doped iron fluoride ($Fe_{0.9}Co_{0.1}OF$) cathode with an energy density of ∼1000 Wh kg^{-1} and a long cycle life of 1000 cycles. The origin of this high performance was investigated using various characterization techniques, including *in situ* TEM.[215] X-ray pair distribution function (PDF) and *ex situ* TEM analysis revealed different phase distributions of $Fe_{0.9}Co_{0.1}OF$ compared to FeOF at the discharged (lithiated) state (Figure 26c). $Fe_{0.9}Co_{0.1}OF$ exhibited a dominant rock-salt phase (86.9%) over the metallic phase (13.1%), while the FeOF showed a 39.4% metallic phase and a 60.6% rock-salt phase. Moreover, the metallic nanoparticles of Fe (Co) were smaller than the Fe nanoparticles in FeOF. Those findings supported that the $Fe_{0.9}Co_{0.1}OF$ cathode operates via reaction mechanisms different from the FeOF cathode, where the conversion reaction is suppressed and the reversibility of the extrusion reaction is enhanced. Open-cell *in situ* TEM experiments unveiled a much faster reaction rate of $Fe_{0.9}Co_{0.1}OF$ compared to FeOF, forming a ∼2 nm-thick oxygen-rich layer after lithiation, which was absent in FeOF. This oxygen-rich rock salt layer was proposed to prevent electrolyte reactions with metal nanoparticles and their subsequent dissolution. In addition to the partial substitution in iron fluoride cathodes, the effects of substituting nickel with copper in NiF_2 cathodes were investigated using *in situ* TEM by Villa et al.[218] This work compared the lithiation process of NiF_2, $Cu_{0.1}Ni_{0.9}F_2$, and $Cu_{0.25}Ni_{0.75}F_2$, and identified phase transitions using SAED patterns. It was observed that the degree of areal expansion during the first lithiation decreases when Cu is substituted. This was attributed to the formation of metallic Cu, which was previously demonstrated to effectively accommodate lithiation products such as LiF by the authors.[219] It was also found that the reversibility of the conversion reaction remarkably increases in the $Cu_{0.25}Ni_{0.75}F_2$

https://doi.org/10.1021/acs.chemrev.4c00507
Chem. Rev. XXXX, XXX, XXX−XXX

cathode, which explains the benefit of Cu substitutions for enhancing electrochemical performances.

4.4. Li−S Chemistry

The exploration of advanced battery systems, such as lithium−sulfur (Li−S) and lithium−selenium (Li−Se) batteries, has garnered significant attention in recent years due to their high theoretical energy densities and potential for addressing the growing demand for energy storage solutions. In particular, Li−S batteries have emerged as promising candidates owing to the high specific capacity of sulfur cathodes, while Li−Se batteries offer advantages including higher electrical conductivity and theoretical capacity compared to Li−S systems. However, the practical implementation of these battery technologies has been hindered by various challenges, including poor cycling stability, capacity fading, and electrode degradation.[47] To overcome these obstacles, methods such as electrolyte optimization, application of CNTs, and passivation layer have been studied.[220−222] *In situ* TEM has been utilized to gain a deeper understanding of these processes by leveraging its advantages for real-time visualization. This section presents an overview of recent studies utilizing *in situ* TEM to investigate the behavior of Li−S batteries, highlighting key findings and contributions to the fundamental insights and development of these next-generation energy storage systems.

Using solid-electrolyte open-cell configuration, Kim et al. reported the first *in situ* TEM study on the lithiation process of S cathode that was confined in cylindrical CNTs.[223] To prepare sulfur-filled hollow CNTs, a 15 nm layer of carbon was deposited onto an alumina template. The template was then immersed in molten sulfur at 160 °C, allowing the sulfur to fill the hollow interior of the CNTs. Finally, the alumina template was dissolved using hydrofluoric acid, leaving behind sulfur inside the hollow CNTs. The presence of the CNTs prevented sulfur evaporation during electron beam irradiation, enabling *in situ* TEM observation of the lithiation process. Under a voltage bias of −2.0 V, sulfur inside a hollow CNT exhibited a contrast change, and the light contrast indicated a phase transition to polycrystalline Li_2S, as confirmed by the SAED patterns shown in Figure 27a. EELS analysis showed an intensity increase of the Li K-edge and a peak shift of the S L-edge, suggesting the formation of Li_2S. Several noteworthy observations were made, including a flat reaction front propagation, a constant reaction rate, no volume expansion, no fracturing of the CNT, and the absence of intermediate phases such as polysulfides and LiS. The flat reaction front and constant reaction rate were explained by the high ionic conductivity at the grain boundary of nanocrystalline Li_2S. The absence of polysulfides and the phase separation of S/Li_2S in a solid-state battery were also observed via *in situ* TEM studies by Yang et al.[224] Concerning the *in situ* TEM experiment with the open-cell configuration, they opted to make contact between the Li/Li_2O tip and a carbon supporting film on a TEM grid, instead of directly with the sulfur particle. This setup allowed lithium ions to reach the electroactive materials through the carbon film that serves as a medium. The sulfur powder was dispersed on a TEM grid and then further coated with carbon to shield it from the high-energy electron beam and the high vacuum environment. By coupling TEM imaging, ADF-STEM imaging, SAED, and EELS techniques, the phase transition of sulfur into Li_2S without the evolution of intermediate lithium polysulfides in the solid-state condition was demonstrated (Figure 27b). Moreover, the coexistence of sulfur and Li_2S nanoparticles

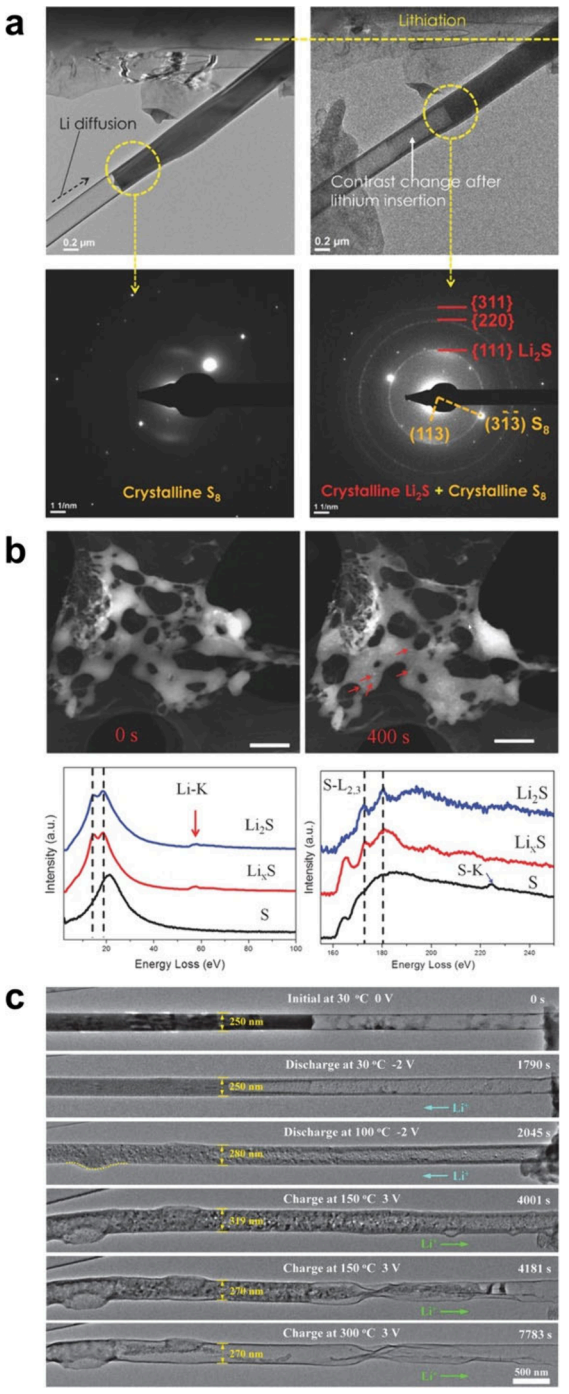

Figure 27. *In situ* TEM studies on sulfur cathodes using the open-cell configuration. (a) Lithiation of sulfur in cylindrical CNTs, showing the formation of polycrystalline Li_2S. Reproduced with permission from ref 223. Copyright 2015 WILEY-VCH Verlag GmbH & Co. KGaA, Weinheim. (b) Phase transition of sulfur into Li_2S without intermediate lithium polysulfides during lithiation of sulfur particles under solid-state conditions, and nanophase separation of S and Li_2S nanoparticles. Reproduced with permission from ref 224. Copyright 2016 WILEY-VCH Verlag GmbH & Co. KGaA, Weinheim. (c) *In situ* lithiation/delithiation of S@CNT at different voltage biases and temperatures, demonstrating sluggish lithium-ion diffusion as the limiting factor for Li_2S reversibility. Reproduced with permission from ref 225. Copyright 2020 WILEY-VCH Verlag GmbH & Co. KGaA, Weinheim.

https://doi.org/10.1021/acs.chemrev.4c00507
Chem. Rev. XXXX, XXX, XXX−XXX

implied the nanophase separation during the reactions. The aforementioned two studies suggested that the formation of nanocrystalline Li_2S forms a medium for ions and electrons to the Li_2S/S interface, providing insights into the reaction kinetics of sulfur cathodes.

Additionally, Wang et al. reported the precipitation and decomposition of Li_2S at high temperatures using a MEMS heating device in the *in situ* open-cell TEM configuration.[225] Sulfur was prepared inside a carbon nanotube (S@CNT) to prevent electron beam damage and to provide electrical conductivity to the insulating sulfur. When a negative voltage bias of −2.0 V was applied at room temperature, the nucleation of the amorphous/nanocrystalline Li_2S phase and its transition to polycrystalline Li_2S was observed. However, the as-formed Li_2S phase remained electrochemically inactive even under a high positive voltage bias of 8.0 V. Further experiments on samples with enhanced electrical conductivity did not trigger Li_2S decomposition, indicating that the electrical conductivity is not the primary limiting factor in Li_2S decomposition during charging. Delithiation from Li_2S was accomplished under a 3-V bias at 150 °C and a more thorough delithiation was observed at 300 °C, which demonstrated that sluggish lithium-ion diffusion is the limiting step determining the reversibility of Li_2S (Figure 27c). This work also illustrated that Li_2S with high crystallinity was produced at a temperature as high as 800 °C but remained undecomposed even under an 8.0 V bias, which suggests that high crystallinity is another factor responsible for Li_2S irreversibility.

Although polysulfides were not observed in solid-state batteries, the long-chain polysulfides and their dissolution into the ionic liquid (IL) electrolyte were observed by Wang et al.[226] 1-Butyl-1-methylpyrrolidinium bis(trifluoromethylsulfonyl)imide (Py_{14}TFSI) with 1.0 M LiTFSI was prepared as an IL electrolyte and a drop of IL was placed on the lithium metal surface in the *in situ* TEM sample setup (Figure 28a). Upon establishing contact between the IL and a partially empty S@CNT using the *in situ* open-cell TEM holder, the IL infiltrated the hollow CNT and intimately contacted the sulfur, resulting in the formation of a Li|IL|S@CNT (Li−S) nanobattery. During the *in situ* lithiation by the potential sweep method, the S/IL interface migrated from the IL to S, indicating the lithiated product dissolving into the IL. The electron diffraction pattern at the reaction front was indexed into the lithium polysulfide and the phase far from the reaction front was revealed to be polycrystalline Li_2S, demonstrating the formation of polysulfides and further transition to Li_2S as the final product during the lithiation. After the potential was swept back to open-circuit voltage, some semispherical sulfur was observed at the CNT wall. This work further compared the electrochemical reaction behavior using pure IL without a lithium salt. A CV scan illustrated the S_8 reduction peak at a higher potential (2.25 V (vs. Li/Li^+) in the IL with salt compared to 2.5 V (vs. Li/Li^+) in the IL without salt). Meanwhile, more precipitated S_8 species were observed after delithiation in the IL without lithium salt, together suggesting the presence of longer-chain polysulfides. This inference is based on their equilibrium potential and their characteristic propensity for easy transformation into S_8.

Later, Zhou et al. observed the liquid−solid conversion of lithium polysulfides and the collective reaction induced by metallic active centers in Li−S batteries.[47] The *in situ* liquid-phase TEM setup consists of Ti electrodes and a Li_2S_6-containing electrolyte. A negative voltage bias of −0.5 V was

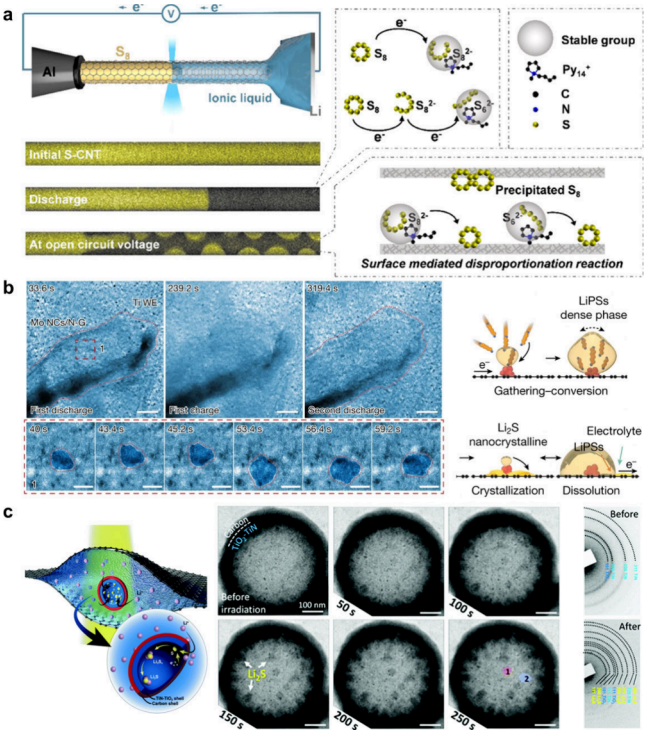

Figure 28. *In situ* TEM investigations of sulfur cathodes under liquid electrolyte environments. (a) Schematic illustrations of lithiation mechanisms of S@CNT involving lithium polysulfide formation under ionic liquid electrolyte. Reproduced with permission from ref 226. Copyright 2020 American Chemical Society. (b) Liquid−solid conversion of lithium polysulfides and collective reaction induced by metallic active centers in Li−S batteries with liquid electrolyte. Scale bars for top and bottom rows: 200 and 50 nm, respectively. Reproduced with permission from ref 47. Copyright 2023 UChicago Argonne, LLC, Operator of Argonne National Laboratory. (c) A polar TiO_2−TiN host for anchoring lithium polysulfides investigated by carbon membrane-based liquid-phase TEM. Reproduced with permission from ref 68. Copyright 2018 Royal Society of Chemistry.

applied to the working electrode to induce the liquid−solid transformation of lithium polysulfides. Two types of nucleation−growth behavior were observed: a two-step deposition and a single-step deposition. In the two-step deposition process, the formation of granular Li_2S_2 (tetragonal, $P4_2/mnm$) and the subsequent transitioning into rod-like Li_2S (cubic, $Fm\bar{3}m$) were identified, while only rod-like or plate-like Li_2S particles were observed in the single-step deposition. In addition, it was found that the concentration of Li_2S_6 in the electrolyte did not affect the nucleation−growth behavior but the applied voltage had a pronouncing effect. At −0.1 V, only two-step deposition was observed, while at −0.5 V, granular and rod-like structures formed simultaneously, indicating a charge-transfer-limited reaction. The authors also prepared Mo nanoclusters in N-doped graphene (Mo NCs/N-G) as metallic active centers to compare lithium sulfide formation behavior with that on the bare Ti electrodes (Figure 28b). With the active center, contrast changes indicate Li_2S deposition without rod-like Li_2S formation, which was identified as both face-centered cubic nanocrystalline and amorphous Li_2S by SAED patterns and HRTEM images. Additionally, lithium polysulfides aggregated on the working electrode and formed Li_2S_2 that eventually precipitated as Li_2S during discharging. In the subsequent charging step, Li_2S was able to reversibly dissolute

https://doi.org/10.1021/acs.chemrev.4c00507
Chem. Rev. XXXX, XXX, XXX−XXX

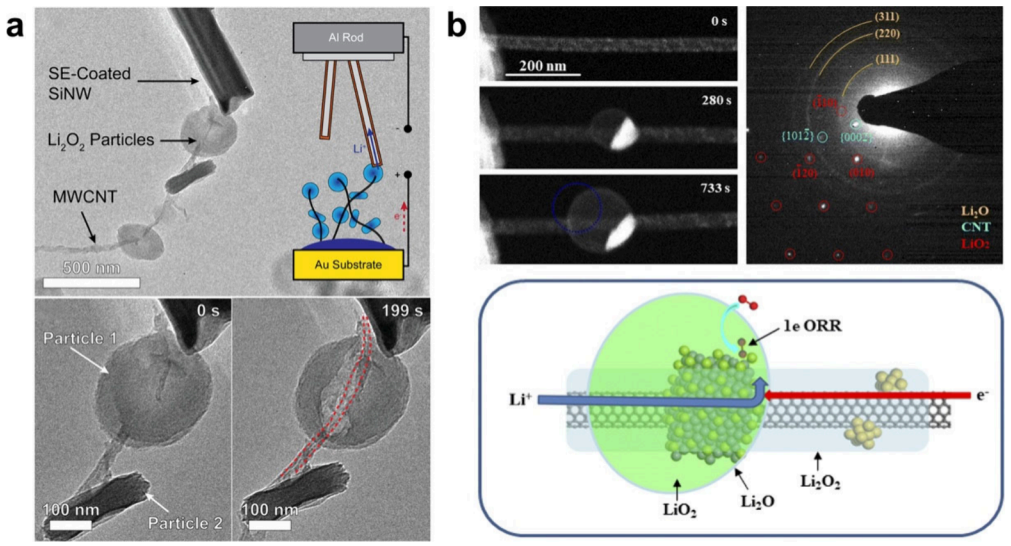

Figure 29. Open-cell *in situ* TEM studies on Li−O_2 chemistry. (a) Morphological changes of Li_2O_2 particles during delithiation process. Reproduced with permission from ref 232. Copyright 2013 American Chemical Society. (b) HRTEM and SAED analysis of metastable LiO_2 phase during lithiation process. Reproduced with permission from ref 233. Copyright 2021 Royal Society of Chemistry.

into the electrolyte in the form of soluble lithium polysulfides. Such gathering-induced collective charge transfer process provided new insights into the reaction mechanism in the Li−S system, guiding electrode optimization and system engineering to promote more reversible processes during Li−S battery operation.

Another work reported the electron-beam-induced nucleation and growth behaviors of lithium sulfides, using a carbon-membrane-based liquid cell, similar to a graphene liquid cell.[68] The authors demonstrated that polar hosts can effectively anchor polysulfides in Li−S battery systems. To explore the impact of surface chemistry on host materials in this system, a series of hollow spheres were prepared with inner and outer walls made of either nonpolar carbon or polar TiO_2−TiN. Sulfur was mixed with the hollow spheres and heated to 300 °C for 6 h under an Ar ambient for integration. During lithiation of the nonpolar C/S composite, small Li_2S particles were observed both inside and outside the sphere, indicating that polysulfides can diffuse through the hollow carbon. However, the diffusion of lithium sulfides was not observed when adopting TiO_2−TiN binary composites (Figure 28c), which suggests that the polar TiO_2−TiN layer may act as both a physical barrier and a chemical anchor wall. This is further supported by DFT calculations showing that the adsorption energies of polysulfides on TiN and TiO_2 surfaces are significantly higher than on carbon, attributed to the strong binding of Li_2S_x monomers to Ti−S and Li−S/O bonds. In addition, the radial expansion of lithium sulfides showed diffusion-limited kinetics initially, which later shifted to reaction-limited kinetics. Although such observation is contradictory to the diffusion-controlled growth of lithium sulfides found via *in situ* open-cell TEM by Tang et al., the authors suggested that the reasons might lie in the differences in the host materials or the electrolyte.[227] In Xu's work, the cause for the mechanism change was attributed to the transition from more conductive TiN to less conductive TiO_2.[68] Based on the findings, they proposed an optimal polar (inner) and nonpolar (outer) dual-walled sphere host structure for sulfur, e.g., C/TiO_2−TiN/S, and its excellent electrochemical performance was demonstrated, exhibiting a capacity of 4.3 mAh cm^{-2} over 400 cycles at a low electrolyte/sulfur ratio of 6.8 mL g^{-1}. Tan et al. also developed a high-performing Li_2S@graphene nanocapsule cathode by burning lithium foils in a CS_2 vapor.[228] Li_2S@graphene nanocapsules were synthesized by reacting lithium metal foil with CS_2 vapor under argon at 650 °C for 5 h, simultaneously producing Li_2S nanocrystals encapsulated by graphene layers. Their structural stability was examined using open-cell *in situ* TEM. The Li_2S nanocrystals encapsulated with a few graphene layers showed small volume variations of 10−20% during cycles, which is much smaller than bare Li_2S. Moreover, the Li_2S@graphene particle maintained good structural integrity even under a large bias condition (6.0 V) for tens of cycles. Cracking was observed in the later cycles, gradually increasing and leading to the formation of inactive sulfur.

Selenium (Se), akin to sulfur in its chemical properties, has also been explored as a potential cathode material. Se cathode has a higher electrical conductivity compared to sulfur and a high theoretical capacity of 675 mAh g^{-1}, leading to substantial research in Li−Se batteries. Li et al. conducted *in situ* TEM studies with the open-cell configuration to investigate the kinetics and lithiation mechanism of Se nanotubes.[229] The authors observed a single-step lithiation reaction, transforming single-crystalline Se into polycrystalline Li_2Se with approximately 88% volume expansion. Guo et al. also investigated the behaviors of Se nanowires at high temperatures.[230] The polycrystalline face-centered cubic (FCC) Li_2Se phase was confirmed by a SAED pattern, indicating a direct conversion reaction from Se to Li_2Se without intermediate phases such as polyselenides, which is consistent with the results performed by Li et al.[229] Interestingly, Li_2Se decomposition was only accomplished during *in situ* charging at high temperature of 300 °C, which implies that ionic conductivity dictates the reversibility of Li_2Se in solid-state batteries. These findings resemble earlier *in situ* TEM results for Li_2S,[225] indicating potential similarities in the lithiation/delithiation behaviors of sulfur and selenium.

https://doi.org/10.1021/acs.chemrev.4c00507
Chem. Rev. XXXX, XXX, XXX−XXX

4.5. Li−Air Chemistry

The Li−air battery mainly refers to Li−O_2 chemistry, with O_2 gas serving as the active material in the cathode, while Li−CO_2 chemistry is another branch under this category.[231] The major development of the Li−air battery occurred in the mid-2010s and it is still under extensive study. The driving force for researching in Li−air battery is its extremely high theoretical capacity and high gravimetric energy density due to the lightweight of the O_2 cathode. However, the poor cycle life caused by the irreversibility of the O_2 cathode and the challenges in managing air to avoid side reactions between Li and other air components have posed significant hurdles to realizing this battery chemistry in practical use. As cathode reaction involves gas−solid interaction that occurs at the nanoscale, *in situ* TEM is a perfect tool to study the reaction mechanism of the O_2 cathode, and how catalysts can facilitate the delithiation process.

4.5.1. Lithiation Mechanisms. As lithium oxide (Li_xO) species are formed as the lithiated products in Li−O_2 batteries, it is crucial to understand the formation process of Li_xO under battery operating conditions. Zhong et al. employed a solid-electrolyte open-cell sample configuration that consists of a Si nanowire anode coated with a $LiAlSiO_x$ solid electrolyte and lithium peroxide (Li_2O_2) cathode particles loaded on multiwall carbon nanotubes (MWCNTs) to study the delithiation process (Figure 29a). It was found that under high overpotential, Li_2O_2 likes to be oxidized near the interface between Li_2O_2 particles and MWCNT instead of at the interface between the cathode and electrolyte.[232] The direct observation strongly suggested that the limiting factor for the reversibility of the O_2 cathode is electronic conductivity but not ionic conductivity at a high driving force.

Another work focused on the formation process of a lithium superoxide (LiO_2) using a solid-electrolyte open-cell setup in an environmental TEM setup (Figure 29b). An Au-coated CNT was used as the counter electrode while Li_2O/Li was used as the electrolyte and anode. Upon discharging in the O_2 environment, the Au layer was first alloyed with Li and experienced radial expansion. Afterward, a light-contrast particle formed near the Au alloy particle. Electron diffraction identified the presence of LiO_2 with a mixture of Li_2O as the lithiated products. The LiO_2 phase was observed to be stable for several minutes during the reaction, as opposed to the general belief of its metastability.[233] It was proposed to be the result of the weakened electron donation capability of Li due to the interaction between Li and Au/O species. Regardless, the observation of LiO_2 has provided direct evidence of LiO_2 as a possible lithiated product in the Li−O_2 battery.

Liquid-cell TEM also proved its effectiveness in monitoring the lithiation mechanism of Li−O_2 chemistry. Kushima et al. used Au as the cathode current collector in a SiN_x-based liquid cell to study the charging/discharging process of Li_2O_2. The liquid electrolyte was saturated with O_2 before the test.

Figure 30a shows that different Li_2O_2 nucleation modes were found when applying different overpotentials. Under low overpotential, thin film growth of Li_2O_2 was observed, whereas particle growth was observed when applying high overpotential.[234] Such phenomena suggested the lithiation process is ion-diffusion-limited. On the contrary, delithiation was found to occur at the interface between gold and Li_2O_2, indicating that electron transport is the limiting step for delithiation, in consistence with previous observations in open cells.[232] Similar morphology of Li_2O_2 nuclei was observed in several other studies with SiN_x-liquid cells.[235,236] Figure 30b illustrates the Li_2O_2 growth mechanism under a constant current instead of constant voltage. Liu et al. observed porous Li_2O_2 nucleation and growth around the Au electrode. The reverse delithiation surprisingly took nearly the same amount of time as lithiation, indicating a low current density was essential to balance the impacts of electrical conductivity and ionic conductivity of Li_2O_2.[235]

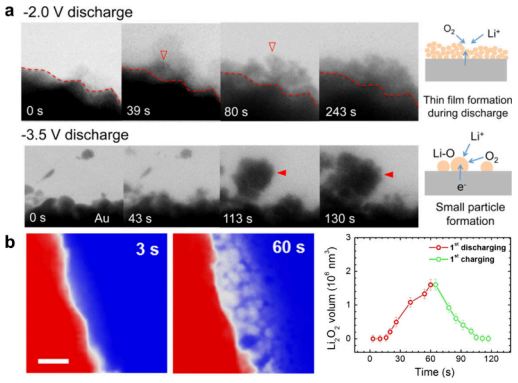

Figure 30. Li_xO formation mechanism probed using closed-cell *in situ* TEM. (a) Morphological evolution during Li_2O_2 formation through potential control. Reproduced with permission from ref 234. Copyright 2015 American Chemical Society. (b) Li_2O_2 growth mode by HRTEM image under constant current control. The blue region represents the electrolyte and white region represents Li_2O_2. Scale bar: 100 nm. Reproduced with permission from ref 235. Copyright 2018 The Authors.

The Li_xO formation mechanism has been extensively studied using both open-cell and closed-cell configurations. Open-cell TEM owns the merits of O_2 atmosphere that provides sufficient O_2 supply during electrochemical process compared with closed-cell tests, where O_2 solubility is usually in the liquid. Nevertheless, in both environments, the formation of Li_xO, namely the discharge process, was found as the ion-diffusion-limiting reaction, while the decomposition of Li_xO was found to be an electron-conduction-limiting process. Such nanoscale insights would guide cell engineering in practical batteries so that suitable strategies can be applied to selectively resolve the issues during different processes.

4.5.2. Effects of Reaction Mediators and Catalysts. Due to the strong binding between Li and O and low electronic conductivity, Li−O_2 batteries always suffer from large cell polarization and sluggish reaction kinetics. One way to accelerate the reaction kinetics is to add a catalyst or reaction mediator (RM) to lower the energy barrier for Li_xO decomposition. Numerous works have been performed on studying the reaction kinetics in the presence of various catalysts/RMs. *In situ* TEM provides an ideal platform to observe the catalysis process and help find the best catalyst from a nanoscale perspective.

Yang et al. monitored the charging/discharging of a Li−O_2 battery inside a SiN_x-based liquid cell, where a redox mediator tetrathiafulvalene (TTF) was used in $LiClO_4$-dissolved DMSO electrolyte. The reactions between the mediator and Li_2O_2 are as follows (eqs 3 and 4):

$$TTF \rightarrow TTF^+ + e^- \quad (3)$$

$$2TTF^+ + Li_2O_2 \rightarrow 2Li^+ + O_2 + 2TTF \quad (4)$$

https://doi.org/10.1021/acs.chemrev.4c00507
Chem. Rev. XXXX, XXX, XXX−XXX

The soluble TTF component did not show an impact on the formation of Li_2O_2 during the discharging process, while it tremendously helped the charging process. Figure 31a

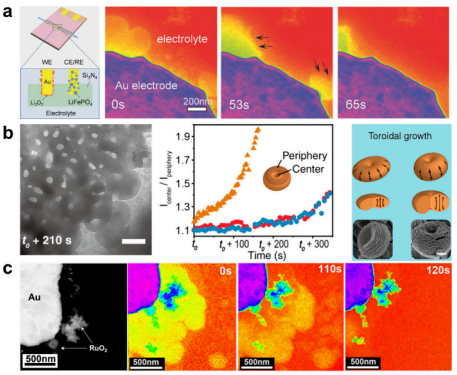

Figure 31. Li_xO decomposition process activated by the reaction mediator and catalyst probed using closed-cell *in situ* TEM. (a) HRTEM images showing Li_2O_2 decomposition aided by TFF reaction mediator. The yellow region represents dissolving Li_2O_2, and the red region represents electrolyte. Reproduced with permission from ref 237. Copyright 2017 WILEY-VCH Verlag GmbH & Co. KGaA, Weinheim. (b) Micromorphology examination indicating the growth of toroidal Li_2O_2 aided by DBBQ reaction mediator. Scale bar: 500 nm. Reproduced with permission from ref 239. Copyright 2019 American Chemical Society. (c) RuO_2 catalyst promoted the formation and decomposition of Li_2O_2 by HRTEM imaging. Yellow, red, and blue regions represent dissolving Li_2O_2, electrolyte, and RuO_2 catalyst, respectively. Reproduced with permission from ref 238. Copyright 2018 Elsevier Ltd.

demonstrates the dissolution of Li_2O_2 on the Au electrode, where the dissolution took place at the Li_2O_2/electrolyte interface, and no residual Li_2O_2 was observed after the delithiation process. A much lower charging voltage was also obtained using TTF when compared with the process without TTF.[237] *In situ* TEM results provided direct evidence that TTF was able to mediate the dissolution process of Li_2O_2 and facilitate the reaction kinetics in the Li−O_2 system.

Another work by Lee et al. used 2,5-di*tert*-butyl-1,4-benzoquinone (DBBQ) as the reaction mediator to promote the formation of Li_2O_2 (Figure 31b). Detailed analysis demonstrated that Li_2O_2 first follows lateral growth into disk-like morphology and then grows vertically to form a toroidal structure in the presence of DBBQ.[238] The altered growth kinetics provide insight into mediating the controllable lithiation process of Li_2O_2 for Li−O_2 batteries.

Besides the reaction mediator, the catalyst is another common chemical to promote the reaction kinetics. Figure 31c shows the effects of the catalyst on Li_2O_2-associated reaction in the Li−O_2 battery. An Au electrode was used as the counter electrode and RuO_2 served as the catalyst for both the lithiation and delithiation processes. A reduced cell polarization was obtained when using RuO_2 in the system. *In situ* TEM was able to capture the Li_2O_2 dissolution catalyzed by RuO_2, where delithiation occurred at the electrolyte−RuO_2−Li_2O_2 triple phase interface. RuO_2 further promoted the dissolution of Li_2O_2 isolated particles that already lost electrical connection to the electrode, indicating its positive impact on many aspects inside the Li−O_2 battery.[239] However, a general question regarding adding a catalyst into the electrochemical system is whether the heavy-metal-containing catalyst significantly decreases the gravimetric energy density of the battery, compromising its lightweight advantage. As promising as catalysts are in promoting the desired electrochemical reactions, further optimization will be required to balance the extended cycle life and gravimetric energy density of Li−O_2 batteries. Later, a combination of reaction mediator and catalyst were applied in the Li−O_2 system and proven effective.[240] Nevertheless, the question regarding the balance between cyclability and energy density stands.

5. *IN SITU* TEM STUDY OF ELECTROLYTES FOR LITHIUM BATTERIES

Electrolytes play a crucial role in the electrochemical behaviors of lithium batteries, while there is a lack of studies focused on electrolytes via *in situ* TEM, especially in the case of liquid electrolytes, due to low crystallinity and susceptibility to electron beams. Most *in situ* TEM studies related to electrolytes primarily concentrated on how different electrolytes affect the behavior of each active component in lithium batteries, which have been covered in previous sections. In this section, we listed *in situ* TEM efforts with a focus on the electrolyte materials.

5.1. Liquid Electrolytes

Abellan et al. examined the degradation mechanisms of liquid electrolytes under *in situ* liquid-phase TEM.[241] Several electrolytes with different salts and solvents were compared to identify the individual effects of these components on electrolyte stability (Figure 32a). The formation of nano-

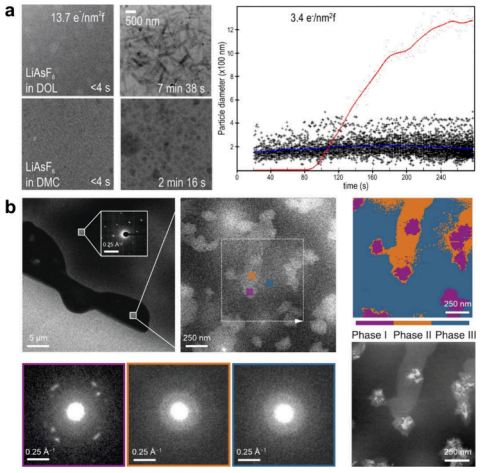

Figure 32. Liquid-phase TEM investigations on liquid electrolytes. (a) Comparison of liquid electrolyte degradation between different solvents under electron beam irradiation. Reproduced with permission from ref 241. Copyright 2014 American Chemical Society. (b) Investigation of structural order of 1 M $LiPF_6$ in 1:1 EC/DEC at −30 °C using integrated techniques including liquid-phase TEM, cryo-TEM, 4D-STEM, and deep learning data analysis. Reproduced with permission from ref 29. Copyright 2023 The Authors.

particles by radicals after electron beam irradiation was confirmed in electrolytes consisting of a $LiAsF_6$ salt dissolved in DOL, DMC, and EC/DMC solvents. Particularly in the DOL solvent, nanoparticles were observed since the first imaging frame, which later grew into nanorods. The formation of nanorods suggested unidirectional growth due to the continued reaction of organic components. In addition, faster degradation was observed in DMC compared to EC/DMC. In DMC, the nanoparticles stabilized at approximately 200 nm in

https://doi.org/10.1021/acs.chemrev.4c00507
Chem. Rev. XXXX, XXX, XXX−XXX

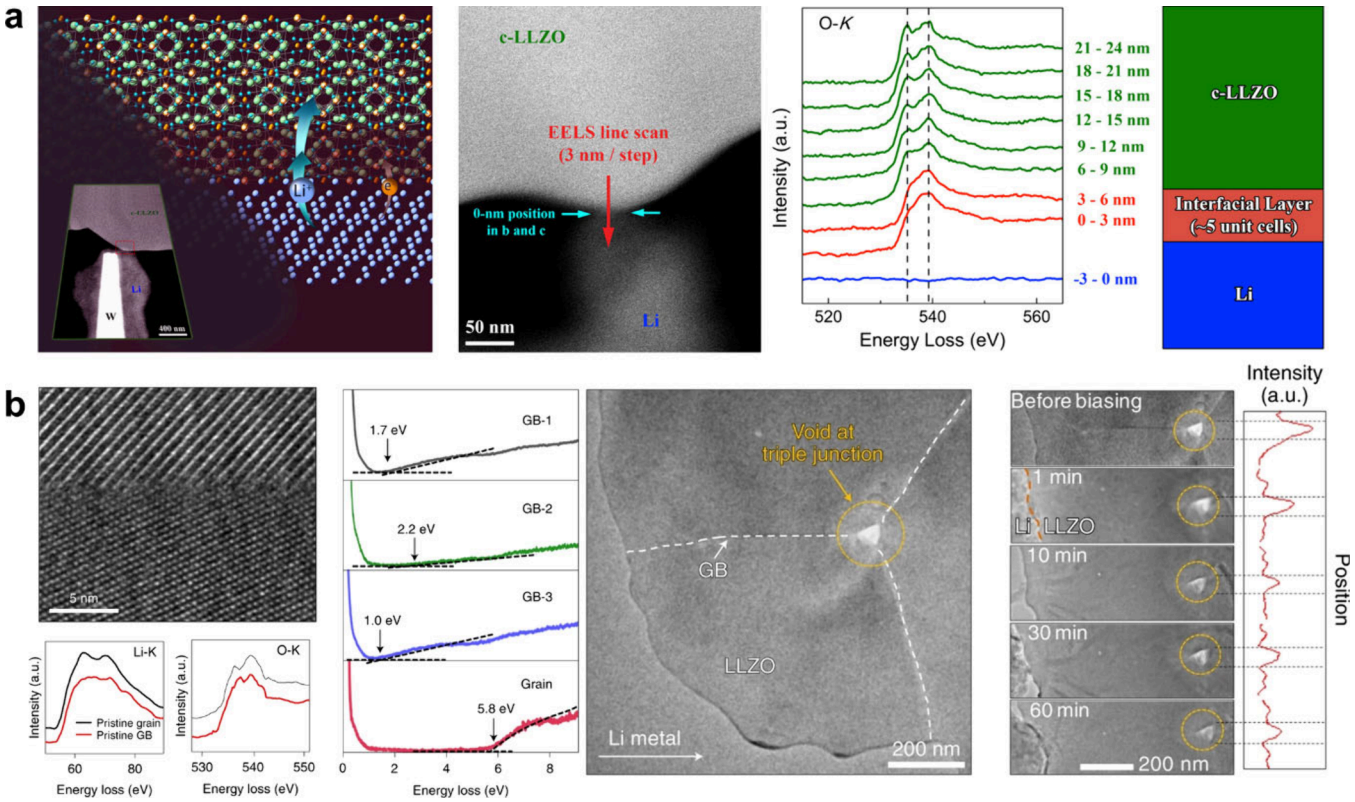

Figure 33. Interfacial stability of LLZO against Li metal probed by open-cell *in situ* TEM. (a) HRTEM and EELS analysis showing tetragonal LLZO interphase formation upon contacting Li metal. Reproduced with permission from ref 50. Copyright 2016 American Chemical Society. (b) Bandgap measurements at LLZO grain boundaries by valence EELS. Li metal nucleation at LLZO grain boundary observed by HRTEM images. Reproduced with permission from ref 44. Copyright 2021 The Authors, under exclusive license to Springer Nature Limited.

size, after which secondary larger particles grew rapidly. Based on HAADF-STEM images, it was indicated that large secondary particles could be the polymerized organic materials (with low atomic number), while the small primary particles could be the inorganic materials (with high atomic number). Their growth rate follows a power law function, with the primary particles exhibiting diffusion-limited growth and the secondary particles exhibiting reaction-limited growth according to the Lifshitz−Slyozov−Wagner (LSW) growth model. Moreover, this study demonstrated that $LiPF_6$ salts are more stable than $LiAsF_6$ in EC/DMC solvent environments.

By leveraging cryo-TEM, 4D-STEM, and deep learning methods, Xie et al. utilized *in situ* liquid-phase TEM to resolve the structural ordering of an organic liquid electrolyte at a low temperature.[29] At −30 °C, a partial region of the electrolyte composed of 1 M $LiPF_6$ in EC/DEC solvent retained the liquid form and exhibited phase separations. Three phases were identified using 4D-STEM measurement based on contrast differences (Figure 32b). Notably, in the bright region, a long-range ordered poly crystalline structure (Phase 1) was embedded in the dense liquid phase (Phase 2). In the dark region (Phase 3), a diffraction pattern similar to Phase 2 was observed, except for the scattering signature at the peak around 0.23 $Å^{-1}$ in Phase 2. The distinct peak at 0.23 $Å^{-1}$ indicates the presence of short-range order with a length of 4.34 Å, as it matched well with the mean distance of the first peak in the P−F radial distribution function (RDF) in the high-concentration electrolytes, indicated by molecular dynamics simulation. Consequently, the authors proposed the presence of a dense liquid phase with short-range ordering, which likely represents the state before $LiPF_6$ precipitation upon cooling. EELS mapping data also supported this hypothesis by showing a high concentration of $LiPF_6$ in this region.

5.2. Solid Electrolytes

Solid electrolyte materials generally include lithium-containing oxides, sulfides, halides, polymers, etc., each of which exhibits its unique advantages and drawbacks. Common oxide-based electrolytes include LLZO (garnet-type), LLTO (perovskite-type), and LATP (NASICON-type), while sulfide-based electrolytes consist of Li_6PS_5Cl (argyrodite-type), $Li_{3.25}Ge_{0.25}P_{0.75}S_4$ (thio-LISICON), and $Li_2S−P_2S_5$ systems (glass and glass−ceramic sulfides). PEO-based solid polymer electrolytes (SPEs) and gel polymer electrolytes (GPEs) are the popular polymer electrolytes. Another category falls into glassy electrolytes, i.e., LiPON and lithium borate chemistries, etc.

Solid electrolytes present promising attributes for lithium batteries for enhanced safety, higher energy density, and extended cycling life. However, many of them suffer from issues such as insufficient ionic conductivity, narrow electrochemical windows, high processing costs, or air sensitivity. Interfacial degradation including continuous interphase formation and lithium dendrite formation has been a crucial concern for many of these solid electrolytes. Although numerous strategies have been applied to mitigate interfacial reactions between solid electrolytes against electrodes, where certain solid electrolytes have delivered benchmarking electrochemical performance,[10] more research efforts are pressingly needed to address existing interfacial problems. *In situ* TEM serves as an ideal tool to study the degradation mechanism

https://doi.org/10.1021/acs.chemrev.4c00507
Chem. Rev. XXXX, XXX, XXX−XXX

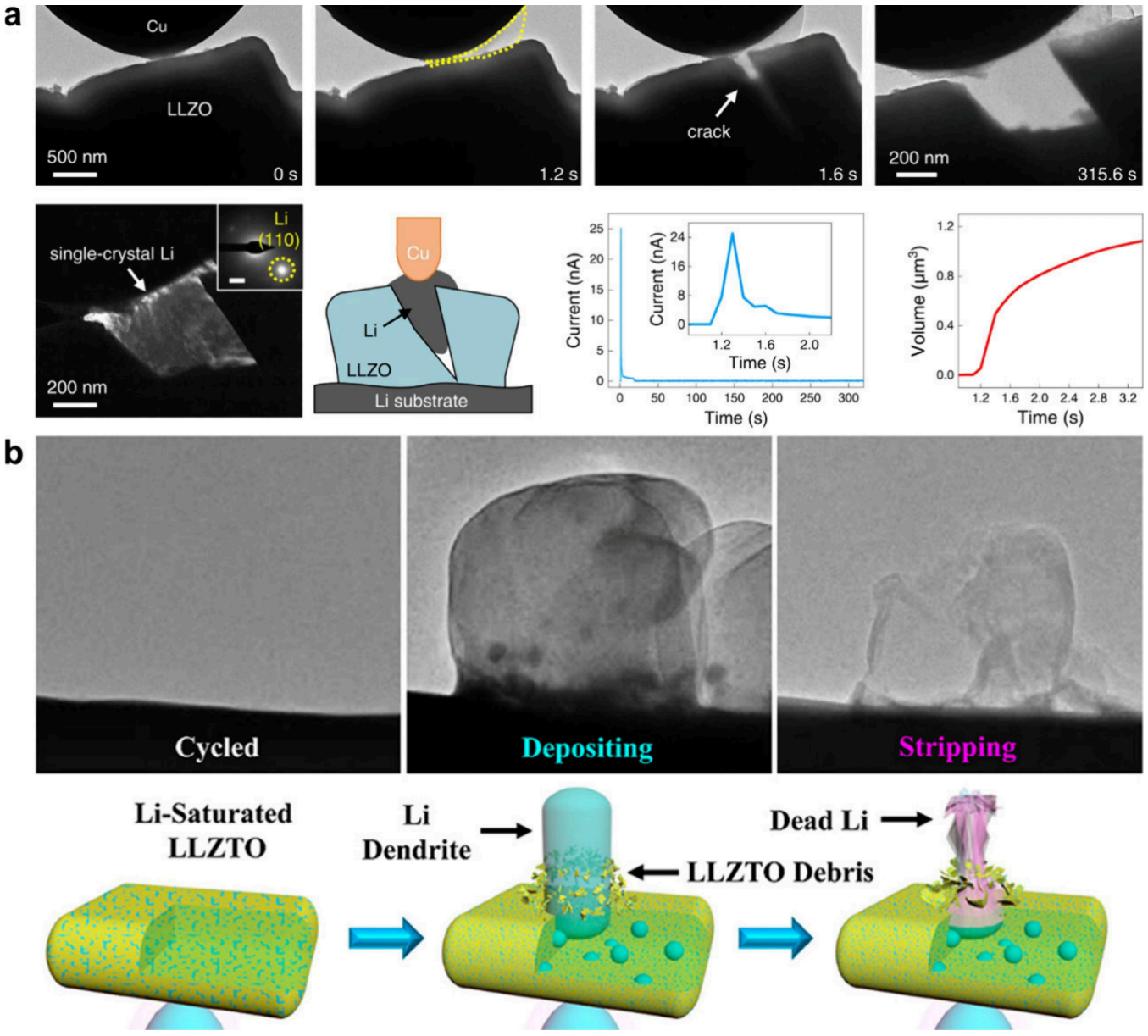

Figure 34. Mechanical properties of LLZO investigated by open-cell *in situ* TEM. (a) Low-magnification TEM images of LLZO cracking due to Li dendrite penetration. Reproduced with permission from ref 242. Copyright 2022 The Authors. (b) Dead Li formation on Ta-doped LLZO by low-magnification TEM images and corresponding schematics. Reproduced with permission from ref 243. Copyright 2021 American Chemical Society.

between solid electrolytes and electrodes since it probes reaction dynamics and can emulate practical operation conditions. Many *in situ* TEM works documented in literature have provided useful insights for interface engineering in practical solid-state batteries.

Nevertheless, due to either air sensitivity or electron beam susceptibility, a large portion of solid electrolytes are not suitable for *in situ* TEM examinations. Herein, we summarized some exemplary *in situ* TEM works particularly performed on LLZO and LiPON material systems below.

5.2.1. LLZO. Garnet-type LLZO is one of the most widely studied solid electrolytes owing to its high ionic conductivity, mechanical strength, and compatibility with common electrodes. However, it has been reported that dendrite growth could occur within the LLZO pellet, which requires a nanoscale understanding of its stability against Li metal.

5.2.1.1. Interfacial Stability. Figure 33a shows an *in situ* formation of the interphase between LLZO and Li metal inside TEM using solid-electrolyte open-cell configuration. Li metal piece coated on the W tip was moved toward crystalline LLZO and triggered a chemical reaction with LLZO. EELS analysis along the reacted region unveiled an interface with a thickness of ~6 nm, where the LLZO structure transformed from the cubic to the tetragonal phase.[50] Although the interphase was formed as soon as they were in contact, it did not continuously grow and stopped at a length of about 5 unit cells of LLZO, manifesting a passivation effect against reductive Li metal. Interphase as such will be expected to help stabilize solid electrolytes when in contact with the Li anode.

Another work performed by Ma et al. utilized a similar sample configuration and examined the electrochemical stability of LLZO at its grain boundaries. As shown in Figure 33b, valence EELS suggests that the electronic conductivity at

https://doi.org/10.1021/acs.chemrev.4c00507
Chem. Rev. XXXX, XXX, XXX−XXX

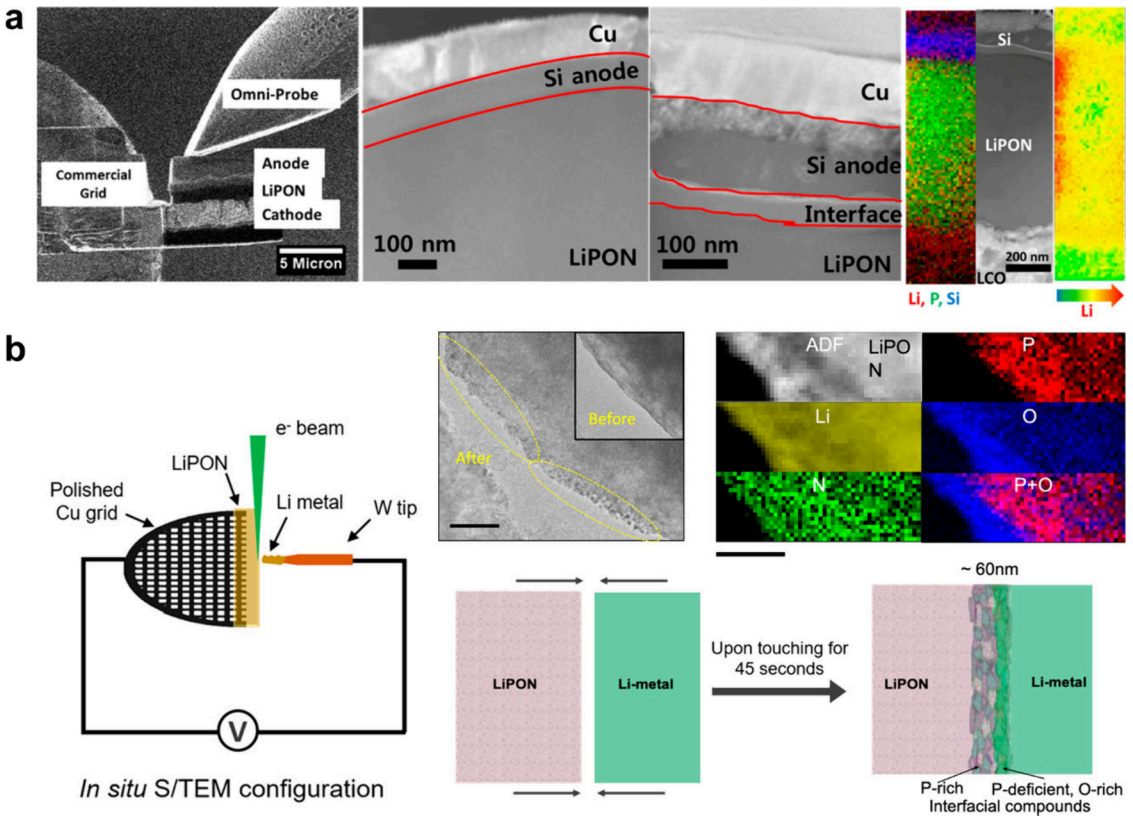

Figure 35. Evolution of interphase between LiPON and electrodes via open-cell *in situ* TEM. (a) HRTEM images and EELS mapping of charged Si/LiPON interface showing lithium accumulation. Reproduced with permission from ref 73. Copyright 2014 American Chemical Society. (b) *In situ* formed Li/LiPON interphase analyzed by HRTEM and EELS. The proposed interphase model is depicted in the schematic. Reproduced with permission from ref 246. Copyright 2021 American Chemical Society.

the grain boundaries within LLZO is generally higher than that of bulk grains. Such characteristics render the grain boundaries susceptible to more active electron conduction and then metallic Li formation inside the LLZO electrolyte. *In situ* open-cell TEM successfully captured the formation of Li metal at a triple junction point within LLZO lamella when a negative bias was applied to it. EELS further confirmed the presence of Li metal and suggests that grain boundaries indeed can induce local current hotspots and promote dendrite growth.[44] Such findings stress the grain boundary engineering and current density control especially for crystalline solid electrolytes so that internal short-circuiting can be avoided in solid electrolytes.

5.2.1.2. Mechanical Considerations. Owing to the nature of oxide materials, LLZO generally shows high yield strength and good mechanical rigidity. It has been speculated that LLZO can suppress the growth of Li metal dendrite because it is mechanically strong. Gao et al. tested this hypothesis by growing Li metal dendrite with an *in situ* solid-electrolyte open cell, which consists of an LLZO solid electrolyte, a Li metal piece as anode, and a Cu tip as the counter electrode. Figure 34a demonstrates a fractured single-crystal LLZO particle with the stress generated by Li dendrite growth, corresponding to the sudden current spike observed in the I-t plot. In the other two cases demonstrated in this work, LLZO was able to retain its structure when Li-growth-generated stress can be released via either counter electrode deformation or dendrite deformation.[242] Direct observation here confirmed that such built-up stress is able to crack single-crystal LLZO particle without apparent defects. Chemo-mechanical simulation suggested that the stress generated locally by Li dendrite at high current densities of 2 A/cm^2 could reach up to GPa levels, sufficient to cause fracture of LLZO particles. This provides critical insights regarding cell engineering using the LLZO solid electrolyte, and likely any other types of crystalline solid electrolytes. Proper measures need to be employed to ensure that stress can be effectively released during Li metal growth, thereby preventing particle fracture and short-circuiting in solid electrolytes.

In another work, Sun et al. applied an *in situ* sample setup similar to the solid-electrolyte open cell to examine Li dendrite growth from a Ta-doped LLZO (LLZTO) solid electrolyte. Repeated Li metal plating and stripping were monitored, during which dead Li formed on the surface of LLZTO due to the loss of electrical connection (Figure 34b).[243] The Li metal growth on the LLZTO surface was proposed to be a result of dendrite penetration through the electrolyte, which might also be Li extraction from LLZTO itself since Li plating on top of the LLZO pellet has been observed elsewhere before.[244] Regardless, due to the different nucleation sites for each cycle, dead Li formation and SEI accumulation occurred on the LLZTO surface, which can be regarded as one of the major reasons for Li inventory loss in practical solid-state batteries.

5.2.2. LiPON. LiPON is essentially nitrogen-doped lithium phosphate and a glassy thin film solid electrolyte. The sputtering process during LiPON synthesis amorphized its structure and granted it a fully dense feature that is ideal for solid-state electrolytes. Over the last 30 years, LiPON has been extensively studied owing to its well-known electrochemical stability against Li metal, although the root cause of the

https://doi.org/10.1021/acs.chemrev.4c00507
Chem. Rev. XXXX, XXX, XXX−XXX

stability remains in debate. A cryogenic TEM study unveiled a multilayer interphase formed between Li metal and LiPON that passivates and protects the interface.[245] Nanoscale insights of the interphase have been probed via *in situ* TEM.

Santhanagopalan et al. captured the interphase formation between LiPON and the Si anode using a probe-assisted chip-based open-cell configuration. Figure 35a illustrates the clear evidence of extra layers formed at the Si/LiPON interface. STEM-EELS analysis uncovered a Li-rich layer at the Si/LiPON interface, indicating the presence of lithium accumulation.[73] Such lithium accumulation was proposed to be the cause of increased cell impedance during repeated cycling.

In another work employing a solid-electrolyte open-cell configuration, Li metal was precisely controlled to make contact with the LiPON electrolyte that was deposited on a half Cu grid (Figure 35b). When a negative bias was applied, the interphase between Li and LiPON started to form and kept growing for ~40 s under 5-V external stimuli.[246] A 60 nm-thick interphase was found to be rich in P and O signals, in line with the *ex situ* observation using cryo-TEM. The direct evidence confirmed the root cause of the electrochemical stability at the Li/LiPON interface, where interfacial decomposition appears self-passivating. Such a formed interphase serves as a good ionic conductor and electronic insulator, which are the attributes for an ideal good SEI.

Solid-state battery research took off in the mid-2010s, with numerous research and industrial efforts dedicated to the field. It turns out now that further optimization of solid-state batteries really ties in with the nanoscale phenomena, which is related to the solid electrolyte itself but also closely related to its interfaces with electrodes. *In situ* TEM presents the ultimate advantage of observing dynamic changes with high spatial/temporal resolution, pushing forward the global commercialization of solid-state batteries.

6. BEYOND LITHIUM BATTERIES

Lithium battery technology is currently the dominant branch in the battery industry owing to its intrinsic advantages over other chemistries and its long development history. Decades of efforts have successfully transformed research results into portable electronics and electrical vehicles. Nevertheless, as lithium sources are not geologically infinite and the transition metal species become increasingly pricy, there is an urgent need to find alternatives besides lithium batteries, namely those containing Na, K, Mg, Ca, and Al, etc. These battery chemistries have all shown promise toward different specific applications. Except for Na batteries that have been commercialized in some countries, most of the rest are still in the research phase. *In situ* TEM provides a powerful tool to look at metal nucleation, lithiation mechanism, degradation pathways, and interface formation, etc. in these batteries. As *in situ* TEM has greatly expanded our understanding in the field of lithium batteries, now it is also playing a critical role in advancing battery technologies beyond lithium chemistries.

6.1. Sodium Batteries

Sodium batteries use Na ions as the conducting species, which have seen remarkably fast market growth over the past years. Sodium batteries are considered the best alternatives to lithium batteries due to merits such as the earth's abundance of Na elements, low cost of raw materials, less environmental impact, etc. Along with extensive research efforts, commercialization of Na-ion batteries has been realized in certain countries. In order to further enhance the energy density, cyclability, and safety of sodium batteries, the use of Na metal and solid-state electrolytes are considered as the major directions. In this section, we summarize the research efforts via *in situ* TEM in various branches of sodium batteries, including Na metal, Na ion, Na−S, and Na−air batteries.

6.1.1. Na Metal Batteries. As the Li metal anode is regarded as the "holy grail", Na metal also appears as a promising anode for sodium batteries due to its high theoretical capacity of 1165 mAh g^{-1}. However, continuous SEI formation and Na dendrite growth lead to severe capacity loss and safety concerns for Na metal batteries. Numerous research has been focused on understanding the nucleation and growth mechanism of Na metal in various environments that include different media (i.e., liquid or solid), different compositions (i.e., solvents, additives, etc.), and different external controls (i.e., pressure control), etc. *In situ* TEM was able to help capture the growth mechanisms of Na metal.

Geng et al. applied a solid-electrolyte open-cell configuration to study Na metal growth patterns in CO_2-containing environmental TEM. The sample setup consists of an MWCNT as the counter electrode and Na_2CO_3-coated Na metal as the solid electrolyte and anode. Figure 36a

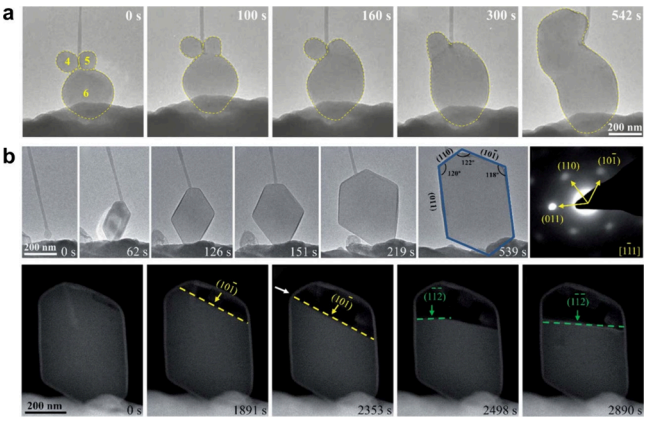

Figure 36. Na metal plating and stripping processes monitored via open-cell *in situ* TEM. (a) HRTEM images of Na metal evolution during plating. Reproduced with permission from ref 247. Copyright 2021 Tsinghua University Press and Springer-Verlag GmbH Germany, part of Springer Nature. (b) Wulff-structured Na nucleation and layer-by-layer Na metal stripping process observed by HRTEM. Reproduced with permission from ref 248. Copyright 2021 Royal Society of Chemistry.

demonstrates that in the early stage of Na metal growth, adjacent Na metal deposits or small Na metal particles tend to merge together through Ostwald ripening. The smaller particles experienced mass loss and eventually disappeared.[247] In the meantime, the adjacent larger particles kept growing and eventually remained as the only particles in the original local position. Such an intriguing phenomenon is important to understand the microscale growth patterns of Na metal, which might be caused by the electrochemical potential difference between adjacent particles.

In another case, Na metal stripping was performed at a relatively low rate. Figure 36b demonstrates that Na metal crystallizes with the Wulff structure and appears single-crystalline after plating. Upon stripping, a layer-by-layer removal of Na atoms along the $(10\bar{1})$ crystal planes, after which stripping along the $(\bar{1}12)$ planes occurred once the Na

https://doi.org/10.1021/acs.chemrev.4c00507
Chem. Rev. XXXX, XXX, XXX−XXX

extraction reached the corner of the Wulff structure. DFT results suggest that this stripping manner follows the minimum energy barrier during Na removal.[248] Such fascinating results suggest that uniform stripping can be realized when the stripping is slow and the SEI layer is strong and rigid, in this case, as Na_2CO_3. Although the plated Na particles showed a discrepancy with the ones in Figure 36a, possible reasons for the difference include growth rate and CO_2 pressure in the chamber.[247] Regardless, observed phenomena provide important insights regarding the growth behaviors of Na metal in a vacuum and can have profound impacts on Na metal engineering in solid-state Na batteries.

SiN_x-based liquid cells have also been applied to monitor the Na metal nucleation in a liquid environment. Figure 37a shows

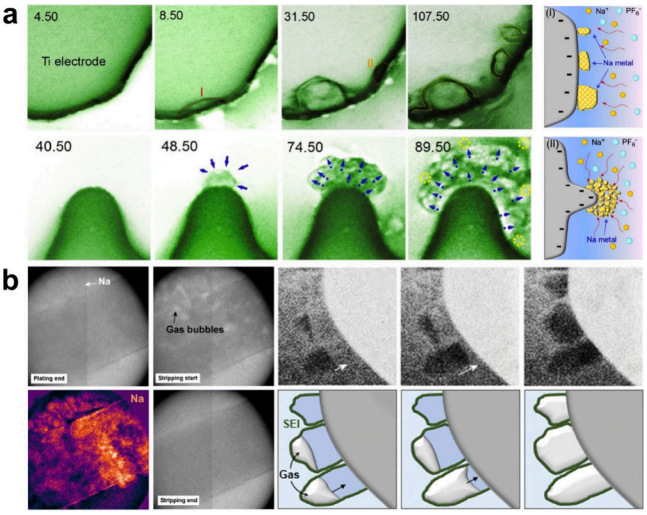

Figure 37. Na metal plating and stripping processes monitored via closed-cell *in situ* TEM. (a) HRTEM images showing different growth modes of Na metal on varying surfaces. Reproduced with permission from ref 249. Copyright 2020 Elsevier Ltd. (b) Gas bubble generation in carbonate electrolyte by HRTEM imaging during Na metal plating and stripping. Reproduced with permission from ref 250. Copyright 2023 Royal Society of Chemistry.

the growth mechanism of Na metal using a liquid electrolyte with 1 M $NaPF_6$ dissolved in PC. Na metal nucleation on a flatter electrode surface appeared more uniform than the nucleation occurring at the curved locations. Na metal at the curved surface experienced much faster growth compared with that on the flat surface. The SEI thickness also appears relatively more uniform in the Na metal grown on flat surface.[249] A model was proposed for these two different modes where electrode roughness plays an important role in regulating grain morphology. Nevertheless, on another note, such drastic differences in growth modes might also be caused by varying local electric fields. The sharp surface tends to generate a stronger electric field that leads to "dendrite-like" nucleation and growth. This work suggests the importance of using a flat current collector for the metal anode.

Gong et al. employed both carbonate-based and ether-based electrolytes in SiN_x-liquid cells to investigate the impact of SEI on Na metal nucleation. Figure 37b demonstrates severe gas bubble formation in carbonate electrolyte. In contrast, no obvious bubbling was observed in the ether electrolyte system. It was further found that a nonuniform SEI formed in a carbonate electrolyte tends to allow gas to enter the empty SEI shell during stripping, which could further lead to the deformation of the SEI in the following cycles. In combination with results from AFM, an ether-based electrolyte produces the SEI with improved uniformity and elasticity, rendering the SEI capable of regulating a uniform Na deposition. Intriguingly, experiments in Figure 37a did not observe as much bubble formation as in this study even though a carbonate electrolyte was used there.[250] The reasons might come from the beam sensitivity of certain solvents and electrical control during the *in situ* experiments. However, both of these have shed light on the growth mechanism of Na metal with various electrode roughness and solvent types in liquid environments, completing the findings in open-cell *in situ* TEM to form a more complete picture of Na metal growth mechanics at the nanoscale.

6.1.2. Na Ion Batteries. Due to the unresolved issues with the Na metal anode, many other anode materials were studied for Na-ion batteries, including hard carbon, alloys, metal oxides, and metal chalcogenides, etc.[251] Here we summarize *in situ* TEM efforts performed on metal alloys, oxides, and chalcogenides for Na-ion batteries in the recent years.

6.1.2.1. Metal Alloy Anodes. Like lithium analogues, Na alloy anodes can theoretically deliver high capacity while most of the alloy anodes go through a drastic volumetric change that reduces cyclability. *In situ* TEM has been employed to study the sodiation mechanism at the nanoscale, enabling the application of proper strategies in electrode engineering.[251,252]

Figure 38a shows the sodiation process of Sn metal using a solid-electrolyte open-cell configuration. The crystalline Sn nanoparticles first form an amorphous Na_xSn phase that is poor in Na content. The amorphous Na_xSn phase was then sodiated to the amorphous Na-rich phase, which eventually formed crystalline $Na_{15}Sn_4$.[253] The final product experienced a volume expansion of 420%, stressingthat essential measures are needed to deal with stress building-up during sodiation of the Na−Sn alloy anode. Another work investigated the sodiation mechanism in amorphous Ge nanowires using open-cell *in situ* TEM (Figure 38b). Amorphous Ge nanowires experienced a volume expansion of 300% and formed an amorphous Li_xGe phase. Intriguingly, during the repeated cycling, pores were found in the desodiated nanowires, which could be then filled up in the subsequent sodiation process.[254] No drastic structural damage was observed after several cycles, highlighting the merits of using amorphous metal alloys to store Na without compromising the structural stability.

Figure 38c demonstrates the discharging process of Bi nanosheets that underwent a multistep sodiation. Pristine hexagonal Bi metal transformed to tetragonal NaBi in the early stage and then became the cubic Na_3Bi phase. Note that the cubic phase is a metastable phase, which turns into a hexagonal Na_3Bi phase as the final product.[255] *In situ* HRTEM clearly captured the step-by-step sodiation of Bi metal and suggested a cubic phase as a buffer phase to mitigate the drastic volume change of the final hexagonal phase.

6.1.2.2. Chalcogenide and Oxide Anodes. Sodium chalcogenides and oxides are also attractive candidates for sodium anode materials. Most of them follow the conversion reaction mechanisms while undergoing large volumetric changes. *In situ* TEM has been applied to understand the detailed sodiation mechanism in these conversion materials.[256−260]

Figure 39a shows the sodiation process of FeS_2 nanoparticles using open-cell configuration. Like most conversion materials,

https://doi.org/10.1021/acs.chemrev.4c00507
Chem. Rev. XXXX, XXX, XXX−XXX

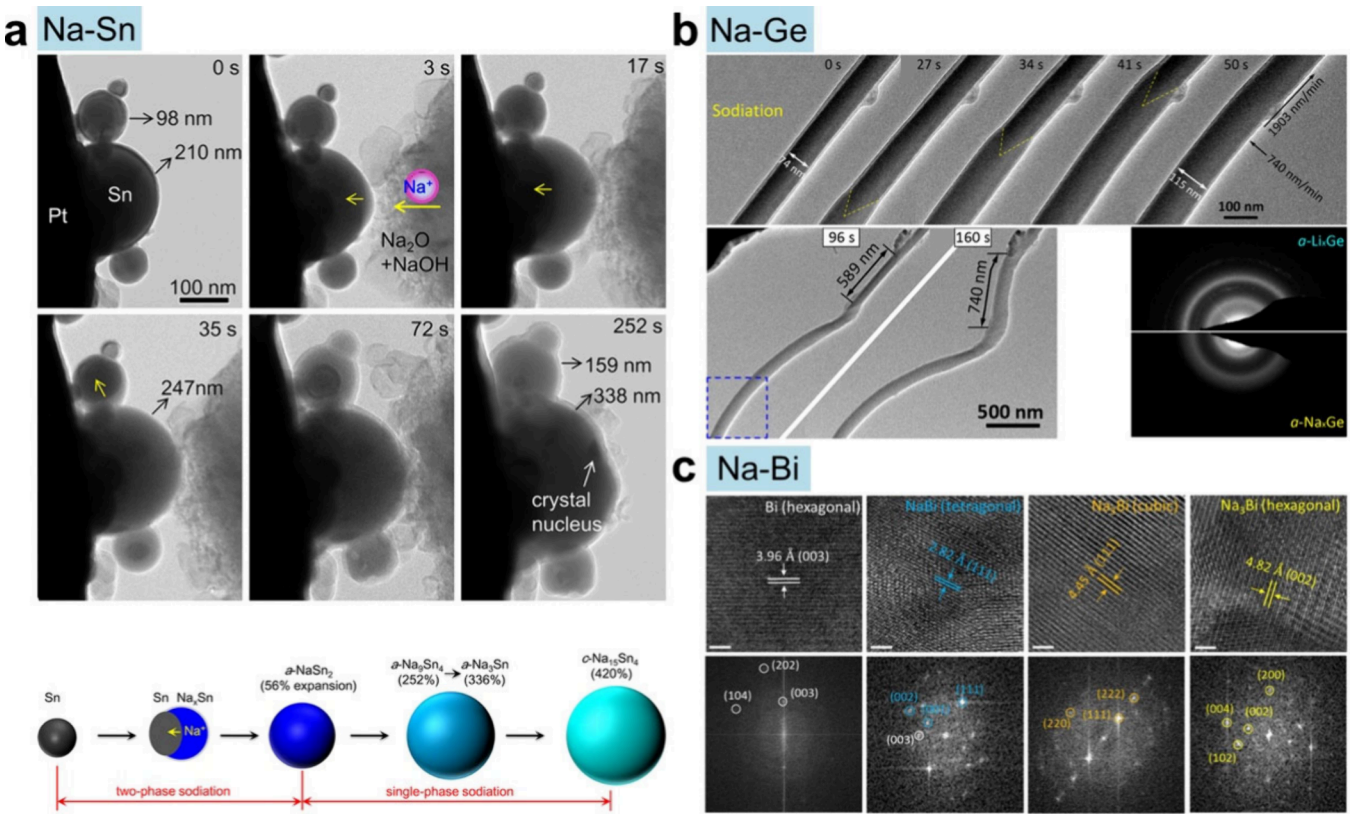

Figure 38. Sodiation process of metal alloy anode materials monitored by open-cell *in situ* TEM. (a) Multiphase sodiation of Na−Sn alloys via HRTEM imaging. Reproduced with permission from ref 253. Copyright 2012 American Chemical Society. (b) Morphological evolution of amorphous Ge NW via HRTEM and SAED analysis. Reproduced with permission from ref 254. Copyright 2016 American Chemical Society. (c) Multistep sodiation process of Na−Bi alloying anodes. Scale bars: 2 nm. Reproduced with permission from ref 255. Copyright 2019 American Chemical Society.

FeS_2 became Na_2S+Fe at the end of the sodiation step along with volume expansion, while $NaFeS_2$ was found as the intermediate phase. Note that a reversible conversion reaction between $NaFeS_2$ and Na_2S+Fe was established in the following cycles.[261] Such direct evidence demonstrates the source for the capacity loss of FeS_2 conversion anode while $NaFeS_2$ can be potentially used as a conversion anode directly. Figure 39b shows an open-cell *in situ* TEM study focusing on Sb_2Se_3 nanowire anode material. Besides volume expansion of the nanowires, Na intercalation occurred first into Sb_2Se_3 nanowires and formed the $Na_xSb_2Se_3$ phase. The conversion reaction then produced Na_2Se and Sb species, after which metallic Sb continued to alloy with Na and eventually formed the Na_3Sb phase.[262] However, Na_2Se+Sb was not desodiated, which was attributed to the major reason for the capacity loss. In another work using $BiSbS_3$ nanorods, a bimetallic sulfide, Fu et al. observed a rather complex sodiation process (Figure 39c). Intercalation first occurred to form BiSb+Na_2S, after which BiSb alloyed further with Na to form Na_2BiSb and then Na_6BiSb as the final product. Surprisingly, Na_6BiSb was recovered to $BiSbS_3$ upon desodiation.[263] Although this bimetallic anode contains heavy transition metal elements, it still delivers a capacity over 700 mAh g^{-1}.

Besides chalcogenides, oxides have also been regarded as candidates for Na-ion battery anodes. Figure 39d illustrates the lithiation process of α-MoO_3 nanobelts. Upon sodiation, α-MoO_3 first forms an amorphous Na_xMoO_3 phase and intermediate crystalline $NaMoO_2$. The final products contained nanocrystalline Mo embedded within a Na_2O matrix, commonly seen in lithium-containing oxide anodes.[264] During subsequent cycles, a reversible transformation between Mo and amorphous Na_2MoO_3 was observed, though with capacity loss due to the irreversible conversion reactions.

In addition, the graphene liquid cell demonstrated a complicated sodiation process of CuS nanoplates inside a liquid electrolyte (Figure 39e). Before the conversion reaction took place, CuS was first sodiated to form three intermediate phases: $Na(CuS)_4$, $Na_7(Cu_6S_5)_2$, and $Na_3(CuS)_4$, whose presence was caused by crystal strain generated during Na-ion intercalation. Eventually, Na_2S+Cu was formed at the end of sodiation.[265] This direct observation of the complex sodiation process highlighted the impact of Na intercalation on crystal structure due to the large ionic radii of Na ions.

6.1.3. Na−S Batteries. Despite its high theoretical capacity, Na−S batteries normally operate at high temperatures (over 300 °C) to keep Na and S at molten states. High-temperature environment cast concerns not only on energy efficiency but also on thermal management system and battery safety. Lowering the operating temperature while delivering high capacity is one of the focuses for Na−S batteries.[229]

By combining a solid-electrolyte open-cell with a heating chip, Li et al. performed *in situ* TEM at 200 °C to investigate the Na−S conversion reaction mechanism (Figure 40a). The S cathode was found to convert to Na_2S or a mixture of Na_2S with polysulfide. By introducing nanovoids inside the S cathode, the integrity of the CNT was maintained during discharging and charging. It was also observed that the S cathode can be reversibly converted between S and Na_2S,

https://doi.org/10.1021/acs.chemrev.4c00507
Chem. Rev. XXXX, XXX, XXX−XXX

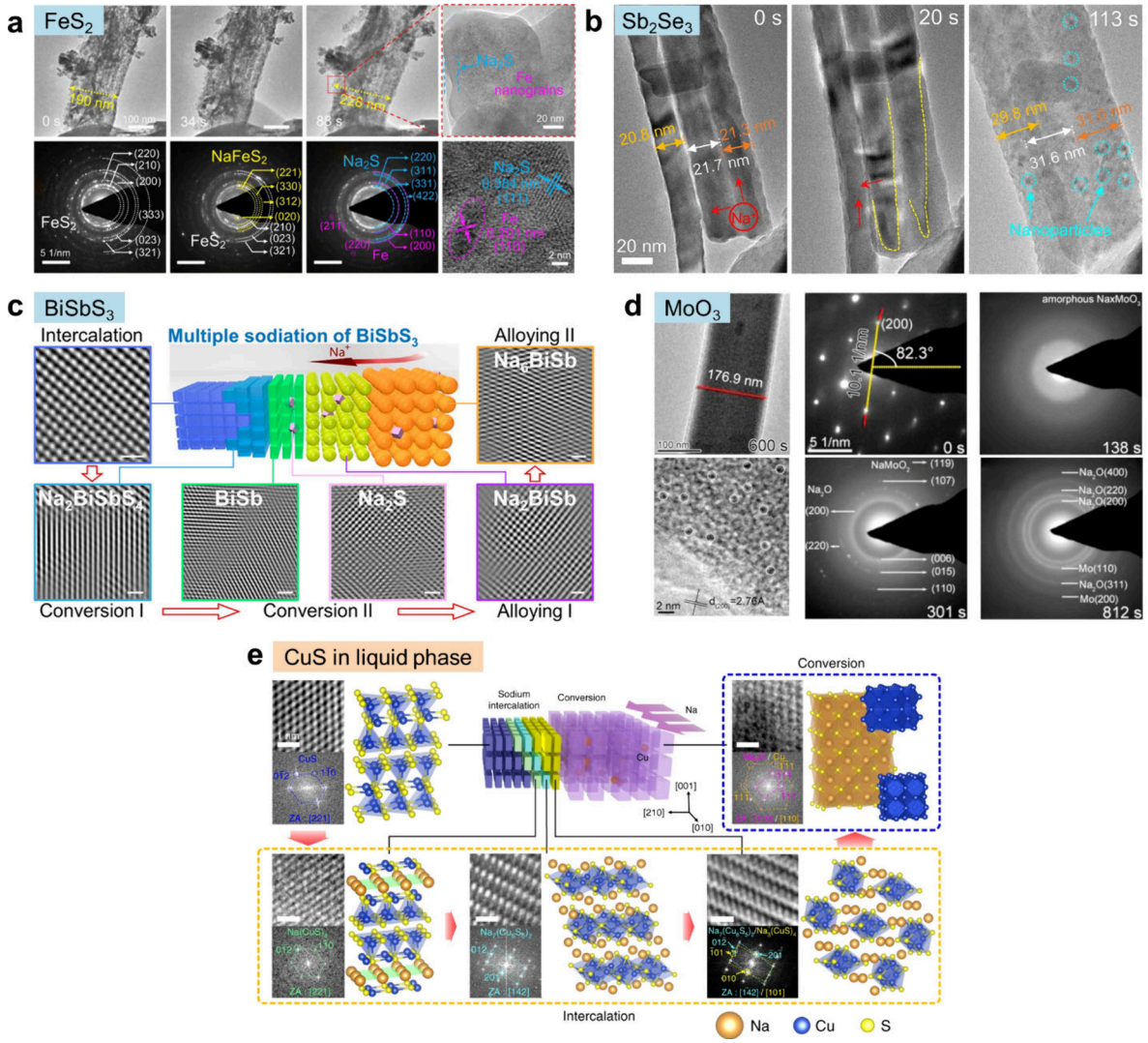

Figure 39. *In situ* TEM studies on the sodiation mechanism of Na chalcogenides and oxides via (a–d) open-cell and (e) closed-cell configurations. (a) HRTEM and SAED analysis on the sodiation process of FeS_2 NW. Reproduced with permission from ref 261. Copyright 2019 Elsevier Ltd. (b) HRTEM images showing the conversion reaction of Sb_2Se_3. Reproduced with permission from ref 262. Copyright 2020 Elsevier Ltd. (c) Multistep sodiation of $BiSbS_3$ through intercalation and conversion reactions unraveled by HRTEM. Reproduced with permission from ref 263. Copyright 2023 American Chemical Society. (d) *In situ* electron diffraction tracking the sodiation process of MoO_3 NW. Reproduced with permission from ref 264. Copyright 2016 Elsevier Ltd. (e) HRTEM images showing a multistep sodiation process of CuS plates probed in liquid-phase TEM. Reproduced with permission from ref 265. Copyright 2018 The Authors.

which can only form Na_2S_2 in a conventional cell operating at 300 °C.[266] By combining the solid electrolyte, CNT, and nanovoid, high utilization of the S cathode and its good reversibility were achieved at a rather low temperature, providing inspiring insights for practical Na–S battery design. Another work employed SeS_2 to further lower the reaction energy barrier of the Na–S battery. Figure 40b demonstrates the sodiation mechanism of SeS_2 inside the CNT. Using a temperature as low as 100 °C, SeS_2 converted to Na_2S without the formation of polysulfides, indicating a much-reduced energy barrier due to the incorporation of Se into the S cathode.[267] Such insights are invaluable for guiding battery engineering at a large scale.

6.1.4. Na–O_2 Batteries. Na–O_2 chemistry takes advantage of elemental abundance, lightweight, and high theoretical capacity, which have been extensively studied. However, it also suffers from high irreversibility, sluggish kinetics, cathode instability, and high polarization. *In situ* TEM was applied to investigate the reaction mechanism at the nanoscale, guiding cell engineering at practical scales.

Figure 41a shows the reaction mechanism of the Na–O_2 battery using a CuS nanowire as the cathode host and catalyst. The detailed analysis demonstrated the formation of NaO_2 that was then disproportionated into Na_2O_2 at the end of sodiation.[268] Another work performed using open-cell configuration illustrates the catalytic effect of single-atom Co (SG-Co) species on Na–O_2 reaction kinetics as shown in Figure 41b. It was observed that a facile formation of Na_2O_2 occurred at SG-Co active sites on a reduced graphene oxide sheet, after which decomposition of Na_2O_2 could also be realized with a low energy barrier.[269] These works stress the essence of catalyst in lowering the reaction barriers for Na–O_2 batteries.[271]

Na–O_2 chemistry was also investigated in an aprotic liquid electrolyte using a SiN_x-based liquid cell. Figure 41c captured the incubation and growth of NaO_2 as the sodiated product

https://doi.org/10.1021/acs.chemrev.4c00507
Chem. Rev. XXXX, XXX, XXX–XXX

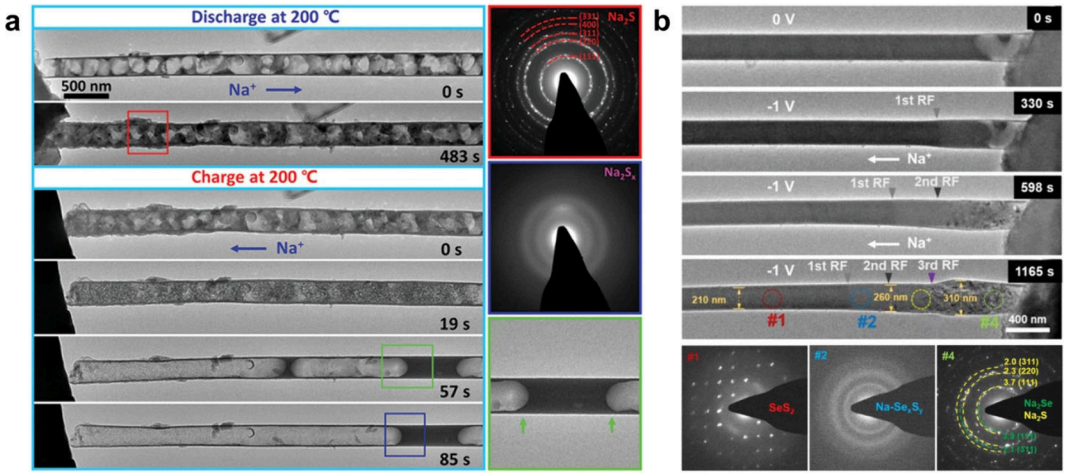

Figure 40. Sodiation mechanism of S cathode at elevated temperature. (a) Morphological and microstructural change during discharging and charging of S cathode at 200 °C. Reproduced with permission from ref 266. Copyright 2021 Wiley-VCH GmbH. (b) Promoted reaction kinetics using SeS_2 cathode for Na−S battery. Reproduced with permission from ref 267. Copyright 2022 The Authors.

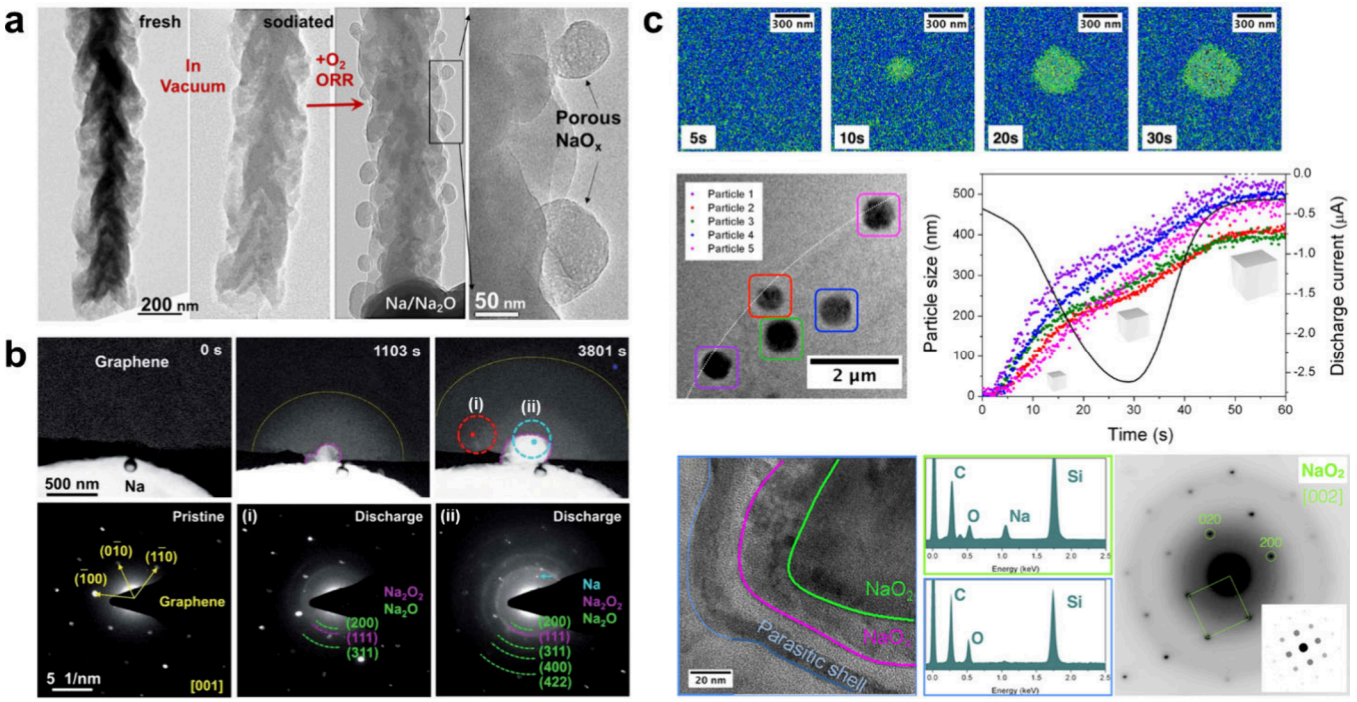

Figure 41. Reaction mechanism of O_2 cathode probed by *in situ* TEM in (a,b) open-cell and (c) closed-cell. (a) CuS-catalyzed Na_2O_2 formation probed by HRTEM images. Reproduced with permission from ref 268. Copyright 2020 American Chemical Society. (b) Facile Na_2O_2 decomposition aided by single-atom Co catalyst. Reproduced with permission from ref 269. Copyright 2021 Royal Society of Chemistry. (c) Reaction pathways of NaO_2 in liquid electrolyte probed by HRTEM and SAED. Reproduced with permission from ref 270. Copyright 2018 American Chemical Society.

through a solution-mediated precipitation process. It was further confirmed that existing NaO_2 particles were susceptible to chemical reactions against the liquid electrolyte and would form a parasitic outer shell, leading to capacity loss.[270] Important insights from this work suggest that the instability between sodiated product and electrolyte is one of the major reasons limiting the cyclability of Na−O_2 batteries.

6.2. Other Battery Chemistries (K, Zn, Mg, and Ca)

In light of the high cost and dwindling supply of lithium resources, alternative metal-ion batteries, including potassium (K), zinc (Zn), magnesium (Mg), and calcium (Ca) ion batteries, have garnered increasing attention as sustainable energy storage solutions besides Na batteries.[272−275] Although their overall operating principles are similar to those of Li/Na batteries, the specific behaviors of these batteries vary according to the physical and chemical properties of each metal species. Therefore, a fundamental understanding of each metal-ion battery is essential for performance optimization. *In situ* TEM has greatly contributed to elucidating the characteristic reaction mechanisms in these battery chemistries.

Arthur et al. studied SEI formation in Mg batteries by using operando XAS and TEM analysis.[278] *In situ* liquid-phase TEM captured SEI layer formation on the surface of Mg metal under

https://doi.org/10.1021/acs.chemrev.4c00507
Chem. Rev. XXXX, XXX, XXX−XXX

a magnesium borohydride. Combined with electrochemical impedance spectroscopy (EIS) and *in situ* XAS analysis, this work demonstrated that the active component responsible for the deposition of Mg metal is a contact-ion pair $[Mg(\mu\text{-}H)_2BH_2]^+$. Moreover, the formation of boron clusters and the release of hydrogen gas were detected during the Mg deposition process, which is crucial for the SEI formation on the surface. The presence of Mg compounds at the interface was also reported by Xu et al. through *in situ* liquid-phase TEM.[276] The authors observed uniform electrodeposition of Mg film without dendritic growth when a constant current of 0.06 mA was applied to a Ti electrode in a magnesium aluminum chloride complex (MACC) electrolyte, as shown in Figure 42a. A similar smooth Mg electrodeposition was also

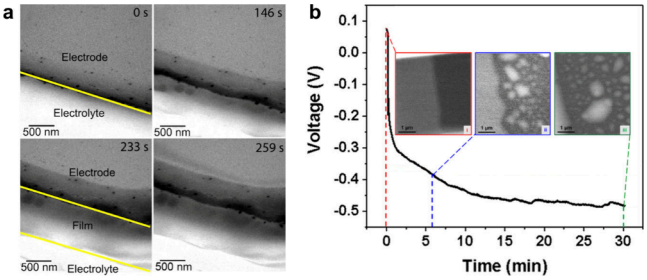

Figure 42. *In situ* liquid-phase TEM investigations of magnesium (Mg) batteries. (a) Uniform Mg film electrodeposition observed in a magnesium aluminum chloride complex (MACC) electrolyte. Reproduced with permission from ref 276. Copyright 2017 The Authors. (b) SEI formation and the subsequent deposition of Mg nanoparticles in Mg monocarborane in tetraglyme (MMC/G4) electrolyte. Reproduced with permission from ref 277. Copyright 2018 American Chemical Society.

observed on an Au electrode, supporting the intrinsic nondendritic nature of Mg electrodeposition. However, the Mg thin film was not electrochemically reversible. *In situ* scanning transmission X-ray microscopy (STXM) and XAS identified the Mg thin film as hexa-coordinated organometallic Mg compounds, which are attributed to the observed nonreversibility. The SEI formation under Mg monocarborane in tetraglyme (MMC/G4) electrolyte and the reversible deposition and dissolution of Mg were also reported by Singh et al.[277] Using *ex situ* and *in situ* liquid-phase TEM experiments, they observed the SEI formation and the subsequent deposition of Mg nanoparticles (Figure 42b). XPS suggested that the SEI resulted from the decomposition of the MMC/G4 electrolyte. In-depth interphase analysis using SEM, XPS, and TEM indicated that the Mg-ion conductive SEI and the subsequent formation of nanocrystalline Mg are critical for the high reversibility of Mg plating and stripping in the MMC/G4 electrolyte system.

In situ TEM research on Zn batteries has been reported by several groups.[279,280,282] Sasaki et al. monitored Zn electrodeposition on a Pt electrode in a 0.1 M $ZnSO_4$ aqueous electrolyte using *in situ* liquid-phase TEM.[279] This work captured the rapid growth of Zn particles with $\{10\bar{1}0\}$ facet planes of hexagonal close-packed (HCP) structure, with only a few seconds after applying a constant current of 4 μA (Figure 43a). Needle-like dendrites grew along the $<11\bar{2}0>$ directions at the hexagonal vertices of the Zn particles, attributed to the higher Zn-ion concentration at these vertices. Additionally, this study unraveled that Zn dendrite stripping proceeds from the

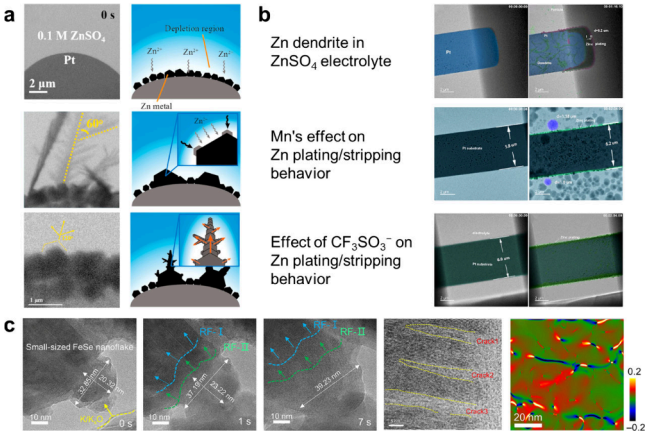

Figure 43. *In situ* TEM investigations of zinc (Zn) and potassium (K) ion batteries. (a) Observation of rapid growth of hexagonal Zn particles followed by needle-like dendrite growth at the particle vertices in Zn batteries with 0.1 M $ZnSO_4$ aqueous electrolyte. Reproduced with permission from ref 279. Copyright 2020 Elsevier B.V. (b) Comparative analysis of Zn plating/stripping behaviors in various electrolytes including $ZnSO_4$, $Zn(CF_3SO_3)_2$, and $ZnSO_4$/$MnSO_4$. Reproduced with permission from ref 280. Copyright 2022 Elsevier B.V. (c) Two-step potassiation reactions of a small-sized FeSe nanoflake anode for K-ion batteries. Reproduced with permission from ref 281. Copyright 2022 The Authors.

root to the tip when the voltage was swept positively. Park et al. investigated the impact of bismuth (Bi) additives on the electrodeposition of a ZnAu alloy on the surface of an Au electrode.[282] The authors observed a delay in Zn dendritic growth and the suppression of hydrogen bubble formation using an electrolyte composed of 0.5 M H_2SO_4 and 0.1 M $ZnSO_4$ with 0.25 mM Bi_2O_3. It was suggested that bismuth could enhance surface diffusion and act as a screening layer, contributing to the uniform deposition of Zn metal. Huang et al. also demonstrated that adding Mn^{2+} or $CF_3SO_3^-$ in aqueous electrolytes can suppress Zn dendritic growth in Zn batteries.[280] *In situ* liquid-phase TEM was applied to investigate Zn plating/stripping behaviors in various electrolytes, including $ZnSO_4$, $Zn(CF_3SO_3)_2$, and $ZnSO_4$/$MnSO_4$ (Figure 43b). In both 2.0 M $ZnSO_4$ and 20 mM $ZnSO_4$ solutions, Zn metal was electrodeposited with a dendritic morphology on Pt substrates. Slow dendritic growth was observed at low concentrations but was not fully suppressed. During the stripping process, Zn did not completely dissolve, leading to the generation of inactive Zn. However, the addition of 5 mM $MnSO_4$ to 20 mM $ZnSO_4$ resulted in the formation of insoluble manganese-based compounds, likely $Mn(OH)_2$, on the electrode surface and in the electrolyte. These particles promoted Zn precipitation by slowing down dendrite formation by mechanically regulating Zn^{2+} flow and creating a uniform Zn-ion field around the electrode. In $Zn(CF_3SO_3)_2$ electrolyte, an electrolyte that exhibits excellent electrochemical performance, Zn metal was plated uniformly with a particle-like morphology, and no H_2 gas evolution was observed. The deposited Zn fully dissolved at the end of the stripping process. MD simulations suggested reduced solvation effects of Zn^{2+} cations in $Zn(CF_3SO_3)_2$ electrolyte, which facilitated Zn^{2+} transportation and charge transfer, leading to dendrite-free Zn electrodeposition.

FeSe materials show promise as an electrode for K batteries. Cai et al. investigated the size-dependent potassiation behavior

https://doi.org/10.1021/acs.chemrev.4c00507
Chem. Rev. XXXX, XXX, XXX−XXX

of FeSe and its stepwise reactions involving intercalation and conversion.[281] Various FeSe nanoflakes with a tetragonal phase were prepared and the potassiation was then observed via *in situ* open-cell TEM. For small (~25 nm) FeSe nanoflakes, two distinct reaction fronts were observed: an initial intercalation reaction and a subsequent conversion reaction. Potassium ion intercalation caused slight contrast changes in the FeSe structure, followed by volume expansion during the conversion reaction as shown in Figure 43c. The intercalation reaction proceeded twice as fast as the conversion reaction, but its rate decreased due to the rapid consumption of potassium by the conversion reaction. Notably, no cracks or pulverization occurred during the volume expansion. In contrast, large (~200 nm) FeSe nanoflakes developed cracks at the reaction boundary along the K-ion diffusion direction. These cracks were attributed to stress accumulation during potassiation, leading to the extension of defects at the interface between FeSe nanoflakes and the potassium source. Additionally, the good electrochemical reversibility of the FeSe anode was demonstrated by observing repetitive volume expansion and contraction through *in situ* TEM.

7. SUMMARY AND OUTLOOK

7.1. Summary and Existing Concerns

By real-time observation of the structural and chemical changes that occur in anodes, cathodes, at interfaces, or in electrolytes during battery operation, *in situ* TEM studies provide critical insights into battery material behaviors and degradation mechanisms relevant to battery performance. As versatile and powerful as *in situ* TEM is, there exist several aspects calling for further attention in the field.

7.1.1. Sample Preparation. Most electrode materials are known for high reactivity and air sensitivity. One of the main tasks during sample preparation is to ensure that samples represent real battery material conditions without introducing artifacts. For *in situ* TEM experiments that utilize Li metal, Na metal, or other reactive materials as electrodes, extra care is needed to minimize the impact of ambient air and moisture during sample preparation. A good practice is to employ glovebox or customized argon-flowing glove bags when mounting reactive materials onto the sample platform and when transferring TEM holders into the microscope. Such measures largely mitigate the side reactions that could alter sample intrinsic properties.

7.1.2. Sample Configuration. There often exist concerns from the battery community on *in situ* TEM results due to the significant differences between TEM sample configuration and actual battery cells/electrodes. For instance, during an open-cell *in situ* TEM experiment, the reaction pathway of 1D nanowires is confined along the longitudinal direction due to limited contact between the nanowire and the electrolyte, unlike the electrolyte-surrounding environment in real battery cells. Similarly, in the closed-cell TEM configuration, the lack of external pressure on the side-by-side electrodes on the chip is in sharp contrast with pressurized practical batteries. The discrepancies from *in situ* TEM setups may lead to unknown impact in observed reaction behaviors that obscures data interpretation. While such *in situ* TEM sample configurations were designed to achieve electron transparency and electrical control of battery materials, further research is needed to refine sample configurations to better emulate actual battery operating conditions.

7.1.3. Electrical Control. As *in situ* TEM observation of battery materials is driven by electrochemical stimuli, precise electrical control is required. The observed dynamic phenomena of battery materials should be correlated with electrochemical responses on the potentiostat. In other words, a good understanding of the electrochemistry in studying battery system is needed to fully comprehend the as-seen phenomena on samples. However, it has been found in the literature that the electrical input signal may not be suitable for their systems, or it is uncertain whether the output electrical response corresponds to observed changes under TEM. It is noted that for the same material system or sample setup, constant current control or constant voltage control can activate vastly different electrochemical behaviors in materials. Especially when under electron beam irradiation, sample behaviors tend to be unpredictable, where electrochemistry ought to be a good reference to rationalize the observed phenomena.

7.1.4. Beam Control. Except for being air-sensitive, most battery materials are also extremely electron-beam-sensitive. The electron beam irradiation may introduce beam-induced structural or chemical changes that alter the intrinsic properties of the battery materials. Controlling electron dose rate and total dosage is essential for *in situ* TEM studies. It is always good practice to find the electron beam intensity threshold for the battery materials under investigation before diving into actual measurements so that beam damage can be largely minimized during analysis.

On the other hand, battery material synthesis efforts ought to align with the nature of TEM studies. Since *in situ* TEM serves as a localized characterization tool, the observed phenomena usually require statistics for validation. The conclusions drawn from *in situ* TEM measurement call for improved material quality control, where more engineering efforts might be needed from the battery community, along with the continuous enhancement of *in situ* TEM techniques.

7.2. Outlook

Over the past decades, the demands for the challenging characterization of battery materials have in turn promoted renovations in TEM technologies. The noteworthy developments include cryogenic protection, 4D-STEM and iDPC, etc. The cryo-TEM toolset was originally developed in the structural biology field and was then incorporated by the battery researchers to mitigate the beam damage on electrodes and associated interfaces since 2017.[283,284] Cryogenic protection helps to preserve the pristine state of reacted battery samples.[285] 4D-STEM utilizes a pixelated electron detector to capture a two-dimensional convergent beam electron diffraction pattern at each scan location as the beam rasters across a two-dimensional image in real space. It has demonstrated the unique capabilities in phase identification, strain mapping, fast electron detection and charge density mapping of battery materials.[197,286] iDPC is a STEM method based on the measurement of the deflection of electron beam using a segmented detector, which can not only simultaneously image both light and heavy elements, such as lithium and oxygen atoms in lithium cathode materials, but also enables low-dose imaging.[286−288] All these attributes are essential for characterizing battery materials.

Development of advanced *in situ* TEM techniques with both open-cell and closed-cell configurations, coupling with aforementioned cutting-edge TEM techniques, granted

https://doi.org/10.1021/acs.chemrev.4c00507
Chem. Rev. XXXX, XXX, XXX−XXX

researcher powerful tools to access more invaluable information hidden in the sample and data sets. A few future directions for *in situ* TEM advancement are listed below.

7.2.1. Sample Platform. The common sample platforms used in closed cells and open cells were initially developed 20 years ago. Over this period, variant cell designs have emerged, but the research field is still open for future breakthroughs. For closed cells, the key improvement will be achieving higher spatial resolution. By engineering the SiN_x liquid cell, it was shown that high- resolution imaging of lithium polysulfide precipitation could be captured;[47] In a very recent work, a customized liquid cell design leveraging thin polymer membranes and interdigital electrodes was able to obtain atomic resolution of Cu during electrocatalytic reactions with *in situ* TEM.[58] Such designs of sample platforms are inspiring for battery research as they can potentially resolve the long-lasting drawback of liquid cells and provide more detailed information during electrochemical processes.

7.2.2. Data Interpretation. New TEM capabilities such as fast electron detection helps capture the transient phenomena during rapid chemical/electrochemical reactions. However, huge data sets collected from such an imaging capability could easily overwhelm researchers and lead to discrepancies during analysis. Additionally, due to the need for low-dose imaging, image contrast appears weak most of the time. Developing robust methods for analyzing and interpreting the vast amounts of data is urgently needed for the *in situ* TEM studies. The machine-learning approach should be employed to address large data set and potential biases or misinterpretations that can arise from the complexity of *in situ* measurements.[285] Examples include the classification of different diffraction patterns collected via 4D-STEM, where unsupervised learning was used to cluster the intensity curves with various characteristics and helped define the best way to categorize the collected pattern or spectra.[29] With the increased computing power nowadays, machine learning is anticipated to be part of routine procedures during *in situ* TEM data analysis.

7.2.3. Cryogenic Capability. The alternative good way to alleviate beam damage on the sample during *in situ* operation is to apply cryogenic protection. As cryogenic TEM has proven effective in preserving beam-sensitive materials, the cryogenic capability would be an invaluable attribute to add to the current *in situ* TEM technologies. The TEM holder that is capable of applying electrical stimuli and cooling down the sample platform at the same time can be one of the priorities for future development. Although lithium transport in low temperature liquid electrolytes would be largely suppressed, the cryogenic capability or variable subzero low temperature control may slow down the sample kinetics and might provide unprecedented insights that will be otherwise missed.

7.2.4. Correlative Characterization. Another future direction ties in the integration of *in situ* TEM and other characterization methods. The ability to analyze the same sample location and observe electrochemical changes at multiple length scales, from millimeters down to angstroms, using multiple characterization methods through imaging and spectroscopy will be the ultimate goal of failure analysis for battery systems.

In situ TEM has undoubtedly accelerated the exploration of battery materials in all branches of battery research, offering unparalleled insights into the fundamental processes. In the decades to come, mutual progress should be seen when the continuous innovation of *in situ* TEM techniques keeps pushing the boundaries of battery research.

AUTHOR INFORMATION

Corresponding Authors

Seung-Yong Lee − *Division of Materials Science and Engineering and Department of Battery Engineering, Hanyang University, Seoul 04763, Republic of Korea*; Email: syonglee@hanyang.ac.kr

Haimei Zheng − *Materials Sciences Division, Lawrence Berkeley National Laboratory, Berkeley, California 94720, United States; Department of Materials Science and Engineering, University of California, Berkeley, California 94720, United States*; orcid.org/0000-0003-3813-4170; Email: hmzheng@lbl.gov

Authors

Diyi Cheng − *Materials Sciences Division, Lawrence Berkeley National Laboratory, Berkeley, California 94720, United States*; orcid.org/0000-0003-1616-9209

Jinseok Hong − *Division of Materials Science and Engineering, Hanyang University, Seoul 04763, Republic of Korea*

Daewon Lee − *Materials Sciences Division, Lawrence Berkeley National Laboratory, Berkeley, California 94720, United States; Department of Materials Science and Engineering, University of California, Berkeley, California 94720, United States*

Complete contact information is available at: https://pubs.acs.org/10.1021/acs.chemrev.4c00507

Author Contributions

D.C., S.-Y.L., and H.Z. conceived the outline of the manuscript. D.C., J.H., and D.L. performed literature search and prepared the figures. D.L. refined the figure collages. D.C., J.H., S.-Y.L., and H.Z. cowrote the manuscript. All authors discussed the content and commented on the manuscript. All authors have approved the final manuscript. CRediT: **Diyi Cheng** conceptualization, data curation, project administration, resources, visualization, writing - original draft, writing - review & editing; **Jinseok Hong** resources, software, validation, writing - original draft; **Daewon Lee** resources, software, validation, visualization; **Seung-Yong Lee** conceptualization, project administration, supervision, validation, writing - original draft, writing - review & editing.

Notes

The authors declare no competing financial interest.

Biographies

Diyi Cheng is currently a postdoctoral fellow at Lawrence Berkeley National Laboratory. He received his Ph.D. in Materials Science and Engineering at the University of California, San Diego, in 2023. He received his B.S. in Materials Physics at Jilin University in 2017. His research interests include advanced electron microscopy, *in situ* characterizations, lithium metal thin-film batteries, solid−solid interfaces, metal nucleation, etc.

Jinseok Hong is an integrated M.S./Ph.D. student under the supervision of Professor Seung-Yong Lee in the Division of Materials Science and Engineering at Hanyang University, South Korea. He received his B.S. in Chemical Engineering at Hanbat National University in 2022. His research interests focus on *in situ* transmission

https://doi.org/10.1021/acs.chemrev.4c00507
Chem. Rev. XXXX, XXX, XXX−XXX

electron microscopy to investigate the electrochemical reaction mechanisms of lithium-ion battery cathode materials.

Daewon Lee is a doctoral candidate at the University of California, Berkeley. He earned his B.S. and M.S. degrees in Materials Science and Engineering from the Korea Advanced Institute of Science and Technology (KAIST) in 2014 and 2016, respectively. After graduating from KAIST, he fulfilled his mandatory military service by working as a research scientist at the Carbon Resources Institute within the Korea Research Institute of Chemical Technology (KRICT) from 2016 to 2019. His research focuses on *in situ* liquid-phase transmission electron microscopy for atomic scale understanding of phase transformations in nanocrystals.

Seung-Yong Lee is an assistant professor in the Division of Materials Science and Engineering at Hanyang University, South Korea. He earned his B.S. and Ph.D. in Materials Science and Engineering from Seoul National University in 2012 and 2017, respectively. From 2018 to 2020, he worked as a postdoctoral researcher at Lawrence Berkeley National Laboratory. His current research focuses on *in situ* and *ex situ* electron microscopy to explore the electrochemical reaction mechanisms of applied nanomaterials. He is particularly interested in next-generation anode and cathode materials for secondary batteries, including Li/Na batteries, and also conducts research on electronic materials for memory devices.

Haimei Zheng is a senior scientist in the Materials Sciences Division at the Lawrence Berkeley National Laboratory (LBNL) and an adjunct professor in the Department of Materials Science and Engineering at the University of California, Berkeley. She received her Ph.D. degree from the University of Maryland, College Park, and did postdoctoral research at LBNL and the Department of Chemistry at the University of California, Berkeley. In 2010, she started her independent research group at LBNL. Her research interests broadly focus on the physical and chemical processes of materials, with a focus on nanoscale materials transformations and dynamic phenomena at solid−liquid interfaces including those in batteries and electrocatalysis, through developing and applying *in situ* liquid-phase transmission electron microscopy.

ACKNOWLEDGMENTS

This work was supported by the U.S. Department of Energy, Office of Science, Office of Basic Energy Sciences (BES), Materials Sciences and Engineering Division under Award Number DE-AC02-05-CH11231 within the *in situ* TEM program (KC22ZH). D.C. thanks the support by the U.S. Department of Energy, Office of Science, Office of Basic Energy Sciences, Materials Sciences and Engineering Division under contract no. DE-AC02-05-CH11231 (D2S2 program, KCD2S2). D.L. acknowledges the Kwanjeong Study Abroad Scholarship from the KEF (Kwanjeong Educational Foundation) (KEF-2019). J.H. and S.-Y.L. were supported by the National Research Foundation of Korea (NRF) grant funded by the Korea government (MSIT) (no. RS-2023-00222411, RS-2024-00406724, and NRF-2022R1C1C1010157). We thank Zilai Feng for the help with the schematic drawing in Figure 1.

REFERENCES

(1) Volta, A.; Banks, J. I. On the electricity excited by the mere contact of conducting substances of different kinds. *Philos. Mag.* **1800**, *7*, 289−311.

(2) Leblanc-Soreau, A.; Danot, M.; Trichet, L.; Rouxel, J. Les intercalaires Ax Ti S_2 et Ax Zr S_2. Structure et liaisons. (A = Li, Na, K, Rb, Cs). *Mater. Res. Bull.* **1974**, *9*, 191−197.

(3) Haering, R. R.; Stiles, J. A. R. Electrical Storage Device. U. S. Patent 4,233,377A, 1978.

(4) Goodenough, J. B.; Mizushima, K.; Wiseman, P. J. Electrochemical cell and method of making ion conductors for said cell. European Patent EP0017400B1, 1984.

(5) Yazami, R.; Touzain, P. A reversible graphite-lithium negative electrode for electrochemical generators. *J. Power Sources* **1983**, *9*, 365−371.

(6) Thackeray, M. M.; Johnson, P. J.; de Picciotto, L. A.; Bruce, P. G.; Goodenough, J. B. Electrochemical extraction of lithium from $LiMn_2O_4$. *Mater. Res. Bull.* **1984**, *19*, 179−187.

(7) Padhi, A. K.; Nanjundaswamy, K. S.; Goodenough, J. B. Phospho-olivines as Positive-Electrode Materials for Rechargeable Lithium Batteries. *J. Electrochem. Soc.* **1997**, *144*, 1188−1194.

(8) Delmas, C.; Saadoune, I. Electrochemical and physical properties of the $Li_xNi_{1-y}Co_yO_2$ phases. *Solid State Ion.* **1992**, *53*−*56*, 370−375.

(9) Gao, Y.; Myrtle, K.; Zhang, M.; Reimers, J. N.; Dahn, J. R. Valence band of $LiNi_xMn_{2-x}O_4$ and its effects on the voltage profiles of $LiNi_xMn_{2-x}O_4$/Li electrochemical cells. *Phys. Rev. B* **1996**, *54*, 16670−16675.

(10) Lee, Y.-G.; Fujiki, S.; Jung, C.; Suzuki, N.; Yashiro, N.; Omoda, R.; Ko, D.-S.; Shiratsuchi, T.; Sugimoto, T.; Ryu, S.; et al. High-energy long-cycling all-solid-state lithium metal batteries enabled by silver−carbon composite anodes. *Nat. Energy* **2020**, *5*, 299−308.

(11) Kim, J. G.; Son, B.; Mukherjee, S.; Schuppert, N.; Bates, A.; Kwon, O.; Choi, M. J.; Chung, H. Y.; Park, S. A review of lithium and non-lithium based solid state batteries. *J. Power Sources* **2015**, *282*, 299−322.

(12) Zhu, Y.; He, X.; Mo, Y. Origin of Outstanding Stability in the Lithium Solid Electrolyte Materials: Insights from Thermodynamic Analyses Based on First-Principles Calculations. *ACS Appl. Mater. Interfaces* **2015**, *7*, 23685−23693.

(13) Li, J.-Y.; Xu, Q.; Li, G.; Yin, Y.-X.; Wan, L.-J.; Guo, Y.-G. Research progress regarding Si-based anode materials towards practical application in high energy density Li-ion batteries. *Mater. Chem. Front.* **2017**, *1*, 1691−1708.

(14) Kasemchainan, J.; Zekoll, S.; Spencer Jolly, D.; Ning, Z.; Hartley, G. O.; Marrow, J.; Bruce, P. G. Critical stripping current leads to dendrite formation on plating in lithium anode solid electrolyte cells. *Nat. Mater.* **2019**, *18*, 1105−1111.

(15) Li, J.; Dudney, N. J.; Nanda, J.; Liang, C. Artificial Solid Electrolyte Interphase To Address the Electrochemical Degradation of Silicon Electrodes. *ACS Appl. Mater. Interfaces* **2014**, *6*, 10083−10088.

(16) Lin, D.; Liu, Y.; Li, Y.; Li, Y.; Pei, A.; Xie, J.; Huang, W.; Cui, Y. Fast galvanic lithium corrosion involving a Kirkendall-type mechanism. *Nat. Chem.* **2019**, *11*, 382−389.

(17) Lin, D.; Liu, Y.; Cui, Y. Reviving the lithium metal anode for high-energy batteries. *Nat. Nanotechnol.* **2017**, *12*, 194−206.

(18) Rustomji, C. S.; Yang, Y.; Kim, T. K.; Mac, J.; Kim, Y. J.; Caldwell, E.; Chung, H.; Meng, Y. S. Liquefied gas electrolytes for electrochemical energy storage devices. *Science* **2017**, *356*, eaal4263.

(19) Liu, J.; Bao, Z.; Cui, Y.; Dufek, E. J.; Goodenough, J. B.; Khalifah, P.; Li, Q.; Liaw, B. Y.; Liu, P.; Manthiram, A.; et al. Pathways for practical high-energy long-cycling lithium metal batteries. *Nat. Energy* **2019**, *4*, 180−186.

(20) Cao, X.; Ren, X.; Zou, L.; Engelhard, M. H.; Huang, W.; Wang, H.; Matthews, B. E.; Lee, H.; Niu, C.; Arey, B. W.; et al. Monolithic solid−electrolyte interphases formed in fluorinated orthoformate-based electrolytes minimize Li depletion and pulverization. *Nat. Energy* **2019**, *4*, 796−805.

(21) Yang, Y.; Davies, D. M.; Yin, Y.; Borodin, O.; Lee, J. Z.; Fang, C.; Olguin, M.; Zhang, Y.; Sablina, E. S.; Wang, X.; et al. High-Efficiency Lithium-Metal Anode Enabled by Liquefied Gas Electrolytes. *Joule* **2019**, *3*, 1986−2000.

(22) Hobold, G. M.; Lopez, J.; Guo, R.; Minafra, N.; Banerjee, A.; Shirley Meng, Y.; Shao-Horn, Y.; Gallant, B. M. Moving beyond 99.9% Coulombic efficiency for lithium anodes in liquid electrolytes. *Nat. Energy* **2021**, *6*, 951−960.

https://doi.org/10.1021/acs.chemrev.4c00507
Chem. Rev. XXXX, XXX, XXX−XXX

(23) Knoll, M.; Ruska, E. Beitrag zur geometrischen Elektronenoptik. I. *Ann. Phys.* **1932**, *404*, 607−640.
(24) Kalinin, S. V.; Ophus, C.; Voyles, P. M.; Erni, R.; Kepaptsoglou, D.; Grillo, V.; Lupini, A. R.; Oxley, M. P.; Schwenker, E.; Chan, M. K. Y.; et al. Machine learning in scanning transmission electron microscopy. *Nat. Rev. Methods Primers* **2022**, *2*, 11.
(25) Lovejoy, T. C.; Ramasse, Q. M.; Falke, M.; Kaeppel, A.; Terborg, R.; Zan, R.; Dellby, N.; Krivanek, O. L. Single atom identification by energy dispersive x-ray spectroscopy. *Appl. Phys. Lett.* **2012**, *100*, 154101.
(26) Lin, Y.; Zhou, M.; Tai, X.; Li, H.; Han, X.; Yu, J. Analytical transmission electron microscopy for emerging advanced materials. *Matter* **2021**, *4*, 2309−2339.
(27) Crozier, P. A. Vibrational and valence aloof beam EELS: A potential tool for nondestructive characterization of nanoparticle surfaces. *Ultramicroscopy* **2017**, *180*, 104−114.
(28) Bustillo, K. C.; Zeltmann, S. E.; Chen, M.; Donohue, J.; Ciston, J.; Ophus, C.; Minor, A. M. 4D-STEM of Beam-Sensitive Materials. *Acc. Chem. Res.* **2021**, *54*, 2543−2551.
(29) Xie, Y. J.; Wang, J. Y.; Savitzky, B. H.; Chen, Z.; Wang, Y.; Betzler, S.; Bustillo, K.; Persson, K.; Cui, Y.; Wang, L. W.; et al. Spatially resolved structural order in low-temperature liquid electrolyte. *Sci. Adv.* **2023**, *9*, eadc9721.
(30) Wang, H.; Liu, L.; Wang, J.; Li, C.; Hou, J.; Zheng, K. The Development of iDPC-STEM and Its Application in Electron Beam Sensitive Materials. *Molecules* **2022**, *27*, 3829.
(31) https://web.archive.org/web/20160304224245/http:/www.sonyenergy-devices.co.jp/en/keyword/#anchor01 (accessed July 5, 2024).
(32) Freitas, B.; Siqueira, J., Jr.; da Costa, L.; Ferreira, G.; Resende, J. Synthesis and Characterization of $LiCoO_2$ from Different Precursors by Sol-Gel Method. *J. Braz. Chem. Soc.* **2017**, *28*, 2254−2266.
(33) Ruska, E. Beitrag zur übermikroskopischen Abbildung bei höheren Drucken. *Kolloid-Z.* **1942**, *100*, 212−219.
(34) Abrams, I. M.; McBain, J. W. A Closed Cell for Electron Microscopy. *J. Appl. Phys.* **1944**, *15*, 607−609.
(35) Blech, I. A.; Meieran, E. S. DIRECT TRANSMISSION ELECTRON MICROSCOPE OBSERVATION OF ELECTROTRANSPORT IN ALUMINUM THIN FILMS. *Appl. Phys. Lett.* **1967**, *11*, 263−266.
(36) Williamson, M. J.; Tromp, R. M.; Vereecken, P. M.; Hull, R.; Ross, F. M. Dynamic microscopy of nanoscale cluster growth at the solid−liquid interface. *Nat. Mater.* **2003**, *2*, 532−536.
(37) Huang, J. Y.; Zhong, L.; Wang, C. M.; Sullivan, J. P.; Xu, W.; Zhang, L. Q.; Mao, S. X.; Hudak, N. S.; Liu, X. H.; Subramanian, A.; et al. In Situ Observation of the Electrochemical Lithiation of a Single SnO_2 Nanowire Electrode. *Science* **2010**, *330*, 1515−1520.
(38) Yamamoto, K.; Iriyama, Y.; Asaka, T.; Hirayama, T.; Fujita, H.; Fisher, C. A. J.; Nonaka, K.; Sugita, Y.; Ogumi, Z. Dynamic Visualization of the Electric Potential in an All-Solid-State Rechargeable Lithium Battery. *Angew. Chem., Int. Ed.* **2010**, *49*, 4414−4417.
(39) Mai, L.; Dong, Y.; Xu, L.; Han, C. Single Nanowire Electrochemical Devices. *Nano Lett.* **2010**, *10*, 4273−4278.
(40) Gu, M.; Parent, L. R.; Mehdi, B. L.; Unocic, R. R.; McDowell, M. T.; Sacci, R. L.; Xu, W.; Connell, J. G.; Xu, P.; Abellan, P.; et al. Demonstration of an Electrochemical Liquid Cell for Operando Transmission Electron Microscopy Observation of the Lithiation/Delithiation Behavior of Si Nanowire Battery Anodes. *Nano Lett.* **2013**, *13*, 6106−6112.
(41) Zeng, Z.; Liang, W. I.; Liao, H. G.; Xin, H. L.; Chu, Y. H.; Zheng, H. Visualization of Electrode−Electrolyte Interfaces in $LiPF_6$/EC/DEC Electrolyte for Lithium Ion Batteries via in Situ TEM. *Nano Lett.* **2014**, *14*, 1745−1750.
(42) Yuk, J. M.; Seo, H. K.; Choi, J. W.; Lee, J. Y. Anisotropic Lithiation Onset in Silicon Nanoparticle Anode Revealed by in Situ Graphene Liquid Cell Electron Microscopy. *ACS Nano* **2014**, *8*, 7478−7485.
(43) Lee, S.-Y.; Shangguan, J.; Alvarado, J.; Betzler, S.; Harris, S. J.; Doeff, M. M.; Zheng, H. Unveiling the mechanisms of lithium dendrite suppression by cationic polymer film induced solid−electrolyte interphase modification. *Energy Environ. Sci.* **2020**, *13*, 1832−1842.
(44) Liu, X.; Garcia-Mendez, R.; Lupini, A. R.; Cheng, Y.; Hood, Z. D.; Han, F.; Sharafi, A.; Idrobo, J. C.; Dudney, N. J.; Wang, C.; et al. Local electronic structure variation resulting in Li 'filament' formation within solid electrolytes. *Nat. Mater.* **2021**, *20*, 1485−1490.
(45) Su, L.; Ren, J.; Lu, T.; Chen, K.; Ouyang, J.; Zhang, Y.; Zhu, X.; Wang, L.; Min, H.; Luo, W.; et al. Deciphering Structural Origins of Highly Reversible Lithium Storage in High Entropy Oxides with In Situ Transmission Electron Microscopy. *Adv. Mater.* **2023**, *35*, 2205751.
(46) Xu, Y.; Jia, H.; Gao, P.; Galvez-Aranda, D. E.; Beltran, S. P.; Cao, X.; Le, P. M. L.; Liu, J.; Engelhard, M. H.; Li, S.; et al. Direct in situ measurements of electrical properties of solid−electrolyte interphase on lithium metal anodes. *Nat. Energy* **2023**, *8*, 1345−1354.
(47) Zhou, S.; Shi, J.; Liu, S.; Li, G.; Pei, F.; Chen, Y.; Deng, J.; Zheng, Q.; Li, J.; Zhao, C.; et al. Visualizing interfacial collective reaction behaviour of Li−S batteries. *Nature* **2023**, *621*, 75−81.
(48) Wang, F.; Yu, H. C.; Chen, M. H.; Wu, L.; Pereira, N.; Thornton, K.; Van der Ven, A.; Zhu, Y.; Amatucci, G. G.; Graetz, J. Tracking lithium transport and electrochemical reactions in nanoparticles. *Nat. Commun.* **2012**, *3*, 1201.
(49) Yang, Z.; Ong, P. V.; He, Y.; Wang, L.; Bowden, M. E.; Xu, W.; Droubay, T. C.; Wang, C.; Sushko, P. V.; Du, Y. Direct Visualization of Li Dendrite Effect on LiCoO2 Cathode by In Situ TEM. *Small* **2018**, *14*, 1803108.
(50) Ma, C.; Cheng, Y.; Yin, K.; Luo, J.; Sharafi, A.; Sakamoto, J.; Li, J.; More, K. L.; Dudney, N. J.; Chi, M. Interfacial Stability of Li Metal−Solid Electrolyte Elucidated via in Situ Electron Microscopy. *Nano Lett.* **2016**, *16*, 7030−7036.
(51) Hammad Fawey, M.; Chakravadhanula, V. S. K.; Reddy, M. A.; Rongeat, C.; Scherer, T.; Hahn, H.; Fichtner, M.; Kübel, C. In situ TEM studies of micron-sized all-solid-state fluoride ion batteries: Preparation, prospects, and challenges. *Microsc. Res. Technol.* **2016**, *79*, 615−624.
(52) Hirayama, T.; Aizawa, Y.; Yamamoto, K.; Sato, T.; Murata, H.; Yoshida, R.; Fisher, C. A. J.; Kato, T.; Iriyama, Y. Advanced electron holography techniques for in situ observation of solid-state lithium ion conductors. *Ultramicroscopy* **2017**, *176*, 86−92.
(53) Lee, J. Z.; Wynn, T. A.; Meng, Y. S.; Santhanagopalan, D. Focused Ion Beam Fabrication of LiPON-based Solid-state Lithium-ion Nanobatteries for In Situ Testing. *J. Vis. Exp.* **2018**, e56259.
(54) Zheng, H.; Smith, R. K.; Jun, Y.-w.; Kisielowski, C.; Dahmen, U.; Alivisatos, A. P. Observation of Single Colloidal Platinum Nanocrystal Growth Trajectories. *Science* **2009**, *324*, 1309−1312.
(55) Mirsaidov, U.; Patterson, J. P.; Zheng, H. Liquid phase transmission electron microscopy for imaging of nanoscale processes in solution. *MRS Bull.* **2020**, *45*, 704−712.
(56) Zheng, W.; Lee, D.; Zheng, H. Strategies to overcome electron-beam issues in liquid phase TEM: Study of chemical processes. *MRS Bull.* **2024**, *49*, 205−213.
(57) de Jonge, N.; Ross, F. M. Electron microscopy of specimens in liquid. *Nat. Nanotechnol.* **2011**, *6*, 695−704.
(58) Zhang, Q.; Song, Z.; Sun, X.; Liu, Y.; Wan, J.; Betzler, S. B.; Zheng, Q.; Shangguan, J.; Bustillo, K. C.; Ercius, P.; et al. Atomic dynamics of electrified solid−liquid interfaces in liquid-cell TEM. *Nature* **2024**, *630*, 643−647.
(59) Yuk, J. M.; Park, J.; Ercius, P.; Kim, K.; Hellebusch, D. J.; Crommie, M. F.; Lee, J. Y.; Zettl, A.; Alivisatos, A. P. High-Resolution EM of Colloidal Nanocrystal Growth Using Graphene Liquid Cells. *Science* **2012**, *336*, 61−64.
(60) Zhu, C.; Liang, S.; Song, E.; Zhou, Y.; Wang, W.; Shan, F.; Shi, Y.; Hao, C.; Yin, K.; Zhang, T.; et al. In-situ liquid cell transmission electron microscopy investigation on oriented attachment of gold nanoparticles. *Nat. Commun.* **2018**, *9*, 421.

https://doi.org/10.1021/acs.chemrev.4c00507
Chem. Rev. XXXX, XXX, XXX−XXX

(61) Yang, J.; Choi, M. K.; Sheng, Y.; Jung, J.; Bustillo, K.; Chen, T.; Lee, S.-W.; Ercius, P.; Kim, J. H.; Warner, J. H.; et al. MoS_2 Liquid Cell Electron Microscopy Through Clean and Fast Polymer-Free MoS_2 Transfer. *Nano Lett.* **2019**, *19*, 1788−1795.
(62) Jokisaari, J. R.; Hachtel, J. A.; Hu, X.; Mukherjee, A.; Wang, C.; Konecna, A.; Lovejoy, T. C.; Dellby, N.; Aizpurua, J.; Krivanek, O. L.; et al. Vibrational Spectroscopy of Water with High Spatial Resolution. *Adv. Mater.* **2018**, *30*, 1802702.
(63) Jonge, N. d.; Peckys, D. B.; Kremers, G. J.; Piston, D. W. Electron microscopy of whole cells in liquid with nanometer resolution. *Proc. Natl. Acad. Sci. U. S. A.* **2009**, *106*, 2159−2164.
(64) Peng, X.; Shangguan, J.; Zhang, Q.; Hauwiller, M.; Yu, H.; Nie, Y.; Bustillo, K. C.; Alivisatos, A. P.; Asta, M.; Zheng, H. Unveiling Corrosion Pathways of Sn Nanocrystals through High-Resolution Liquid Cell Electron Microscopy. *Nano Lett.* **2024**, *24*, 1168−1175.
(65) Noh, N.; Park, J.; Park, J. S.; Koo, K.; Park, J. Y.; Yuk, J. M. Lithographically patterned well-type graphene liquid cells with rational designs. *Lab Chip* **2020**, *20*, 2796−2803.
(66) Chang, J. H.; Cheong, J. Y.; Yuk, J. M.; Kim, C.; Kim, S. J.; Seo, H. K.; Kim, I. D.; Lee, J. Y. Direct Realization of Complete Conversion and Agglomeration Dynamics of SnO_2 Nanoparticles in Liquid Electrolyte. *ACS Omega* **2017**, *2*, 6329−6336.
(67) Kuhne, M.; Borrnert, F.; Fecher, S.; Ghorbani-Asl, M.; Biskupek, J.; Samuelis, D.; Krasheninnikov, A. V.; Kaiser, U.; Smet, J. H. Reversible superdense ordering of lithium between two graphene sheets. *Nature* **2018**, *564*, 234−239.
(68) Xu, Z.-L.; Kim, S. J.; Chang, D.; Park, K.-Y.; Dae, K. S.; Dao, K. P.; Yuk, J. M.; Kang, K. Visualization of regulated nucleation and growth of lithium sulfides for high energy lithium sulfur batteries. *Energy Environ. Sci.* **2019**, *12*, 3144−3155.
(69) Tan, D. H. S.; Chen, Y.-T.; Yang, H.; Bao, W.; Sreenarayanan, B.; Doux, J.-M.; Li, W.; Lu, B.; Ham, S.-Y.; Sayahpour, B.; et al. Carbon-free high-loading silicon anodes enabled by sulfide solid electrolytes. *Science* **2021**, *373*, 1494−1499.
(70) Chen, W.; Salvatierra, R. V.; Ren, M.; Chen, J.; Stanford, M. G.; Tour, J. M. Laser-Induced Silicon Oxide for Anode-Free Lithium Metal Batteries. *Adv. Mater.* **2020**, *32*, 2002850.
(71) Huang, W.; Wang, J.; Braun, M. R.; Zhang, Z.; Li, Y.; Boyle, D. T.; McIntyre, P. C.; Cui, Y. Dynamic Structure and Chemistry of the Silicon Solid-Electrolyte Interphase Visualized by Cryogenic Electron Microscopy. *Matter* **2019**, *1*, 1232−1245.
(72) Cao, X.; Jia, H.; Xu, W.; Zhang, J.-G. Review—Localized High-Concentration Electrolytes for Lithium Batteries. *J. Electrochem. Soc.* **2021**, *168*, No. 010522.
(73) Santhanagopalan, D.; Qian, D.; McGilvray, T.; Wang, Z.; Wang, F.; Camino, F.; Graetz, J.; Dudney, N.; Meng, Y. S. Interface Limited Lithium Transport in Solid-State Batteries. *J. Phys. Chem. Lett.* **2014**, *5*, 298−303.
(74) Nanda, J.; Yang, G.; Hou, T.; Voylov, D. N.; Li, X.; Ruther, R. E.; Naguib, M.; Persson, K.; Veith, G. M.; Sokolov, A. P. Unraveling the Nanoscale Heterogeneity of Solid Electrolyte Interphase Using Tip-Enhanced Raman Spectroscopy. *Joule* **2019**, *3*, 2001−2019.
(75) Mukanova, A.; Jetybayeva, A.; Myung, S.-T.; Kim, S.-S.; Bakenov, Z. A mini-review on the development of Si-based thin film anodes for Li-ion batteries. *Mater. Today Energy* **2018**, *9*, 49−66.
(76) Bai, S.; Bao, W.; Qian, K.; Han, B.; Li, W.; Sayahpour, B.; Sreenarayanan, B.; Tan, D. H. S.; Ham, S.-y.; Meng, Y. S. Elucidating the Role of Prelithiation in Si-based Anodes for Interface Stabilization. *Adv. Energy Mater.* **2023**, *13*, 2301041.
(77) Bao, W.; Fang, C.; Cheng, D.; Zhang, Y.; Lu, B.; Tan, D. H. S.; Shimizu, R.; Sreenarayanan, B.; Bai, S.; Li, W.; et al. Quantifying lithium loss in amorphous silicon thin-film anodes via titration-gas chromatography. *Cell Rep. Phys. Sci.* **2021**, *2*, 100597.
(78) Liu, X. H.; Wang, J. W.; Huang, S.; Fan, F.; Huang, X.; Liu, Y.; Krylyuk, S.; Yoo, J.; Dayeh, S. A.; Davydov, A. V.; et al. In situ atomic-scale imaging of electrochemical lithiation in silicon. *Nat. Nanotechnol.* **2012**, *7*, 749−756.
(79) Wang, C. M.; Li, X.; Wang, Z.; Xu, W.; Liu, J.; Gao, F.; Kovarik, L.; Zhang, J. G.; Howe, J.; Burton, D. J.; et al. In Situ TEM Investigation of Congruent Phase Transition and Structural Evolution of Nanostructured Silicon/Carbon Anode for Lithium Ion Batteries. *Nano Lett.* **2012**, *12*, 1624−1632.
(80) McDowell, M. T.; Lee, S. W.; Harris, J. T.; Korgel, B. A.; Wang, C.; Nix, W. D.; Cui, Y. In Situ TEM of Two-Phase Lithiation of Amorphous Silicon Nanospheres. *Nano Lett.* **2013**, *13*, 758−764.
(81) Gu, M.; Wang, Z.; Connell, J. G.; Perea, D. E.; Lauhon, L. J.; Gao, F.; Wang, C. Electronic Origin for the Phase Transition from Amorphous LixSi to Crystalline Li15Si4. *ACS Nano* **2013**, *7*, 6303−6309.
(82) Liu, X. H.; Zhong, L.; Huang, S.; Mao, S. X.; Zhu, T.; Huang, J. Y. Size-Dependent Fracture of Silicon Nanoparticles During Lithiation. *ACS Nano* **2012**, *6*, 1522−1531.
(83) McDowell, M. T.; Ryu, I.; Lee, S. W.; Wang, C.; Nix, W. D.; Cui, Y. Studying the Kinetics of Crystalline Silicon Nanoparticle Lithiation with In Situ Transmission Electron Microscopy. *Adv. Mater.* **2012**, *24*, 6034−6041.
(84) Adkins, E. R.; Jiang, T.; Luo, L.; Wang, C.-M.; Korgel, B. A. In Situ Transmission Electron Microsopy of Oxide Shell-Induced Pore Formation in (De)lithiated Silicon Nanowires. *ACS Energy Lett.* **2018**, *3*, 2829−2834.
(85) Gu, M.; Li, Y.; Li, X.; Hu, S.; Zhang, X.; Xu, W.; Thevuthasan, S.; Baer, D. R.; Zhang, J.-G.; Liu, J.; et al. In Situ TEM Study of Lithiation Behavior of Silicon Nanoparticles Attached to and Embedded in a Carbon Matrix. *ACS Nano* **2012**, *6*, 8439−8447.
(86) Zhang, Y.; Li, Y.; Wang, Z.; Zhao, K. Lithiation of SiO_2 in Li-Ion Batteries: In Situ Transmission Electron Microscopy Experiments and Theoretical Studies. *Nano Lett.* **2014**, *14*, 7161−7170.
(87) Liu, X. H.; Zhang, L. Q.; Zhong, L.; Liu, Y.; Zheng, H.; Wang, J. W.; Cho, J. H.; Dayeh, S. A.; Picraux, S. T.; Sullivan, J. P.; et al. Ultrafast Electrochemical Lithiation of Individual Si Nanowire Anodes. *Nano Lett.* **2011**, *11*, 2251−2258.
(88) He, Y.; Piper, D. M.; Gu, M.; Travis, J. J.; George, S. M.; Lee, S.-H.; Genc, A.; Pullan, L.; Liu, J.; Mao, S. X.; et al. In Situ Transmission Electron Microscopy Probing of Native Oxide and Artificial Layers on Silicon Nanoparticles for Lithium Ion Batteries. *ACS Nano* **2014**, *8*, 11816−11823.
(89) Shen, C.; Ge, M.; Luo, L.; Fang, X.; Liu, Y.; Zhang, A.; Rong, J.; Wang, C.; Zhou, C. In Situ and Ex Situ TEM Study of Lithiation Behaviours of Porous Silicon Nanostructures. *Sci. Rep.* **2016**, *6*, 31334.
(90) Bai, P.; Li, J.; Brushett, F. R.; Bazant, M. Z. Transition of lithium growth mechanisms in liquid electrolytes. *Energy Environ. Sci.* **2016**, *9*, 3221−3229.
(91) Yamaki, J.; Tobishima, S.; Hayashi, K.; Saito, K.; Nemoto, Y.; Arakawa, M. A consideration of the morphology of electrochemically deposited lithium in an organic electrolyte. *J. Power Sources* **1998**, *74*, 219−227.
(92) Besenhard, J. O.; Wagner, M. W.; Winter, M.; Jannakoudakis, A. D.; Jannakoudakis, P. D.; Theodoridou, E. Inorganic film-forming electrolyte additives improving the cycling behaviour of metallic lithium electrodes and the self-discharge of carbon—lithium electrodes. *J. Power Sources* **1993**, *44*, 413−420.
(93) Ferrese, A.; Newman, J. Mechanical Deformation of a Lithium-Metal Anode Due to a Very Stiff Separator. *J. Electrochem. Soc.* **2014**, *161*, A1350−A1359.
(94) Kim, J.; Kim, M.; Kim, M.; Hong, J.; Moon, S. W.; Yu, S. H.; Lee, S. Y. A Stepped Mesh Host for Lithium Metal Batteries Inspired by Transmission Electron Microscopy Sampling Grids. *Electron. Mater. Lett.* **2024**, *20*, 767−774.
(95) Jiang, Y.; Wang, B.; Liu, P.; Wang, B.; Zhou, Y.; Wang, D.; Liu, H.; Dou, S. Modified solid-electrolyte interphase toward stable Li metal anode. *Nano Energy* **2020**, *77*, 105308.
(96) Sacci, R. L.; Dudney, N. J.; More, K. L.; Parent, L. R.; Arslan, I.; Browning, N. D.; Unocic, R. R. Direct visualization of initial SEI morphology and growth kinetics during lithium deposition by in situ electrochemical transmission electron microscopy. *Chem. Commun.* **2014**, *50*, 2104−2107.
(97) Mehdi, B. L.; Qian, J.; Nasybulin, E.; Park, C.; Welch, D. A.; Faller, R.; Mehta, H.; Henderson, W. A.; Xu, W.; Wang, C. M.; et al.

https://doi.org/10.1021/acs.chemrev.4c00507
Chem. Rev. XXXX, XXX, XXX−XXX

Observation and Quantification of Nanoscale Processes in Lithium Batteries by Operando Electrochemical (S)TEM. *Nano Lett.* **2015**, *15*, 2168−2173.
(98) Sacci, R. L.; Black, J. M.; Balke, N.; Dudney, N. J.; More, K. L.; Unocic, R. R. Nanoscale Imaging of Fundamental Li Battery Chemistry: Solid-Electrolyte Interphase Formation and Preferential Growth of Lithium Metal Nanoclusters. *Nano Lett.* **2015**, *15*, 2011−2018.
(99) Dachraoui, W.; Pauer, R.; Battaglia, C.; Erni, R. Operando Electrochemical Liquid Cell Scanning Transmission Electron Microscopy Investigation of the Growth and Evolution of the Mosaic Solid Electrolyte Interphase for Lithium-Ion Batteries. *ACS Nano* **2023**, *17*, 20434−20444.
(100) Kushima, A.; So, K. P.; Su, C.; Bai, P.; Kuriyama, N.; Maebashi, T.; Fujiwara, Y.; Bazant, M. Z.; Li, J. Liquid cell transmission electron microscopy observation of lithium metal growth and dissolution: Root growth, dead lithium and lithium flotsams. *Nano Energy* **2017**, *32*, 271−279.
(101) Leenheer, A. J.; Jungjohann, K. L.; Zavadil, K. R.; Sullivan, J. P.; Harris, C. T. Lithium Electrodeposition Dynamics in Aprotic Electrolyte Observed in Situvia Transmission Electron Microscopy. *ACS Nano* **2015**, *9*, 4379−4389.
(102) Sand, H. J. S., III On the concentration at the electrodes in a solution, with special reference to the liberation of hydrogen by electrolysis of a mixture of copper sulphate and sulphuric acid. *London Edinburgh Philos. Mag. & J. Sci.* **1901**, *1*, 45−79.
(103) Rosso, M.; Gobron, T.; Brissot, C.; Chazalviel, J. N.; Lascaud, S. Onset of dendritic growth in lithium/polymer cells. *J. Power Sources* **2001**, *97*−*98*, 804−806.
(104) Arakawa, M.; Tobishima, S.; Nemoto, Y.; Ichimura, M.; Yamaki, J. Lithium electrode cycleability and morphology dependence on current density. *J. Power Sources* **1993**, *43*, 27−35.
(105) Crowther, O.; West, A. C. Effect of electrolyte composition on lithium dendrite growth. *J. Electrochem. Soc.* **2008**, *155*, A806−A811.
(106) Harrison, K. L.; Zavadil, K. R.; Hahn, N. T.; Meng, X.; Elam, J. W.; Leenheer, A.; Zhang, J. G.; Jungjohann, K. L. Lithium Self-Discharge and Its Prevention: Direct Visualization through In Situ Electrochemical Scanning Transmission Electron Microscopy. *ACS Nano* **2017**, *11*, 11194−11205.
(107) Lee, S.-Y.; Shangguan, J.; Betzler, S.; Harris, S. J.; Doeff, M. M.; Zheng, H. Lithium metal stripping mechanisms revealed through electrochemical liquid cell electron microscopy. *Nano Energy* **2022**, *102*, 107641.
(108) Gong, C.; Pu, S. D.; Gao, X.; Yang, S.; Liu, J.; Ning, Z.; Rees, G. J.; Capone, I.; Pi, L.; Liu, B.; et al. Revealing the Role of Fluoride-Rich Battery Electrode Interphases by Operando Transmission Electron Microscopy. *Adv. Energy Mater.* **2021**, *11*, 2003118.
(109) Mehdi, B. L.; Stevens, A.; Qian, J.; Park, C.; Xu, W.; Henderson, W. A.; Zhang, J. G.; Mueller, K. T.; Browning, N. D. The Impact of Li Grain Size on Coulombic Efficiency in Li Batteries. *Sci. Rep.* **2016**, *6*, 34267.
(110) Park, H.; Jeon, Y.; Chung, W. J.; Bae, Y.; Kim, J.; Baek, H.; Park, J. Early Stage Li Plating by Liquid Phase and Cryogenic Transmission Electron Microscopy. *ACS Energy Lett.* **2023**, *8*, 715−721.
(111) Zhang, X. Q.; Cheng, X. B.; Chen, X.; Yan, C.; Zhang, Q. Fluoroethylene Carbonate Additives to Render Uniform Li Deposits in Lithium Metal Batteries. *Adv. Funct. Mater.* **2017**, *27*, 1605989.
(112) Suo, L. M.; Xue, W. J.; Gobet, M.; Greenbaum, S. G.; Wang, C.; Chen, Y. M.; Yang, W. L.; Li, Y. X.; Li, J. Fluorine-donating electrolytes enable highly reversible 5-V-class Li metal batteries. *Proc. Natl. Acad. Sci. U. S. A.* **2018**, *115*, 1156−1161.
(113) Weber, R.; Genovese, M.; Louli, A. J.; Hames, S.; Martin, C.; Hill, I. G.; Dahn, J. R. Long cycle life and dendrite-free lithium morphology in anode-free lithium pouch cells enabled by a dual-salt liquid electrolyte. *Nat. Energy* **2019**, *4*, 683−689.
(114) Qian, J.; Xu, W.; Bhattacharya, P.; Engelhard, M.; Henderson, W. A.; Zhang, Y.; Zhang, J.-G. Dendrite-free Li deposition using trace-amounts of water as an electrolyte additive. *Nano Energy* **2015**, *15*, 135−144.
(115) Zheng, G.; Lee, S. W.; Liang, Z.; Lee, H.-W.; Yan, K.; Yao, H.; Wang, H.; Li, W.; Chu, S.; Cui, Y. Interconnected hollow carbon nanospheres for stable lithium metal anodes. *Nat. Nanotechnol.* **2014**, *9*, 618−623.
(116) Wang, C.; Wang, H.; Tao, L.; Wang, X.; Cao, P.; Lin, F.; Xin, H. L. Direct Observation of Nucleation and Growth Behaviors of Lithium by In Situ Electron Microscopy. *ACS Energy Lett.* **2023**, *8*, 1929−1935.
(117) Chen, Y.; Wang, Z.; Li, X.; Yao, X.; Wang, C.; Li, Y.; Xue, W.; Yu, D.; Kim, S. Y.; Yang, F.; et al. Li metal deposition and stripping in a solid-state battery via Coble creep. *Nature* **2020**, *578*, 251−255.
(118) Sun, J.; Cheng, Y.; Zhang, H.; Yan, X.; Sun, Z.; Ye, W.; Li, W.; Zhang, M.; Gao, H.; Han, J.; et al. Enhanced Cyclability of Lithium Metal Anodes Enabled by Anti-aggregation of Lithiophilic Seeds. *Nano Lett.* **2022**, *22*, 5874−5882.
(119) He, Y.; Ren, X.; Xu, Y.; Engelhard, M. H.; Li, X.; Xiao, J.; Liu, J.; Zhang, J. G.; Xu, W.; Wang, C. Origin of lithium whisker formation and growth under stress. *Nat. Nanotechnol.* **2019**, *14*, 1042−1047.
(120) Zhang, L.; Yang, T.; Du, C.; Liu, Q.; Tang, Y.; Zhao, J.; Wang, B.; Chen, T.; Sun, Y.; Jia, P.; et al. Lithium whisker growth and stress generation in an in situ atomic force microscope−environmental transmission electron microscope set-up. *Nat. Nanotechnol.* **2020**, *15*, 94−98.
(121) Wang, C. Y.; Lin, R. Q.; He, Y. B.; Zou, P. C.; Kisslinger, K.; He, Q.; Li, J.; Xin, H. L. L. Tension-Induced Cavitation in Li-Metal Stripping. *Adv. Mater.* **2023**, *35*, 2209091.
(122) Yang, T.; Li, H.; Tang, Y.; Chen, J.; Ye, H.; Wang, B.; Zhang, Y.; Du, C.; Yao, J.; Guo, B.; et al. In situ observation of cracking and self-healing of solid electrolyte interphases during lithium deposition. *Sci. Bull.* **2021**, *66*, 1754−1763.
(123) Kaskhedikar, N. A.; Maier, J. Lithium Storage in Carbon Nanostructures. *Adv. Mater.* **2009**, *21*, 2664−2680.
(124) Sun, Y.; Wu, Q.; Shi, G. Graphene based new energy materials. *Energy Environ. Sci.* **2011**, *4*, 1113−1132.
(125) Meyer, J. C.; Eder, F.; Kurasch, S.; Skakalova, V.; Kotakoski, J.; Park, H. J.; Roth, S.; Chuvilin, A.; Eyhusen, S.; Benner, G.; et al. Accurate Measurement of Electron Beam Induced Displacement Cross Sections for Single-Layer Graphene. *Phys. Rev. Lett.* **2012**, *108*, 196102.
(126) Unocic, R. R.; Sun, X. G.; Sacci, R. L.; Adamczyk, L. A.; Alsem, D. H.; Dai, S.; Dudney, N. J.; More, K. L. Direct Visualization of Solid Electrolyte Interphase Formation in Lithium-Ion Batteries with In Situ Electrochemical Transmission Electron Microscopy. *Microsc. Microanal.* **2014**, *20*, 1029−1037.
(127) Dong, J.; Xue, Y.; Zhang, C.; Weng, Q.; Dai, P.; Yang, Y.; Zhou, M.; Li, C.; Cui, Q.; Kang, X.; et al. Improved Li^+ Storage through Homogeneous N-Doping within Highly Branched Tubular Graphitic Foam. *Adv. Mater.* **2017**, *29*, 1603692.
(128) Liu, Y.; Zheng, H.; Liu, X. H.; Huang, S.; Zhu, T.; Wang, J. W.; Kushima, A.; Hudak, N. S.; Huang, X.; Zhang, S. L.; et al. Lithiation-Induced Embrittlement of Multiwalled Carbon Nanotubes. *ACS Nano* **2011**, *5*, 7245−7253.
(129) Liu, X. H.; Wang, J. W.; Liu, Y.; Zheng, H.; Kushima, A.; Huang, S.; Zhu, T.; Mao, S. X.; Li, J.; Zhang, S.; et al. In situ transmission electron microscopy of electrochemical lithiation, delithiation and deformation of individual graphene nanoribbons. *Carbon* **2012**, *50*, 3836−3844.
(130) Liu, X. H.; Huang, S.; Picraux, S. T.; Li, J.; Zhu, T.; Huang, J. Y. Reversible Nanopore Formation in Ge Nanowires during Lithiation−Delithiation Cycling: An In Situ Transmission Electron Microscopy Study. *Nano Lett.* **2011**, *11*, 3991−3997.
(131) Liu, X. H.; Zheng, H.; Zhong, L.; Huang, S.; Karki, K.; Zhang, L. Q.; Liu, Y.; Kushima, A.; Liang, W. T.; Wang, J. W.; et al. Anisotropic Swelling and Fracture of Silicon Nanowires during Lithiation. *Nano Lett.* **2011**, *11*, 3312−3318.
(132) Liu, Y.; Liu, X. H.; Nguyen, B.-M.; Yoo, J.; Sullivan, J. P.; Picraux, S. T.; Huang, J. Y.; Dayeh, S. A. Tailoring Lithiation Behavior

https://doi.org/10.1021/acs.chemrev.4c00507
Chem. Rev. XXXX, XXX, XXX−XXX

by Interface and Bandgap Engineering at the Nanoscale. *Nano Lett.* **2013**, *13*, 4876−4883.
(133) Liang, W.; Yang, H.; Fan, F.; Liu, Y.; Liu, X. H.; Huang, J. Y.; Zhu, T.; Zhang, S. Tough Germanium Nanoparticles under Electrochemical Cycling. *ACS Nano* **2013**, *7*, 3427−3433.
(134) Lu, X.; He, Y.; Mao, S. X.; Wang, C.-m.; Korgel, B. A. Size Dependent Pore Formation in Germanium Nanowires Undergoing Reversible Delithiation Observed by In Situ TEM. *J. Phys. Chem. C* **2016**, *120*, 28825−28831.
(135) Boebinger, M. G.; Yarema, O.; Yarema, M.; Unocic, K. A.; Unocic, R. R.; Wood, V.; McDowell, M. T. Spontaneous and reversible hollowing of alloy anode nanocrystals for stable battery cycling. *Nat. Nanotechnol.* **2020**, *15*, 475−481.
(136) Xia, W.; Zhang, Q.; Xu, F.; Ma, H.; Chen, J.; Qasim, K.; Ge, B.; Zhu, C.; Sun, L. Visualizing the Electrochemical Lithiation/Delithiation Behaviors of Black Phosphorus by in Situ Transmission Electron Microscopy. *J. Phys. Chem. C* **2016**, *120*, 5861−5868.
(137) Liu, Y.; Hudak, N. S.; Huber, D. L.; Limmer, S. J.; Sullivan, J. P.; Huang, J. Y. In Situ Transmission Electron Microscopy Observation of Pulverization of Aluminum Nanowires and Evolution of the Thin Surface Al_2O_3 Layers during Lithiation−Delithiation Cycles. *Nano Lett.* **2011**, *11*, 4188−4194.
(138) Gu, M.; Yang, H.; Perea, D. E.; Zhang, J.-G.; Zhang, S.; Wang, C.-M. Bending-Induced Symmetry Breaking of Lithiation in Germanium Nanowires. *Nano Lett.* **2014**, *14*, 4622−4627.
(139) Gan, Z.; Gu, M.; Tang, J.; Wang, C.-Y.; He, Y.; Wang, K. L.; Wang, C.; Smith, D. J.; McCartney, M. R. Direct Mapping of Charge Distribution during Lithiation of Ge Nanowires Using Off-Axis Electron Holography. *Nano Lett.* **2016**, *16*, 3748−3753.
(140) Liu, N.; Lu, Z.; Zhao, J.; McDowell, M. T.; Lee, H.-W.; Zhao, W.; Cui, Y. A pomegranate-inspired nanoscale design for large-volume-change lithium battery anodes. *Nat. Nanotechnol.* **2014**, *9*, 187−192.
(141) Wu, H.; Chan, G.; Choi, J. W.; Ryu, I.; Yao, Y.; McDowell, M. T.; Lee, S. W.; Jackson, A.; Yang, Y.; Hu, L.; et al. Stable cycling of double-walled silicon nanotube battery anodes through solid−electrolyte interphase control. *Nat. Nanotechnol.* **2012**, *7*, 310−315.
(142) Liu, N.; Wu, H.; McDowell, M. T.; Yao, Y.; Wang, C.; Cui, Y. A Yolk-Shell Design for Stabilized and Scalable Li-Ion Battery Alloy Anodes. *Nano Lett.* **2012**, *12*, 3315−3321.
(143) Jung, S. C.; Han, Y.-K. Thermodynamic and Kinetic Origins of Lithiation-Induced Amorphous-to-Crystalline Phase Transition of Phosphorus. *J. Phys. Chem. C* **2015**, *119*, 12130−12137.
(144) Ma, W.; Wang, Y.; Yang, Y.; Wang, X.; Yuan, Z.; Liu, X.; Ding, Y. Temperature-Dependent Li Storage Performance in Nanoporous Cu−Ge−Al Alloy. *ACS Appl. Mater. Interfaces* **2019**, *11*, 9073−9082.
(145) Zeng, Z.; Liang, W. I.; Chu, Y. H.; Zheng, H. In situ TEM study of the Li−Au reaction in an electrochemical liquid cell. *Faraday Discuss.* **2014**, *176*, 95−107.
(146) Leenheer, A. J.; Jungjohann, K. L.; Zavadil, K. R.; Harris, C. T. Phase Boundary Propagation in Li-Alloying Battery Electrodes Revealed by Liquid-Cell Transmission Electron Microscopy. *ACS Nano* **2016**, *10*, 5670−5678.
(147) Hou, C.; Han, J.; Liu, P.; Yang, C.; Huang, G.; Fujita, T.; Hirata, A.; Chen, M. Operando Observations of SEI Film Evolution by Mass-Sensitive Scanning Transmission Electron Microscopy. *Adv. Energy Mater.* **2019**, *9*, 1902675.
(148) Poizot, P.; Laruelle, S.; Grugeon, S.; Dupont, L.; Tarascon, J. M. Nano-sized transition-metal oxides as negative-electrode materials for lithium-ion batteries. *Nature* **2000**, *407*, 496−499.
(149) Zhang, L. Q.; Liu, X. H.; Liu, Y.; Huang, S.; Zhu, T.; Gui, L.; Mao, S. X.; Ye, Z. Z.; Wang, C. M.; Sullivan, J. P.; et al. Controlling the Lithiation-Induced Strain and Charging Rate in Nanowire Electrodes by Coating. *ACS Nano* **2011**, *5*, 4800−4809.
(150) Nie, A.; Gan, L.-Y.; Cheng, Y.; Asayesh-Ardakani, H.; Li, Q.; Dong, C.; Tao, R.; Mashayek, F.; Wang, H.-T.; Schwingenschlögl, U.; et al. Atomic-Scale Observation of Lithiation Reaction Front in Nanoscale SnO_2 Materials. *ACS Nano* **2013**, *7*, 6203−6211.
(151) Wang, C.-M.; Xu, W.; Liu, J.; Zhang, J. G.; Saraf, L. V.; Arey, B. W.; Choi, D.; Yang, Z. G.; Xiao, J.; Thevuthasan, S.; et al. In Situ Transmission Electron Microscopy Observation of Microstructure and Phase Evolution in a SnO_2 Nanowire during Lithium Intercalation. *Nano Lett.* **2011**, *11*, 1874−1880.
(152) Wen, Y.; Zhu, M.; Song, S.; Xin, L.; Xiong, Y.; Li, J.; Shen, Y.; Yin, K.; Sun, L. In situ TEM investigation of large crystal formation in lithiated SnO_2 anode assisted by electron beam irradiation. *J. Mater. Chem. A* **2021**, *9*, 22301−22312.
(153) Seo, H. K.; Park, J. Y.; Chang, J. H.; Dae, K. S.; Noh, M. S.; Kim, S. S.; Kang, C. Y.; Zhao, K.; Kim, S.; Yuk, J. M. Strong stress-composition coupling in lithium alloy nanoparticles. *Nat. Commun.* **2019**, *10*, 3428.
(154) Cheong, J. Y.; Chang, J. H.; Kim, S. J.; Kim, C.; Seo, H. K.; Shin, J. W.; Yuk, J. M.; Lee, J. Y.; Kim, I. D. In Situ High-Resolution Transmission Electron Microscopy (TEM) Observation of Sn Nanoparticles on SnO_2 Nanotubes Under Lithiation. *Microsc. Microanal.* **2017**, *23*, 1107−1115.
(155) Cheong, J. Y.; Chang, J. H.; Seo, H. K.; Yuk, J. M.; Shin, J. W.; Lee, J. Y.; Kim, I.-D. Growth dynamics of solid electrolyte interphase layer on SnO_2 nanotubes realized by graphene liquid cell electron microscopy. *Nano Energy* **2016**, *25*, 154−160.
(156) Cheong, J. Y.; Chang, J. H.; Kim, C.; Mweta, F. J.; Jung, J.-W.; Lee, J. Y.; Kim, I.-D. Revisiting on the effect and role of TiO_2 layer thickness on SnO_2 for enhanced electrochemical performance for lithium-ion batteries. *Electrochim. Acta* **2017**, *258*, 1140−1148.
(157) Lee, K.; Shin, S.; Degen, T.; Lee, W.; Yoon, Y. S. In situ analysis of SnO_2/Fe_2O_3/RGO to unravel the structural collapse mechanism and enhanced electrical conductivity for lithium-ion batteries. *Nano Energy* **2017**, *32*, 397−407.
(158) Kim, S. J.; Noh, S.-Y.; Kargar, A.; Wang, D.; Graham, G. W.; Pan, X. In situ TEM observation of the structural transformation of rutile TiO_2 nanowire during electrochemical lithiation. *Chem. Commun.* **2014**, *50*, 9932−9935.
(159) Zhong, L.; Liu, Y.; Han, W. Q.; Huang, J. Y.; Mao, S. X. In Situ Observation of Single-Phase Lithium Intercalation in Sub-25-nm Nanoparticles. *Adv. Mater.* **2017**, *29*, 1700236.
(160) Zhang, M.; Yin, K.; Hood, Z. D.; Bi, Z.; Bridges, C. A.; Dai, S.; Meng, Y. S.; Paranthaman, M. P.; Chi, M. In situ TEM observation of the electrochemical lithiation of N-doped anatase TiO_2 nanotubes as anodes for lithium-ion batteries. *J. Mater. Chem. A* **2017**, *5*, 20651−20657.
(161) Yuan, Y. F.; Nie, A. M.; Odegard, G. M.; Xu, R.; Zhou, D. H.; Santhanagopalan, S.; He, K.; Asayesh-Ardakani, H.; Meng, D. D.; Klie, R. F.; et al. Asynchronous Crystal Cell Expansion during Lithiation of K^+-Stabilized α-MnO_2. *Nano Lett.* **2015**, *15*, 2998−3007.
(162) Lee, S. Y.; Wu, L.; Poyraz, A. S.; Huang, J.; Marschilok, A. C.; Takeuchi, K. J.; Takeuchi, E. S.; Kim, M.; Zhu, Y. Lithiation Mechanism of Tunnel-Structured MnO_2 Electrode Investigated by In Situ Transmission Electron Microscopy. *Adv. Mater.* **2017**, *29*, 1703186.
(163) Cai, R.; Guo, S.; Meng, Q.; Yang, S.; Xin, H. L.; Hu, X.; Li, M.; Sun, Y.; Gao, P.; Zhang, S.; et al. Atomic-level tunnel engineering of todorokite MnO_2 for precise evaluation of lithium storage mechanisms by in situ transmission electron microscopy. *Nano Energy* **2019**, *63*, 103840.
(164) He, K.; Xin, H. L. L.; Zhao, K. J.; Yu, X. Q.; Nordlund, D.; Weng, T. C.; Li, J.; Jiang, Y.; Cadigan, C. A.; Richards, R. M.; et al. Transitions from Near-Surface to Interior Redox upon Lithiation in Conversion Electrode Materials. *Nano Lett.* **2015**, *15*, 1437−1444.
(165) He, K.; Zhang, S.; Li, J.; Yu, X.; Meng, Q.; Zhu, Y.; Hu, E.; Sun, K.; Yun, H.; Yang, X.-Q.; et al. Visualizing non-equilibrium lithiation of spinel oxide via in situ transmission electron microscopy. *Nat. Commun.* **2016**, *7*, 11441.
(166) Su, Q.; Zhang, J.; Wu, Y.; Du, G. Revealing the electrochemical conversion mechanism of porous Co_3O_4 nanoplates in lithium ion battery by in situ transmission electron microscopy. *Nano Energy* **2014**, *9*, 264−272.

https://doi.org/10.1021/acs.chemrev.4c00507
Chem. Rev. XXXX, XXX, XXX−XXX

(167) Kushima, A.; Liu, X. H.; Zhu, G.; Wang, Z. L.; Huang, J. Y.; Li, J. Leapfrog cracking and nanoamorphization of ZnO nanowires during in situ electrochemical lithiation. *Nano Lett.* **2011**, *11*, 4535−4541.
(168) Li, J.; He, K.; Meng, Q.; Li, X.; Zhu, Y.; Hwang, S.; Sun, K.; Gan, H.; Zhu, Y.; Mo, Y.; et al. Kinetic Phase Evolution of Spinel Cobalt Oxide during Lithiation. *ACS Nano* **2016**, *10*, 9577−9585.
(169) Li, Q. Q.; Wu, J. S.; Yao, Z. P.; Xu, Y. B.; Thackeray, M. M.; Wolverton, C.; Dravid, V. P. Dynamic imaging of metastable reaction pathways in lithiated cobalt oxide electrodes. *Nano Energy* **2018**, *44*, 15−22.
(170) Ding, Y. Y.; Han, T. L.; Zhang, H. G.; Cheng, M. Y.; Wu, Y.; Chen, X.; Chi, M. F.; Niu, J. J.; Liu, J. Y. A hollow Co_2SiO_4 nanosheet Li-ion battery anode with high electrochemical performance and its dynamic lithiation/delithiation using in situ transmission electron microscopy technology. *Appl. Surf. Sci.* **2019**, *490*, 510−515.
(171) Tan, G.; Wu, F.; Yuan, Y.; Chen, R.; Zhao, T.; Yao, Y.; Qian, J.; Liu, J.; Ye, Y.; Shahbazian-Yassar, R.; et al. Freestanding three-dimensional core−shell nanoarrays for lithium-ion battery anodes. *Nat. Commun.* **2016**, *7*, 11774.
(172) Cheng, X.; Li, Y.; Shi, H.; Lu, J.; Zhang, Y. Rate-dependent electrochemical reaction mechanism of spinel metal oxide anode studied by in situ TEM. *J. Alloys Compd.* **2018**, *763*, 349−354.
(173) Su, Q.; Yao, L.; Zhang, J.; Du, G.; Xu, B. In Situ Transmission Electron Microscopy Observation of the Lithiation−Delithiation Conversion Behavior of CuO/Graphene Anode. *ACS Appl. Mater. Interfaces* **2015**, *7*, 23062−23068.
(174) Su, Q.; Wang, S.; Yao, L.; Li, H.; Du, G.; Ye, H.; Fang, Y. Study on the Electrochemical Reaction Mechanism of $ZnFe_2O_4$ by In Situ Transmission Electron Microscopy. *Sci. Rep.* **2016**, *6*, 28197.
(175) Shi, S. S.; Li, Z. P.; Sun, Y.; Wang, B.; Liu, Q. N.; Hou, Y. L.; Huang, S. F.; Huang, J. Y.; Zhao, Y. F. A covalent heterostructure of monodisperse Ni_2P immobilized on N, P-co-doped carbon nanosheets for high performance sodium/lithium storage. *Nano Energy* **2018**, *48*, 510−517.
(176) Xia, W.; Zhang, Q.; Xu, F.; Sun, L. New Insights into Electrochemical Lithiation/Delithiation Mechanism of α-MoO_3 Nanobelt by in Situ Transmission Electron Microscopy. *ACS Appl. Mater. Interfaces* **2016**, *8*, 9170−9177.
(177) Liu, G.; He, Y.; Liu, Z.; Wan, H.; Xu, Y.; Deng, H.; Yang, H.; Zhang, J. G.; Sushko, P. V.; Gao, F.; et al. In Situ Visualization of the Pinning Effect of Planar Defects on Li Ion Insertion. *Nano Lett.* **2023**, *23*, 6839−6844.
(178) Gregorczyk, K. E.; Liu, Y.; Sullivan, J. P.; Rubloff, G. W. In Situ Transmission Electron Microscopy Study of Electrochemical Lithiation and Delithiation Cycling of the Conversion Anode RuO_2. *ACS Nano* **2013**, *7*, 6354−6360.
(179) Li, Y.; Sun, H.; Cheng, X.; Zhang, Y.; Zhao, K. In-situ TEM experiments and first-principles studies on the electrochemical and mechanical behaviors of α-MoO3 in Li-ion batteries. *Nano Energy* **2016**, *27*, 95−102.
(180) Qi, K.; Wei, J.; Sun, M.; Huang, Q.; Li, X.; Xu, Z.; Wang, W.; Bai, X. Real-time Observation of Deep Lithiation of Tungsten Oxide Nanowires by In Situ Electron Microscopy. *Angew. Chem., Int. Ed.* **2015**, *54*, 15222−15225.
(181) He, Y.; Gu, M.; Xiao, H.; Luo, L.; Shao, Y.; Gao, F.; Du, Y.; Mao, S. X.; Wang, C. Atomistic Conversion Reaction Mechanism of WO_3 in Secondary Ion Batteries of Li, Na, and Ca. *Angew. Chem., Int. Ed.* **2016**, *55*, 6244−6247.
(182) Giri, A.; Park, G.; Jeong, U. Layer-Structured Anisotropic Metal Chalcogenides: Recent Advances in Synthesis, Modulation, and Applications. *Chem. Rev.* **2023**, *123*, 3329−3442.
(183) Palchoudhury, S.; Ramasamy, K.; Han, J.; Chen, P.; Gupta, A. Transition metal chalcogenides for next-generation energy storage. *Nanoscale Adv.* **2023**, *5*, 2724−2742.
(184) Su, Q.; Xie, J.; Zhang, J.; Zhong, Y.; Du, G.; Xu, B. In Situ Transmission Electron Microscopy Observation of Electrochemical Behavior of CoS_2 in Lithium-Ion Battery. *ACS Appl. Mater. Interfaces* **2014**, *6*, 3016−3022.
(185) Li, Z.; Sami, I.; Yang, J.; Li, J.; Kumar, R. V.; Chhowalla, M. Lithiated metallic molybdenum disulfide nanosheets for high-performance lithium−sulfur batteries. *Nat. Energy* **2023**, *8*, 84−93.
(186) Yin, K.; Zhang, M.; Hood, Z. D.; Pan, J.; Meng, Y. S.; Chi, M. Self-Assembled Framework Formed During Lithiation of SnS_2 Nanoplates Revealed by in Situ Electron Microscopy. *Acc. Chem. Res.* **2017**, *50*, 1513−1520.
(187) Liu, X.; Wang, Y.; Yang, Y.; Lv, W.; Lian, G.; Golberg, D.; Wang, X.; Zhao, X.; Ding, Y. A MoS_2/Carbon hybrid anode for high-performance Li-ion batteries at low temperature. *Nano Energy* **2020**, *70*, 104550.
(188) Zou, R. J.; Xu, M. D.; He, S. A.; Han, X. Y.; Lin, R. J.; Cui, Z.; He, G. J.; Brett, D. J. L.; Guo, Z. X.; Hu, J. Q.; et al. Cobalt nickel nitride coated by a thin carbon layer anchoring on nitrogen-doped carbon nanotube anodes for high-performance lithium-ion batteries. *J. Mater. Chem. A* **2018**, *6*, 19853−19862.
(189) Su, Q.; Du, G.; Zhang, J.; Zhong, Y.; Xu, B.; Yang, Y.; Neupane, S.; Kadel, K.; Li, W. In Situ Transmission Electron Microscopy Investigation of the Electrochemical Lithiation−Delithiation of Individual Co_9S_8/Co-Filled Carbon Nanotubes. *ACS Nano* **2013**, *7*, 11379−11387.
(190) Zeng, Z.; Zhang, X.; Bustillo, K.; Niu, K.; Gammer, C.; Xu, J.; Zheng, H. In Situ Study of Lithiation and Delithiation of MoS_2 Nanosheets Using Electrochemical Liquid Cell Transmission Electron Microscopy. *Nano Lett.* **2015**, *15*, 5214−5220.
(191) Wang, Z.; Santhanagopalan, D.; Zhang, W.; Wang, F.; Xin, H. L.; He, K.; Li, J.; Dudney, N.; Meng, Y. S. In Situ STEM-EELS Observation of Nanoscale Interfacial Phenomena in All-Solid-State Batteries. *Nano Lett.* **2016**, *16*, 3760−3767.
(192) Gong, Y.; Zhang, J. N.; Jiang, L. W.; Shi, J. A.; Zhang, Q. H.; Yang, Z. Z.; Zou, D. L.; Wang, J. Y.; Yu, X. Q.; Xiao, R. J.; et al. In Situ Atomic-Scale Observation of Electrochemical Delithiation Induced Structure Evolution of $LiCoO_2$ Cathode in a Working All-Solid-State Battery. *J. Am. Chem. Soc.* **2017**, *139*, 4274−4277.
(193) Wang, L.; Xie, R.; Chen, B.; Yu, X.; Ma, J.; Li, C.; Hu, Z.; Sun, X.; Xu, C.; Dong, S.; et al. In-situ visualization of the space-charge-layer effect on interfacial lithium-ion transport in all-solid-state batteries. *Nat. Commun.* **2020**, *11*, 5889.
(194) Yang, L.; Li, X.; Pei, K.; You, W.; Liu, X.; Xia, H.; Wang, Y.; Che, R. Direct View on the Origin of High Li^+ Transfer Impedance in All-Solid-State Battery. *Adv. Funct. Mater.* **2021**, *31*, 2103971.
(195) Nomura, Y.; Yamamoto, K.; Hirayama, T.; Ohkawa, M.; Igaki, E.; Hojo, N.; Saitoh, K. Quantitative Operando Visualization of Electrochemical Reactions and Li Ions in All-Solid-State Batteries by STEM-EELS with Hyperspectral Image Analyses. *Nano Lett.* **2018**, *18*, 5892−5898.
(196) Nomura, Y.; Yamamoto, K.; Fujii, M.; Hirayama, T.; Igaki, E.; Saitoh, K. Dynamic imaging of lithium in solid-state batteries by operando electron energy-loss spectroscopy with sparse coding. *Nat. Commun.* **2020**, *11*, 2824.
(197) Nomura, Y.; Yamamoto, K.; Hirayama, T.; Igaki, E.; Saitoh, K. Visualization of Lithium Transfer Resistance in Secondary Particle Cathodes of Bulk-Type Solid-State Batteries. *ACS Energy Lett.* **2020**, *5*, 2098−2105.
(198) Li, S.; Sun, Y. P.; Li, N.; Tong, W.; Sun, X. L.; Black, C. T.; Hwang, S. Porosity Development at Li-Rich Layered Cathodes in All-Solid-State Battery during In Situ Delithiation. *Nano Lett.* **2022**, *22*, 4905−4911.
(199) Yu, R. H.; Zeng, W. H.; Zhou, L.; Van Tendeloo, G.; Mai, L. Q.; Yao, Z. P.; Wu, J. S. Layer-by-layer delithiation during lattice collapse as the origin of planar gliding and microcracking in Ni-rich cathodes. *Cell Rep. Phys. Sci.* **2023**, *4*, 101480.
(200) Liu, B. W.; Hu, N. F.; Li, C.; Ma, J.; Zhang, J. W.; Yang, Y.; Sun, D. Y.; Yin, B. X.; Cui, G. L. Direct Observation of Li-Ion Transport Heterogeneity Induced by Nanoscale Phase Separation in Li-rich Cathodes of Solid-State Batteries. *Angew. Chem., Int. Ed.* **2022**, *61*, e202209626.
(201) Zhou, T.; Wang, H.; Wang, Y.; Jiao, P. X.; Hao, Z. M.; Zhang, K.; Xu, J.; Liu, J. B.; He, Y. S.; Zhang, Y. X.; et al. Stabilizing lattice

https://doi.org/10.1021/acs.chemrev.4c00507
Chem. Rev. XXXX, XXX, XXX−XXX

oxygen in slightly Li-enriched nickel oxide cathodes toward high-energy batteries. *Chem-Us* **2022**, *8*, 2817−2830.
(202) Li, Q.; Yao, Z.; Lee, E.; Xu, Y.; Thackeray, M. M.; Wolverton, C.; Dravid, V. P.; Wu, J. Dynamic imaging of crystalline defects in lithium-manganese oxide electrodes during electrochemical activation to high voltage. *Nat. Commun.* **2019**, *10*, 1692.
(203) Bhatia, A.; Cretu, S.; Hallot, M.; Folastre, N.; Berthe, M.; Troadec, D.; Roussel, P.; Pereira-Ramos, J. P.; Baddour-Hadjean, R.; Lethien, C.; et al. In Situ Liquid Electrochemical TEM Investigation of $LiMn_{1.5}Ni_{0.5}O_4$ Thin Film Cathode for Micro-Battery Applications. *Small Methods* **2022**, *6*, 2100891.
(204) Zhu, J.; Shen, H.; Shi, X.; Yang, F.; Hu, X.; Zhou, W.; Yang, H.; Gu, M. Revealing the Chemical and Structural Evolution of V_2O_5 Nanoribbons in Lithium-Ion Batteries Using in Situ Transmission Electron Microscopy. *Anal. Chem.* **2019**, *91*, 11055−11062.
(205) Mukherjee, A.; Ardakani, H. A.; Yi, T.; Cabana, J.; Shahbazian-Yassar, R.; Klie, R. F. Direct characterization of the Li intercalation mechanism into α-V_2O_5 nanowires using in-situ transmission electron microscopy. *Appl. Phys. Lett.* **2017**, *110*, 213903.
(206) Zhu, Y.; Wang, J. W.; Liu, Y.; Liu, X.; Kushima, A.; Liu, Y.; Xu, Y.; Mao, S. X.; Li, J.; Wang, C.; et al. In Situ Atomic-Scale Imaging of Phase Boundary Migration in $FePO_4$ Microparticles During Electrochemical Lithiation. *Adv. Mater.* **2013**, *25*, 5461−5466.
(207) Niu, J.; Kushima, A.; Qian, X.; Qi, L.; Xiang, K.; Chiang, Y. M.; Li, J. In Situ Observation of Random Solid Solution Zone in $LiFePO_4$ Electrode. *Nano Lett.* **2014**, *14*, 4005−4010.
(208) Holtz, M. E.; Yu, Y.; Gunceler, D.; Gao, J.; Sundararaman, R.; Schwarz, K. A.; Arias, T. A.; Abruna, H. D.; Muller, D. A. Nanoscale Imaging of Lithium Ion Distribution During In Situ Operation of Battery Electrode and Electrolyte. *Nano Lett.* **2014**, *14*, 1453−1459.
(209) Karakulina, O. M.; Demortiere, A.; Dachraoui, W.; Abakumov, A. M.; Hadermann, J. In Situ Electron Diffraction Tomography Using a Liquid-Electrochemical Transmission Electron Microscopy Cell for Crystal Structure Determination of Cathode Materials for Li-Ion batteries. *Nano Lett.* **2018**, *18*, 6286−6291.
(210) Poulizac, J.; Boulineau, A.; Billy, E.; Masenelli-Varlot, K. Operando Liquid-Phase TEM Experiments for the Investigation of Dissolution Kinetics: Application to Li-Ion Battery Materials. *Microsc. Microanal.* **2023**, *29*, 105−117.
(211) Yu, S.-H.; Lee, S. H.; Lee, D. J.; Sung, Y.-E.; Hyeon, T. Conversion Reaction-Based Oxide Nanomaterials for Lithium Ion Battery Anodes. *Small* **2016**, *12*, 2146−2172.
(212) Cao, K.; Jin, T.; Yang, L.; Jiao, L. Recent progress in conversion reaction metal oxide anodes for Li-ion batteries. *Mater. Chem. Front.* **2017**, *1*, 2213−2242.
(213) Wu, F.; Yushin, G. Conversion cathodes for rechargeable lithium and lithium-ion batteries. *Energy Environ. Sci.* **2017**, *10*, 435−459.
(214) Karki, K.; Wu, L. J.; Ma, Y.; Armstrong, M. J.; Holmes, J. D.; Garofalini, S. H.; Zhu, Y. M.; Stach, E. A.; Wang, F. Revisiting Conversion Reaction Mechanisms in Lithium Batteries: Lithiation-Driven Topotactic Transformation in FeF_2. *J. Am. Chem. Soc.* **2018**, *140*, 17915−17922.
(215) Fan, X. L.; Hu, E. Y.; Ji, X.; Zhu, Y. Z.; Han, F. D.; Hwang, S. Y.; Liu, J.; Bak, S. M.; Ma, Z. H.; Gao, T.; et al. High energy-density and reversibility of iron fluoride cathode enabled via an intercalation-extrusion reaction. *Nat. Commun.* **2018**, *9*, 2324.
(216) Pereira, N.; Badway, F.; Wartelsky, M.; Gunn, S.; Amatucci, G. G. Iron Oxyfluorides as High Capacity Cathode Materials for Lithium Batteries. *J. Electrochem. Soc.* **2009**, *156*, A407−A416.
(217) Fan, X.; Luo, C.; Lamb, J.; Zhu, Y.; Xu, K.; Wang, C. PEDOT Encapsulated FeOF Nanorod Cathodes for High Energy Lithium-Ion Batteries. *Nano Lett.* **2015**, *15*, 7650−7656.
(218) Villa, C.; Kim, S. K.; Lu, Y. X.; Dravid, V. P.; Wu, J. S. Cu-Substituted NiF_2 as a Cathode Material for Li-Ion Batteries. *ACS Appl. Mater. Interfaces* **2019**, *11*, 647−654.
(219) Liu, H.; Li, Q.; Yao, Z.; Li, L.; Li, Y.; Wolverton, C.; Hersam, M. C.; Wu, J.; Dravid, V. P. Origin of Fracture-Resistance to Large Volume Change in Cu-Substituted Co_3O_4 Electrodes. *Adv. Mater.* **2018**, *30*, 1704851.
(220) He, J.; Chen, Y.; Lv, W.; Wen, K.; Xu, C.; Zhang, W.; Qin, W.; He, W. Three-Dimensional CNT/Graphene−Li_2S Aerogel as Free-standing Cathode for High-Performance Li−S Batteries. *ACS Energy Lett.* **2016**, *1*, 820−826.
(221) Ansari, Y.; Zhang, S.; Wen, B.; Fan, F.; Chiang, Y.-M. Stabilizing Li−S Battery Through Multilayer Encapsulation of Sulfur. *Adv. Energy Mater.* **2019**, *9*, 1802213.
(222) Lin, Y.; Huang, S.; Zhong, L.; Wang, S.; Han, D.; Ren, S.; Xiao, M.; Meng, Y. Organic liquid electrolytes in Li-S batteries: actualities and perspectives. *Energy Storage Mater.* **2021**, *34*, 128−147.
(223) Kim, H.; Lee, J. T.; Magasinski, A.; Zhao, K. J.; Liu, Y.; Yushin, G. In Situ TEM Observation of Electrochemical Lithiation of Sulfur Confined within Inner Cylindrical Pores of Carbon Nanotubes. *Adv. Energy Mater.* **2015**, *5*, 1501306.
(224) Yang, Z. Z.; Zhu, Z. Y.; Ma, J.; Xiao, D. D.; Kui, X.; Yao, Y.; Yu, R. C.; Wei, X.; Gu, L.; Hu, Y. S.; et al. Phase Separation of Li_2S/S at Nanoscale during Electrochemical Lithiation of the Solid-State Lithium-Sulfur Battery Using In Situ TEM. *Adv. Energy Mater.* **2016**, *6*, 1600806.
(225) Wang, Z.; Tang, Y.; Zhang, L.; Li, M.; Shan, Z.; Huang, J. In Situ TEM Observations of Discharging/Charging of Solid-State Lithium-Sulfur Batteries at High Temperatures. *Small* **2020**, *16*, 2001899.
(226) Wang, Z.; Tang, Y.; Fu, X.; Wang, J.; Peng, Z.; Zhang, L.; Huang, J. In Situ Imaging Polysulfides Electrochemistry of Li-S Batteries in a Hollow Carbon Nanotubule Wet Electrochemical Cell. *ACS Appl. Mater. Interfaces* **2020**, *12*, 55971−55981.
(227) Tang, W.; Chen, Z.; Tian, B.; Lee, H.-W.; Zhao, X.; Fan, X.; Fan, Y.; Leng, K.; Peng, C.; Kim, M.-H.; et al. In Situ Observation and Electrochemical Study of Encapsulated Sulfur Nanoparticles by MoS_2 Flakes. *J. Am. Chem. Soc.* **2017**, *139*, 10133−10141.
(228) Tan, G.; Xu, R.; Xing, Z.; Yuan, Y.; Lu, J.; Wen, J.; Liu, C.; Ma, L.; Zhan, C.; Liu, Q.; et al. Burning lithium in CS_2 for high-performing compact Li_2S−graphene nanocapsules for Li−S batteries. *Nat. Energy* **2017**, *2*, 17090.
(229) Li, Q. Q.; Liu, H. G.; Yao, Z. P.; Cheng, J. P.; Li, T. H.; Li, Y.; Wolverton, C.; Wu, J. S.; Dravid, V. P. Electrochemistry of Selenium with Sodium and Lithium: Kinetics and Reaction Mechanism. *ACS Nano* **2016**, *10*, 8788−8795.
(230) Guo, B.; Chen, J.; Wang, Z.; Su, Y.; Li, H.; Ye, H.; Zhang, L.; Tang, Y.; Huang, J. In situ TEM studies of electrochemistry of high temperature lithium-selenium all-solid-state batteries. *Electrochim. Acta* **2022**, *404*, 139773.
(231) Yang, T.; Li, H.; Chen, J.; Ye, H.; Yao, J.; Su, Y.; Guo, B.; Peng, Z.; Shen, T.; Tang, Y.; et al. In situ imaging electrocatalytic CO_2 reduction and evolution reactions in all-solid-state Li−CO_2 nano-batteries. *Nanoscale* **2020**, *12*, 23967−23974.
(232) Zhong, L.; Mitchell, R. R.; Liu, Y.; Gallant, B. M.; Thompson, C. V.; Huang, J. Y.; Mao, S. X.; Shao-Horn, Y. In Situ Transmission Electron Microscopy Observations of Electrochemical Oxidation of Li_2O_2. *Nano Lett.* **2013**, *13*, 2209−2214.
(233) Tang, Y.; Yang, T.; Chen, J.; Li, H.; Ye, H.; Du, C.; Tang, Y.; Xia, M.; Shen, T.; Zhang, L.; et al. In situ imaging of lithium superoxide dynamics in an all-solid-state Li−O_2 nanobattery. *J. Mater. Chem. A* **2022**, *10*, 20294−20301.
(234) Kushima, A.; Koido, T.; Fujiwara, Y.; Kuriyama, N.; Kusumi, N.; Li, J. Charging/Discharging Nanomorphology Asymmetry and Rate-Dependent Capacity Degradation in Li−Oxygen Battery. *Nano Lett.* **2015**, *15*, 8260−8265.
(235) Liu, P.; Han, J.; Guo, X.; Ito, Y.; Yang, C.; Ning, S.; Fujita, T.; Hirata, A.; Chen, M. Operando characterization of cathodic reactions in a liquid-state lithium-oxygen micro-battery by scanning transmission electron microscopy. *Sci. Rep.* **2018**, *8*, 3134.
(236) He, K.; Bi, X.; Yuan, Y.; Foroozan, T.; Song, B.; Amine, K.; Lu, J.; Shahbazian-Yassar, R. Operando liquid cell electron microscopy of discharge and charge kinetics in lithium-oxygen batteries. *Nano Energy* **2018**, *49*, 338−345.

https://doi.org/10.1021/acs.chemrev.4c00507
Chem. Rev. XXXX, XXX, XXX−XXX

(237) Yang, C.; Han, J.; Liu, P.; Hou, C.; Huang, G.; Fujita, T.; Hirata, A.; Chen, M. Direct Observations of the Formation and Redox-Mediator-Assisted Decomposition of Li_2O_2 in a Liquid-Cell Li−O_2 Microbattery by Scanning Transmission Electron Microscopy. *Adv. Mater.* **2017**, *29*, 1702752.
(238) Hou, C.; Han, J.; Liu, P.; Yang, C.; Huang, G.; Fujita, T.; Hirata, A.; Chen, M. Operando observations of RuO_2 catalyzed Li_2O_2 formation and decomposition in a Li-O_2 micro-battery. *Nano Energy* **2018**, *47*, 427−433.
(239) Lee, D.; Park, H.; Ko, Y.; Park, H.; Hyeon, T.; Kang, K.; Park, J. Direct Observation of Redox Mediator-Assisted Solution-Phase Discharging of Li−O_2 Battery by Liquid-Phase Transmission Electron Microscopy. *J. Am. Chem. Soc.* **2019**, *141*, 8047−8052.
(240) Hou, C.; Han, J.; Liu, P.; Huang, G.; Chen, M. Synergetic Effect of Liquid and Solid Catalysts on the Energy Efficiency of Li−O_2 Batteries: Cell Performances and Operando STEM Observations. *Nano Lett.* **2020**, *20*, 2183−2190.
(241) Abellan, P.; Mehdi, B. L.; Parent, L. R.; Gu, M.; Park, C.; Xu, W.; Zhang, Y.; Arslan, I.; Zhang, J. G.; Wang, C. M.; et al. Probing the Degradation Mechanisms in Electrolyte Solutions for Li-Ion Batteries by in Situ Transmission Electron Microscopy. *Nano Lett.* **2014**, *14*, 1293−1299.
(242) Gao, H.; Ai, X.; Wang, H.; Li, W.; Wei, P.; Cheng, Y.; Gui, S.; Yang, H.; Yang, Y.; Wang, M. S. Visualizing the failure of solid electrolyte under GPa-level interface stress induced by lithium eruption. *Nat. Commun.* **2022**, *13*, 5050.
(243) Sun, H.; Liu, Q.; Chen, J.; Li, Y.; Ye, H.; Zhao, J.; Geng, L.; Dai, Q.; Yang, T.; Li, H.; et al. In Situ Visualization of Lithium Penetration through Solid Electrolyte and Dead Lithium Dynamics in Solid-State Lithium Metal Batteries. *ACS Nano* **2021**, *15*, 19070−19079.
(244) Wang, M. J.; Carmona, E.; Gupta, A.; Albertus, P.; Sakamoto, J. Enabling "lithium-free" manufacturing of pure lithium metal solid-state batteries through in situ plating. *Nat. Commun.* **2020**, *11*, 5201.
(245) Cheng, D.; Wynn, T. A.; Wang, X.; Wang, S.; Zhang, M.; Shimizu, R.; Bai, S.; Nguyen, H.; Fang, C.; Kim, M.-C.; et al. Unveiling the Stable Nature of the Solid Electrolyte Interphase between Lithium Metal and LiPON via Cryogenic Electron Microscopy. *Joule* **2020**, *4*, 2484−2500.
(246) Hood, Z. D.; Chen, X.; Sacci, R. L.; Liu, X.; Veith, G. M.; Mo, Y.; Niu, J.; Dudney, N. J.; Chi, M. Elucidating Interfacial Stability between Lithium Metal Anode and Li Phosphorus Oxynitride via In Situ Electron Microscopy. *Nano Lett.* **2021**, *21*, 151−157.
(247) Geng, L.; Liu, Q.; Chen, J.; Jia, P.; Ye, H.; Yan, J.; Zhang, L.; Tang, Y.; Huang, J. In situ observation of electrochemical Ostwald ripening during sodium deposition. *Nano Res.* **2022**, *15*, 2650−2654.
(248) Geng, L.; Zhao, C.; Yan, J.; Fu, C.; Zhang, X.; Yao, J.; Sun, H.; Su, Y.; Liu, Q.; Zhang, L.; et al. In situ imaging the dynamics of sodium metal deposition and stripping. *J. Mater. Chem. A* **2022**, *10*, 14875−14883.
(249) Zeng, Z.; Barai, P.; Lee, S.-Y.; Yang, J.; Zhang, X.; Zheng, W.; Liu, Y.-S.; Bustillo, K. C.; Ercius, P.; Guo, J.; et al. Electrode roughness dependent electrodeposition of sodium at the nanoscale. *Nano Energy* **2020**, *72*, 104721.
(250) Gong, C.; Pu, S. D.; Zhang, S.; Yuan, Y.; Ning, Z.; Yang, S.; Gao, X.; Chau, C.; Li, Z.; Liu, J.; et al. The role of an elastic interphase in suppressing gas evolution and promoting uniform electroplating in sodium metal anodes. *Energy Environ. Sci.* **2023**, *16*, 535−545.
(251) Kim, S.; Cui, J.; Dravid, V. P.; He, K. Orientation-Dependent Intercalation Channels for Lithium and Sodium in Black Phosphorus. *Adv. Mater.* **2019**, *31*, 1904623.
(252) Li, Z.; Tan, X. H.; Li, P.; Kalisvaart, P.; Janish, M. T.; Mook, W. M.; Luber, E. J.; Jungjohann, K. L.; Carter, C. B.; Mitlin, D. Coupling In Situ TEM and Ex Situ Analysis to Understand Heterogeneous Sodiation of Antimony. *Nano Lett.* **2015**, *15*, 6339−6348.
(253) Wang, J. W.; Liu, X. H.; Mao, S. X.; Huang, J. Y. Microstructural Evolution of Tin Nanoparticles during In Situ Sodium Insertion and Extraction. *Nano Lett.* **2012**, *12*, 5897−5902.
(254) Lu, X.; Adkins, E. R.; He, Y.; Zhong, L.; Luo, L.; Mao, S. X.; Wang, C.-M.; Korgel, B. A. Germanium as a Sodium Ion Battery Material: In Situ TEM Reveals Fast Sodiation Kinetics with High Capacity. *Chem. Mater.* **2016**, *28*, 1236−1242.
(255) Huang, Y.; Zhu, C.; Zhang, S.; Hu, X.; Zhang, K.; Zhou, W.; Guo, S.; Xu, F.; Zeng, H. Ultrathin Bismuth Nanosheets for Stable Na-Ion Batteries: Clarification of Structure and Phase Transition by in Situ Observation. *Nano Lett.* **2019**, *19*, 1118−1123.
(256) Cui, J.; Zheng, H. K.; Zhang, Z. L.; Hwang, S.; Yang, X. Q.; He, K. Origin of anomalous high-rate Na-ion electrochemistry in layered bismuth telluride anodes. *Matter* **2021**, *4*, 1335−1351.
(257) He, K.; Zhou, Y. N.; Gao, P.; Wang, L. P.; Pereira, N.; Amatucci, G. G.; Nam, K. W.; Yang, X. Q.; Zhu, Y. M.; Wang, F.; et al. Sodiation via Heterogeneous Disproportionation in FeF_2 Electrodes for Sodium-Ion Batteries. *ACS Nano* **2014**, *8*, 7251−7259.
(258) Wang, X. Z.; Yao, Z. P.; Hwang, S.; Pan, Y.; Dong, H.; Fu, M. S.; Li, N.; Sun, K.; Gan, H.; Yao, Y.; et al. In Situ Electron Microscopy Investigation of Sodiation of Titanium Disulfide Nanoflakes. *ACS Nano* **2019**, *13*, 9421−9430.
(259) Boebinger, M. G.; Yeh, D.; Xu, M.; Miles, C.; Wang, B. L.; Papakyriakou, M.; Lewis, J. A.; Kondekar, N. P.; Cortes, F. J. Q.; Hwang, S.; et al. Avoiding Fracture in a Conversion Battery Material through Reaction with Larger Ions. *Joule* **2018**, *2*, 1783−1799.
(260) Yao, S. S.; Cui, J.; Lu, Z. H.; Xu, Z. L.; Qin, L.; Huang, J. Q.; Sadighi, Z.; Ciucci, F.; Kim, J. K. Unveiling the Unique Phase Transformation Behavior and Sodiation Kinetics of 1D van der Waals Sb_2S_3 Anodes for Sodium Ion Batteries. *Adv. Energy Mater.* **2017**, *7*, 1602149.
(261) Yao, L.; Xia, W.; Zhang, H.; Dong, H.; Xin, H. L.; Gao, P.; Cai, R.; Zhu, C.; Wu, Y.; Nie, M.; et al. In situ visualization of sodium transport and conversion reactions of FeS_2 nanotubes made by morphology engineering. *Nano Energy* **2019**, *60*, 424−431.
(262) Wu, Y.; Luo, W.; Gao, P.; Zhu, C.; Hu, X.; Qu, K.; Chen, J.; Wang, Y.; Sun, L.; Mai, L.; et al. Unveiling the microscopic origin of asymmetric phase transformations in (de)sodiated Sb_2Se_3 with in situ transmission electron microscopy. *Nano Energy* **2020**, *77*, 105299.
(263) Fu, R.; Pan, J.; Wang, M.; Min, H.; Dong, H.; Cai, R.; Sun, Z.; Xiong, Y.; Cui, F.; Lei, S. Y.; et al. In Situ Atomic-Scale Deciphering of Multiple Dynamic Phase Transformations and Reversible Sodium Storage in Ternary Metal Sulfide Anode. *ACS Nano* **2023**, *17*, 12483−12498.
(264) Xia, W.; Xu, F.; Zhu, C.; Xin, H. L.; Xu, Q.; Sun, P.; Sun, L. Probing microstructure and phase evolution of α-MoO_3 nanobelts for sodium-ion batteries by in situ transmission electron microscopy. *Nano Energy* **2016**, *27*, 447−456.
(265) Park, J. Y.; Kim, S. J.; Chang, J. H.; Seo, H. K.; Lee, J. Y.; Yuk, J. M. Atomic visualization of a non-equilibrium sodiation pathway in copper sulfide. *Nat. Commun.* **2018**, *9*, 922.
(266) Li, Y.; Tang, Y.; Li, X.; Tu, W.; Zhang, L.; Huang, J. In Situ TEM Studies of Sodium Polysulfides Electrochemistry in High Temperature Na−S Nanobatteries. *Small* **2021**, *17*, 2100846.
(267) Zhang, Z.; Wang, Z.; Zhang, L.; Liu, D.; Yu, C.; Yan, X.; Xie, J.; Huang, J. Unraveling the Conversion Evolution on Solid-State Na−SeS_2 Battery via In Situ TEM. *Adv. Sci.* **2022**, *9*, 2200744.
(268) Han, S.; Cai, C.; Yang, F.; Zhu, Y.; Sun, Q.; Zhu, Y. G.; Li, H.; Wang, H.; Shao-Horn, Y.; Sun, X.; et al. Interrogation of the Reaction Mechanism in a Na−O_2 Battery Using In Situ Transmission Electron Microscopy. *ACS Nano* **2020**, *14*, 3669−3677.
(269) Sun, H.; Liu, Q.; Gao, Z.; Geng, L.; Li, Y.; Zhang, F.; Yan, J.; Gao, Y.; Suenaga, K.; Zhang, L.; et al. In situ TEM visualization of single atom catalysis in solid-state Na−O_2 nanobatteries. *J. Mater. Chem. A* **2022**, *10*, 6096−6106.
(270) Lutz, L.; Dachraoui, W.; Demortiere, A.; Johnson, L. R.; Bruce, P. G.; Grimaud, A.; Tarascon, J. M. Operando Monitoring of the Solution-Mediated Discharge and Charge Processes in a Na−O_2 Battery Using Liquid-Electrochemical Transmission Electron Microscopy. *Nano Lett.* **2018**, *18*, 1280−1289.
(271) Liu, Q.; Tang, Y.; Sun, H.; Yang, T.; Sun, Y.; Du, C.; Jia, P.; Ye, H.; Chen, J.; Peng, Q.; et al. In Situ Electrochemical Study of Na−

https://doi.org/10.1021/acs.chemrev.4c00507
Chem. Rev. XXXX, XXX, XXX−XXX

O_2/CO_2 Batteries in an Environmental Transmission Electron Microscope. *ACS Nano* **2020**, *14*, 13232−13245.
(272) Goikolea, E.; Palomares, V.; Wang, S.; de Larramendi, I. R.; Guo, X.; Wang, G.; Rojo, T. Na-Ion Batteries—Approaching Old and New Challenges. *Adv. Energy Mater.* **2020**, *10*, 2002055.
(273) Niu, J.; Zhang, Z.; Aurbach, D. Alloy Anode Materials for Rechargeable Mg Ion Batteries. *Adv. Energy Mater.* **2020**, *10*, 2000697.
(274) Song, M.; Tan, H.; Chao, D.; Fan, H. J. Recent Advances in Zn-Ion Batteries. *Adv. Funct. Mater.* **2018**, *28*, 1802564.
(275) Hosaka, T.; Kubota, K.; Hameed, A. S.; Komaba, S. Research Development on K-Ion Batteries. *Chem. Rev.* **2020**, *120*, 6358−6466.
(276) Wu, Y. A.; Yin, Z.; Farmand, M.; Yu, Y. S.; Shapiro, D. A.; Liao, H. G.; Liang, W. I.; Chu, Y. H.; Zheng, H. In-situ Multimodal Imaging and Spectroscopy of Mg Electrodeposition at Electrode-Electrolyte Interfaces. *Sci. Rep.* **2017**, *7*, 42527.
(277) Singh, N.; Arthur, T. S.; Tutusaus, O.; Li, J.; Kisslinger, K.; Xin, H. L.; Stach, E. A.; Fan, X.; Mohtadi, R. Achieving High Cycling Rates via In Situ Generation of Active Nanocomposite Metal Anodes. *ACS Appl. Energy Mater.* **2018**, *1*, 4651−4661.
(278) Arthur, T. S.; Glans, P.-A.; Singh, N.; Tutusaus, O.; Nie, K.; Liu, Y.-S.; Mizuno, F.; Guo, J.; Alsem, D. H.; Salmon, N. J.; et al. Interfacial Insight from Operando XAS/TEM for Magnesium Metal Deposition with Borohydride Electrolytes. *Chem. Mater.* **2017**, *29*, 7183−7188.
(279) Sasaki, Y.; Yoshida, K.; Kawasaki, T.; Kuwabara, A.; Ukyo, Y.; Ikuhara, Y. In situ electron microscopy analysis of electrochemical Zn deposition onto an electrode. *J. Power Sources* **2021**, *481*, 228831.
(280) Huang, Y.; Gu, Q.; Guo, Z.; Liu, W.; Chang, Z.; Liu, Y.; Kang, F.; Dong, L.; Xu, C. Unraveling dynamical behaviors of zinc metal electrodes in aqueous electrolytes through an operando study. *Energy Storage Mater.* **2022**, *46*, 243−251.
(281) Cai, R.; Bao, L.; Zhang, W.; Xia, W.; Sun, C.; Dong, W.; Chang, X.; Hua, Z.; Shao, R.; Fukuda, T.; et al. In situ atomic-scale observation of size-dependent (de)potassiation and reversible phase transformation in tetragonal FeSe anodes. *InfoMat* **2023**, *5*, e12364.
(282) Park, J. H.; Schneider, N. M.; Steingart, D. A.; Deligianni, H.; Kodambaka, S.; Ross, F. M. Control of Growth Front Evolution by Bi Additives during ZnAu Electrodeposition. *Nano Lett.* **2018**, *18*, 1093−1098.
(283) Li, Y.; Li, Y.; Pei, A.; Yan, K.; Sun, Y.; Wu, C.-L.; Joubert, L.-M.; Chin, R.; Koh, A. L.; Yu, Y.; et al. Atomic structure of sensitive battery materials and interfaces revealed by cryo−electron microscopy. *Science* **2017**, *358*, 506−510.
(284) Wang, X.; Zhang, M.; Alvarado, J.; Wang, S.; Sina, M.; Lu, B.; Bouwer, J.; Xu, W.; Xiao, J.; Zhang, J.-G.; et al. New Insights on the Structure of Electrochemically Deposited Lithium Metal and Its Solid Electrolyte Interphases via Cryogenic TEM. *Nano Lett.* **2017**, *17*, 7606−7612.
(285) Cheng, D.; Lu, B.; Raghavendran, G.; Zhang, M.; Meng, Y. S. Leveraging cryogenic electron microscopy for advancing battery design. *Matter* **2022**, *5*, 26−42.
(286) Zachman, M. J.; Hachtel, J. A.; Idrobo, J. C.; Chi, M. Emerging Electron Microscopy Techniques for Probing Functional Interfaces in Energy Materials. *Angew. Chem., Int. Ed.* **2020**, *59*, 1384−1396.
(287) Thersleff, T.; Biendicho, J. J.; Prakasha, K. R.; Moreno, E. M.; Jøsang, L. O.; Grins, J.; Jaworski, A.; Svensson, G. Exploring the Nanoscale Origin of Performance Enhancement in $Li_{1.1}Ni_{0.35}Mn_{0.55}O_2$ Batteries Due to Chemical Doping. *Adv. Energy Mater.* **2023**, *13*, 2203889.
(288) Zhu, Y.; Wu, D.; Yang, X.; Zeng, L.; Zhang, J.; Chen, D.; Wang, B.; Gu, M. Microscopic investigation of crack and strain of $LiCoO_2$ cathode cycled under high voltage. *Energy Storage Mater.* **2023**, *60*, 102828.

https://doi.org/10.1021/acs.chemrev.4c00507
Chem. Rev. XXXX, XXX, XXX−XXX